MEASUREMENT OF THE FORM FACTOR RATIOS FOR THE CHARM SEMILEPTONIC DECAYS $D^+ \to \overline{K}^{*0}\ell^+\nu_\ell$

by

DANIEL MIHALCEA

B.S., Bucharest University, 1980

M.S., Bucharest University, 1981

AN ABSTRACT OF A DISSERTATION

submitted in partial fulfillment of the

requirements for the degree

DOCTOR OF PHILOSOPHY

Department of Physics

College of Arts and Sciences

KANSAS STATE UNIVERSITY

Manhattan, Kansas

1998

Reproduced with permission of the copyright owner. Further reproduction prohibited without permission.

MEASUREMENT OF THE FORM FACTOR RATIOS FOR THE CHARM SEMILEPTONIC DECAYS $D^+ \to \overline{K}^{*0}\ell^+\nu_\ell$

by

DANIEL MIHALCEA

B.S., Bucharest University, 1980

M.S., Bucharest University, 1981

A DISSERTATION

submitted in partial fulfillment of the

requirements for the degree

DOCTOR OF PHILOSOPHY

Department of Physics

College of Arts and Sciences

KANSAS STATE UNIVERSITY

Manhattan, Kansas

1998

Approved By:

Neville W. Reay

Major Professor

Neville W. Reay

Reproduced with permission of the copyright owner. Further reproduction prohibited without permission.

ABSTRACT

The form factor ratios $r_V = V(0)/A_1(0)$, $r_2 = A_2(0)/A_1(0)$ and $r_3 = A_3(0)/A_1(0)$ in the decay $D^+ \to \overline{K}^{*0} l^+ \nu_l$, $\overline{K}^{*0} \to K^- \pi^+$ have been measured from charm hadroproduction experiment E791 at Fermilab. From 3034 signal events in the muon channel, we obtain $r_V = 1.84 \pm 0.11 \pm 0.09$, $r_2 = 0.75 \pm 0.08 \pm 0.09$ and, as a first measurement of r_3, we find $0.04 \pm 0.33 \pm 0.29$. The values of the form factor ratios r_V and r_2 measured for muon channel are combined with the slightly revised values of our previously published measurement of r_V and r_2 for the electron channel. The combined E791 results for the muon and electron channels are $r_V = 1.87 \pm 0.08 \pm 0.07$ and $r_2 = 0.73 \pm 0.06 \pm 0.08$.

Reproduced with permission of the copyright owner. Further reproduction prohibited without permission.

Contents

List of Figures v

List of Tables x

Acknowledgments xiii

Dedication xiv

1 Theoretical Motivation **1**

1.1 Form Factors in the Standard Model 2

1.2 The Differential Decay Rate 4

1.3 The Case of Zero Lepton Mass 6

1.4 The Effects of the Lepton Mass 7

1.5 Theoretical Predictions for the Form Factor Ratios 11

2 E791 Experimental Setup **14**

2.1 Charm Production 16

2.1.1 Beamline 16

2.1.2 Target 17

2.2 Tracking and Vertexing System 18

Reproduced with permission of the copyright owner. Further reproduction prohibited without permission.

2.2.1 E791 Coordinate System 18

2.2.2 Silicon Microstrip Detectors 18

2.2.3 Proportional Wire Chambers 19

2.2.4 Drift Chambers 20

2.3 Momentum and Charge Measurement 21

2.4 Particle Identification 22

2.4.1 Čerenkov Counters 22

2.4.2 Segmented Liquid Ionization Calorimeter (SLIC) 26

2.4.3 Muon Identification 27

2.5 Trigger 30

3 Data Selection **32**

3.1 Strip, Substrip and Microstrip 33

3.2 Nanostrip 34

3.3 Analysis Cuts 36

3.4 $D^+ \to \overline{K}^{*0}\mu^+\nu_\mu$ Signal 39

3.5 Summary of the Cuts 42

4 Fitting Technique **44**

4.1 Monte Carlo Sample 45

4.2 Kinematic Variable Resolutions 48

4.3 Maximum Likelihood 49

4.4 Smearing and Acceptance Effects 51

4.4.1 Distorted Distribution Function 51

Reproduced with permission of the copyright owner. Further reproduction prohibited without permission.

4.4.2 Sources of Smearing Effects 52

4.5 Smearing and Acceptance Effects 53

4.6 Unbinned Maximum Likelihood Method 53

4.6.1 General Description 53

4.6.2 Including Background 54

4.7 Matrix Method 55

4.7.1 Motivation 55

4.7.2 General Description 56

4.7.3 Including Background 58

4.8 Particle Identification Efficiency 59

5 Systematic Checks **61**

5.1 Introduction 61

5.2 Checks of Fitting Techniques 62

5.2.1 Fit with Known Form Factors 62

5.3 Monte Carlo Volume Size 64

5.3.1 Number of Monte Carlo Points Associated with Each Data Point . . 66

5.4 Simulation of Detector Effects 67

5.4.1 Hadron Identification 68

5.4.2 Muon Identification 69

5.4.3 Production Mechanism 72

5.4.4 Spectrometer acceptance 75

5.4.5 Final Cut Selection 76

Reproduced with permission of the copyright owner. Further reproduction prohibited without permission.

5.4.6 Number of Background Events 78

5.4.7 Background Shape 80

5.5 Other Checks 83

5.5.1 Fitting Subsamples of the Data 83

5.5.2 Charge Dependence 84

5.5.3 $M_{K\pi}$ Dependence 85

5.5.4 Choice of Neutrino Momentum 85

5.5.5 Stability of the Fit 86

5.5.6 M_{min} Cut 87

5.6 Summary of the Systematic Errors 87

6 Results and Conclusions **90**

6.1 Final Results 90

6.2 Conclusions 93

6.2.1 $D^+ \to \overline{K}^{*0}\mu^+\nu_\mu$ 93

6.2.2 $D^+ \to \overline{K}^{*0}\ell^+\nu_\ell$ 95

6.3 Future Improvements 98

A Neutrino Momentum Ambiguity **101**

B Muon Identification **103**

C The Origin of Systematic Shifts in Fitting **107**

Reproduced with permission of the copyright owner. Further reproduction prohibited without permission.

List of Figures

1.1 Semileptonic decay $D^+ \to \overline{K}^{*0}\ell^+\nu_\ell$. 2

1.2 Definition of the angles θ_l , θ_V and χ in the decay $D \longrightarrow K^*l\nu$. 5

1.3 Spin-1 component of the W boson (left); Spin-0 component of the W boson. 8

1.4 Monte Carlo simulation of differential decay rates $d\Gamma/dq^2$ for muon and electron decay modes. 11

2.1 The E791 Spectrometer. 15

2.2 Layout of the Fermilab beam lines. 16

2.3 The schematic layout of the E791 target foils. 17

2.4 The E791 coordinate system. 19

2.5 Schematic of the first Čerenkov detector, C1. 23

2.6 Schematic of the second Čerenkov detector, C2. 24

2.7 Schematic of the mirror segmentation in C1 and C2 Čerenkov detectors. . . 25

2.8 Schematic view of the SLIC. 28

2.9 Geometry of the X muon wall. 28

2.10 Geometry of the Y muon wall. 29

2.11 Location of scintillating paddles used in trigger decision. 30

Reproduced with permission of the copyright owner. Further reproduction prohibited without permission.

3.1 Significance of the signal when SDZ cut changes from $SDZ > 12$ to $SDZ > 20$. The optimized cut is $SDZ > 15$. 35

3.2 Right-sign (clear histograms) and wrong-sign (shaded) distributions of the linear combination chosen by CART (top) and minimum parent mass (bottom). Events lying to the left of the vertical line (top plot) and between the two vertical lines (bottom plot) are kept, and the rest are discarded. . . 38

3.3 Distributions of minimum parent mass M_{min} and $K\pi$ invariant mass for $D^+ \to \overline{K}^{*0}\mu^+\nu_\mu$ candidate events. Right-sign (RS) and wrong-sign (WS) samples are defined in the text. Top left: M_{min} for events with $K\pi$ mass in the range 0.85 to 0.94 GeV/c^2. Top right: $K\pi$ invariant mass for events with M_{min} in the range 1.6 to 2.0 GeV/c^2. Bottom: background-subtracted (RS-WS) $K\pi$ mass distribution (crosses) compared to Monte Carlo prediction (dashed histogram) for events with M_{min} in the range 1.6 to 2.0 GeV/c^2. All candidates pass all the other final selection cuts. The arrows indicate the range of the final sample. 40

3.4 Distributions of the four kinematic variables for RS data events calculated using the negative solution of neutrino momentum (left) and the positive solution (right). The distributions of WS events are drawn with dash lines. 41

4.1 Distributions of the four kinematical variables for Monte Carlo events calculated using the negative solution of neutrino momentum (left) and the positive solution (right).The plots were done using the whole MC sample (95,579 events). 46

4.2 The distributions of $M_{K\pi}$ (top) and M_{min} (bottom) in background subtracted data (cross hatches) overlaid with Monte Carlo (dashed line). 47

4.3 Resolution of the decay rate when Monte Carlo events were reconstructed using the lower neutrino momentum solution (top) and the higher neutrino momentum solution (bottom). 50

Reproduced with permission of the copyright owner. Further reproduction prohibited without permission.

5.1 Distributions of R_2, R_V and R_3 for the 32 Monte Carlo subsamples. The form factor ratios were calculated with the unbinned loglikelihood method (left side plots) and with the matrix method (right side plots). 63

5.2 Values of form factor ratios calculated with different Monte Carlo volume sizes. The ranges of q^2/q^2_{max} (left side) and $\cos\theta_l$ (right side) were varied from 1 to 1/9 of the total range. The open circle corresponds to standard binning. Fits were performed with the first fitting technique. 65

5.3 Values of form factor ratios calculated with different Monte Carlo volume sizes. The ranges of $\cos\theta_V$ (left side) and χ (right side) were varied from 1 to 1/9 of the total range. The open circle corresponds to standard binning. Fits were performed with the first fitting technique. 66

5.4 Weights correcting the inaccuracies in the Monte Carlo K and π identification efficiency for different ranges of track momentum. Continuous curves represent a fit to polynomial functions. 69

5.5 D momentum distributions for background subtracted data (error bars) overlaid with the similar Monte Carlo distributions. 73

5.6 Weights correcting the inaccuracies in the Monte Carlo $(p_D)_\perp$ distribution. Continuos curves represent a fit to a polynomial function. 74

5.7 Distribution of muon tracks intercepts, data (top) and Monte Carlo (bottom), at the z-position of the 16th drift chamber. The points were determined by their x and y positions measured in cm. 75

5.8 The values of form factor ratios for different background weights. 79

5.9 Distributions of kinematic variables for WS events within the signal region (crosses), overlaid with two extreme distributions of background (continuous and dotted lines). 81

Reproduced with permission of the copyright owner. Further reproduction prohibited without permission.

5.10 Distributions of kinematic variables outside the signal region ($M_{K\pi}$ not in (0.85; 0.94) GeV). RS events are shown as black dots, overlaid with the corresponding distributions of WS events in the signal region. 82

5.11 Stability of R_2, R_V and R_3 against a cut on the minimum allowed value of q^2/q^2_{max}. Only statistical errors are shown. 86

5.12 Values of R_2 , R_V and R_3 for varying cuts on M_{min}. The lower bound of M_{min} was varied from 1.5 to 1.7 GeV holding the upper bound constant at 2.0 GeV (left side plots). The upper bound of M_{min} was varied from 1.9 to 2.1 GeV holding the lower bound constant at 1.6 GeV (right side plots). Open circles correspond to standard cuts on M_{min}. 88

6.1 Background subtracted data distributions (cross hatches) overlaid with Monte Carlo (dashed line) with best fit values for the form factor ratios. . . 91

6.2 Comparison of single-variable distributions of background-subtracted data (crosses) with Monte Carlo predictions (dashed histograms) using best-fit values for the form factor ratios. In the plots of $\cos\theta_l$ and $\cos\theta_V$ data has been divided into two ranges of q^2/q^2_{max}, while the distribution of χ is shown for two ranges of $\cos\theta_V$. 92

6.3 Top: Comparison of experimental measurements of form factor ratios r_V and r_2 for $D^+ \to \overline{K}^{*0}\ell^+\nu_\ell$ in the muon (μ), electron (e) and combined ($\mu + e$) channels. The smaller error bars indicate the statistical errors and the larger ones indicate the statistical and sytematic errors added in quadrature. Bottom: Comparison of theoretical predictions with the E791 ($\mu + e$) result. 97

Reproduced with permission of the copyright owner. Further reproduction prohibited without permission.

B.1 (a) Centerline in the position and TDC correlation plot. The equation for the line is 10x + y -9150 = 0, where y is the projected X-position on the Y wall and x is the muon TDC from Y wall. (b) Distribution of the DIST variable for RS and WS events. 106

C.1 A correctly-normalized distribution function $f(x)$ is shown in the top plot. The "average" distribution function $\bar{f}(x)$ (defined in the text) is shown in the bottom plot. The nominal volume equals to the full range of x. 110

C.2 The "average" distribution functions $\bar{f}(x)$'s when the nominal volume is one fifth (top) and one tenth (bottom) from the full range of x. 111

C.3 Values of the form factor ratios, uncorrected (open circles) and corrected (black bullets) for the systematic shifts. The horizontal axis represents the fraction nominal volume to the total phase-space volume in log scale. The values of the nominal volume are the same as those in Table C1 and Table C2. 113

Reproduced with permission of the copyright owner. Further reproduction prohibited without permission.

List of Tables

1.1 Theoretical predictions for the form factors R_2 and R_V, and the average of previous experimental results. 13

2.1 Characteristics of the E791 PWC systems. 20

2.2 Characteristics of the E791 drift chambers. 21

2.3 Some important characteristics of the two Čerenkov detectors C1 and C2. The threshold momentum for each Čerenkov detector indicates the point at which a given particle starts to emit Čerenkov radiation. 23

2.4 Čerenkov Separation for π, K and p 24

2.5 Important Characteristics of the SLIC. 27

2.6 Characteristics of the X and Y muon walls. 29

3.1 Summary of the cuts chosen by CART to produce the clean $D^+ \rightarrow \bar{K}^{*0}\mu^+\nu_\mu$ sample. Each column gives the coefficients of the six parameters plus a constant which represents the cut $C_1 * Sigma + C_2 * SDIP + C_3 * SDZ + C_4 * Sratio + Constant > 0$. 39

4.1 Monte Carlo events passing each set of cuts. 48

4.2 Resolutions of the kinamatic variables reconstructed with the lower and higher neutrino momentum solutions. 49

Reproduced with permission of the copyright owner. Further reproduction prohibited without permission.

4.3 The widths of the differencies $x_{rec} - x_{gen}$ when both sources of smearing are present (RMS1) and when the decays are affected only by the detector smearing (RMS2). 52

4.4 Weights correcting the inaccuracies in the Monte Carlo K and π identification efficiency for different ranges of track momentum. 60

5.1 Values of form factor ratios calculated with various conditions on the minimum number of Monte Carlo points (n_{MCmin}). 67

5.2 The values of form factor ratios calculated with different combinations of hadron ID corrections. 68

5.3 Systematic errors due to hadron identification efficiencies. 70

5.4 Values of form factor ratios calculated with the unbinned method, for different cuts on the lower bound of muon momentum. Fit values were not corrected for systematic shifts. 71

5.5 The values of form factor ratios, calculated with the unbinned method, for different ways (described in the text) to solve the ambiguity of muon candidate. 72

5.6 The systematic errors due to muon identification. 72

5.7 The values of form factor ratios calculated with different combinations of $(p_D)_\perp$ corrections. 73

5.8 Study of the systematic uncertainties associated with spectrometer acceptance effects. 77

5.9 The number of events and the values of form factors calculated with the unbinned method for 14 sets of CART cuts. 78

5.10 Values of form factor ratios calculated with different background weights. Fits were performed with the second fitting technique. 80

Reproduced with permission of the copyright owner. Further reproduction prohibited without permission.

5.11 Results of systematic checks of data selection. The fits were performed with the unbinned loglikelihood method and corrections for systematic shifts were applied. 84

5.12 The main contributions to form-factor uncertainties. 89

6.1 Comparison of E791 results with previous experimental results. The E791 electron result for r_V is 0.06 higher than the value reported in Ref. [5] because we have corrected for inaccuracies in the earlier modeling of the D^+ transverse momentum. 93

6.2 Comparison of the measured form factor values $A_1(0)$, $A_2(0)$ and $V(0)$ with theoretical predictions. 94

6.3 The main contributions to form factor uncertainties measured for $D^+ \to \overline{K}^{*0}\ell^+\nu_\ell$. 96

C.1 The values of the systematic shifts measured for different values of the nominal volume. The first column shows the number of bins for each kinematic variable. 112

C.2 The values of the form factor ratios uncorrected and corrected for the systematic shifts. The corrections were done by subtracting the values of the systematic shifts listed in Table C1. 114

Reproduced with permission of the copyright owner. Further reproduction prohibited without permission.

ACKNOWLEDGMENTS

First of all, I wish to thank members of Kansas State HEP group Bill Reay, Noel Stanton, Ron Sidwell, Tim Bolton for helping me to discover, to understand and to love this wonderful field, which is experimental high energy physics. Also, I owe a great debt to Larry Weaver for his great lectures and for the enlightening discussions on theoretical issues.

This work would have never reached the final form without the assistance from Fermilab staff, Jeff Appel and Jean Slaughter, and from the other participants to E791 Collaboration. Especially, I would like to thank Pat Burchat, Mike Sokoloff and Milind Purohit for their useful comments and suggestions.

As a graduate student I learned not only from professors, but also from other graduate students. I wish to thank former or actual graduate students Nick Witchey, Arun Tripathi, Shih-Wen Yang, Jesse Goldman, Drew Alton, Max Goncharov and Renata Zalizniak for sharing their knowledge with me.

Reproduced with permission of the copyright owner. Further reproduction prohibited without permission.

Dedicated To Mother and Father

Reproduced with permission of the copyright owner. Further reproduction prohibited without permission.

Chapter 1

Theoretical Motivation

Weak semileptonic decays of hadrons provide a valuable way for testing the structure of weak currents, for probing the quark structure of hadrons, and for extracting fundamental information on the quark mixing matrix. Charmed meson semileptonic decays are mainly used for testing the structure of the weak currents. Strong interaction effects play a major role in the weak decays of hadrons containing heavy quarks. Semileptonic charm decays such as $D^+ \rightarrow \overline{K}^{*0}\ell^+\nu_\ell$ are an especially clean way to study these effects, because all information about the strong interactions is contained in a few form factors. The goal of this work is to measure the values of the form factor ratios for a specific charm semileptonic decay and to compare results with specific models.

According to Heavy Quark Effective Theory, the values of form factors for charm semileptonic decays can be related to those in certain bottom decays. Combining experimental data obtainable from $B \rightarrow \rho\ell\overline{\nu}_\ell$ and the measured form factors for charm semileptonic decays can lead to a model independent determination of $\mid V_{ub} \mid$ ([1]). The decay rate $\Gamma(B \rightarrow \rho\ell\overline{\nu}_\ell)$ is related to $\mid V_{ub} \mid^2$ and to a function $S^{(B\rightarrow\rho)}$ of the B-meson decay form factors: $\Gamma(B \rightarrow \rho\ell\overline{\nu}_\ell) \propto \mid V_{ub} \mid^2 \cdot S^{(B\rightarrow\rho)}(FF's)$. The form factors for $B \rightarrow \rho\ell\overline{\nu}_\ell$ can be related to those corresponding to the decay $D \rightarrow K^*\overline{\ell}\nu_l$ using two approximate symmetries:

Reproduced with permission of the copyright owner. Further reproduction prohibited without permission.

- heavy quark symmetry: FF's $(D \to K^\star) \Rightarrow FF's(B \to K^\star)$.
- SU(3) flavor symmetry: FF's $(B \to K^\star) \Rightarrow FF's(B \to \rho)$.

Determination of the $\mid V_{ub} \mid$ in this way is biased by theoretical uncertainties estimated at about 20%.

1.1 Form Factors in the Standard Model

The Feynman diagram for the decay $D^+ \to \overline{K}^{\star 0}\ell^+\nu_\ell$ is shown in Fig. 1.1. Assuming a point-like interaction, the invariant amplitude is proportional to the product of the lepton and hadron currents L_μ and H^μ:

$$A(D^+ \to \overline{K}^{\star 0}) = \frac{G_F}{\sqrt{2}} \cdot V_{cs} \cdot L_\mu \cdot H^\mu \tag{1.1}$$

where G_F is the Fermi coupling constant for the weak interaction and V_{cs} is the CKM matrix element corresponding to the coupling of the charm quark to the strange.

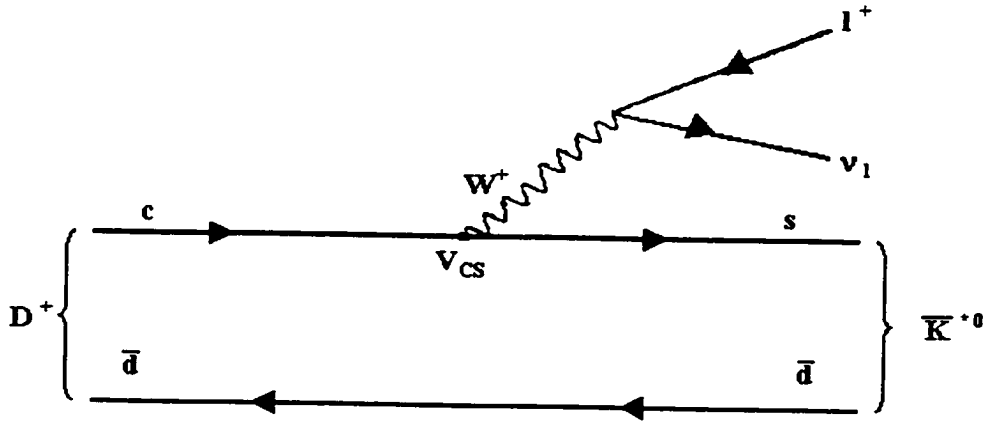

Figure 1.1: Semileptonic decay $D^+ \to \overline{K}^{\star 0}\ell^+\nu_\ell$.

The lepton current L^μ has a standard $V - A$ structure:

$$L_\mu = \bar{u}_\nu \gamma_\mu (1 - \gamma_5) v_l \tag{1.2}$$

Reproduced with permission of the copyright owner. Further reproduction prohibited without permission.

where $\bar{u}_e$ and v_ν are the standard Dirac spinors. The expression of the hadron current is more complicated because both the initial and final quarks are not free. However, the hadron current H^μ is still constrained by three requirements:

1. It must be a four-vector.
2. It must be built up from all independent four-vectors that are relevant for the decay mode.
3. It must be linear in the polarization vector ϵ of the final vector meson $K^\star$.

For this charm semileptonic decay there are three independent four-vectors: the four-momentum of the parent particle p_D, the four-momentum of the vector meson $p_{K^\star}$ and the polarization of the vector meson ϵ. The hadron current H_μ does not have a well-determined parity. Its most general expression contains both vector (V^μ) and axial-vector (A^μ) components [2, 3].

$$\langle p_{K^\star}, \epsilon \mid V^\mu \mid p_D \rangle = g(q^2)\epsilon^{\mu\nu\rho\sigma}\epsilon^\star_\nu (p_D + p_{K^\star})_\rho (p_D - p_{K^\star})_\sigma \tag{1.3}$$

$$\begin{aligned} \langle p_{K^\star}, \epsilon \mid A^\mu \mid p_D \rangle &= f(q^2)\epsilon^{\star\mu} + a_+(q^2)(\epsilon^\star \cdot p_D)(p_D + p_{K^\star})^\mu + \\ &\quad a_-(q^2)(\epsilon^\star \cdot p_D)(p_D - p_{K^\star})^\mu \end{aligned} \tag{1.4}$$

where q^2 is the invariant mass squared of the virtual W.

The hadron current is parametrized by four Lorentz-invariant form factors $g(q^2)$, $f(q^2)$, $a_+(q^2)$ and $a_-(q^2)$. The first of these is related to the vector component of the hadron current and the other three to its axial part. In practice, dimensionless linear combinations of $g(q^2)$, $f(q^2)$, $a_+(q^2)$ and $a_-(q^2)$ denoted by $V(q^2)$, $A_1(q^2)$, $A_2(q^2)$, $A_3(q^2)$, are more often used. Relationships between the two sets of form factors are given by:

$$g(q^2) = \frac{i}{m_D + m_{K^\star}} V(q^2) \tag{1.5}$$

$$f(q^2) = i(m_D + m_{K^\star})A_1(q^2) \tag{1.6}$$

Reproduced with permission of the copyright owner. Further reproduction prohibited without permission.

$$a_+(q^2) = \frac{-i}{m_D + m_{K^*}} A_2(q^2) \tag{1.7}$$

$$a_-(q^2) = \frac{i}{q^2}\left[2m_{K^*}A_3(q^2) - (m_D + m_{K^*})A_1(q^2) + (m_D - m_{K^*})A_2(q^2)\right] \tag{1.8}$$

Limited size of data samples has so far precluded precise measurement of the q^2 dependence of the form factors, and the q^2 dependence is assumed to be given by the nearest-pole dominance model:

$$A_{1,2,3}(q^2) = \frac{A_{1,2,3}(0)}{1 - \frac{q^2}{M_A^2}} \tag{1.9}$$

$$V(q^2) = \frac{V(0)}{1 - \frac{q^2}{M_V^2}} \tag{1.10}$$

with $M_A = 2.5$ GeV/c^2 and $M_V = 2.1$ GeV/c^2 given by the lowest lying $c\bar{s}$ states with appropriate quantum numbers [4].

1.2 The Differential Decay Rate

Form factor ratios were extracted from data by measuring the differential decay rate of the process $D^+ \to \overline{K}^{*0}\ell^+\nu_\ell$. This decay is described as a succession of 2-body decays; the D^+ first decays into a $\overline{K}^{*0}$ and a virtual W^+, then the $\overline{K}^{*0}$ decays into a K^- and a π^+, and the W^+ into ℓ^+ and ν_ℓ. Including phase-space, the decay rate can be written as:

$$d\Gamma = \frac{1}{2M_D} \mid A(D \longrightarrow K\pi l\nu) \mid^2 d\Phi_4 (2\pi)^4 \delta^4(p_D - p_K - p_\pi - p_\nu) \tag{1.11}$$

With four particles in the final state, the phase-space associated to this decay is 12-dimensional:

$$d\Phi_4 = \frac{d^3p_K}{(2\pi)^3 2E_K} \cdot \frac{d^3p_\pi}{(2\pi)^3 2E_\pi} \cdot \frac{d^3p_l}{(2\pi)^3 2E_l} \cdot \frac{d^3p_\nu}{(2\pi)^3 2E_\nu} \tag{1.12}$$

However, using energy and momentum conservation, expressed by the delta function in the formula of the decay rate (1.11), the number of degrees of freedom reduces from 12 to 8. There are also three irrelevant angles: two angles that define the axis of K^* and W in the D rest frame, and one angle corresponding to a rotation around this axis.

Reproduced with permission of the copyright owner. Further reproduction prohibited without permission.

Integrating over these angles reduces the number of degrees of freedom to 5. Finally, integrating over the invariant mass of the $\overline{K}^{*0}$, which is not related to the form factors, the phase-space relevant for this analysis is 4-dimensional. The definitions of the four independent kinematic variables, used in this analysis are very similar to those used in Ref. [2]: the square of the momentum transfer (q^2), the polar angle θ_V in the $\overline{K}^{*0}$ rest frame between the π^+ and D^+, the polar angle θ_l in the W^+ rest frame between the ν_μ and D^+, and the azimuthal angle χ in the D^+ rest frame between the $\overline{K}^{*0}$ and W^+ decay planes (Fig. 1.2). The definition we use for the polar angle θ_l is related to the definition used in Ref. [2] by $\theta_l \to \pi - \theta_l$.

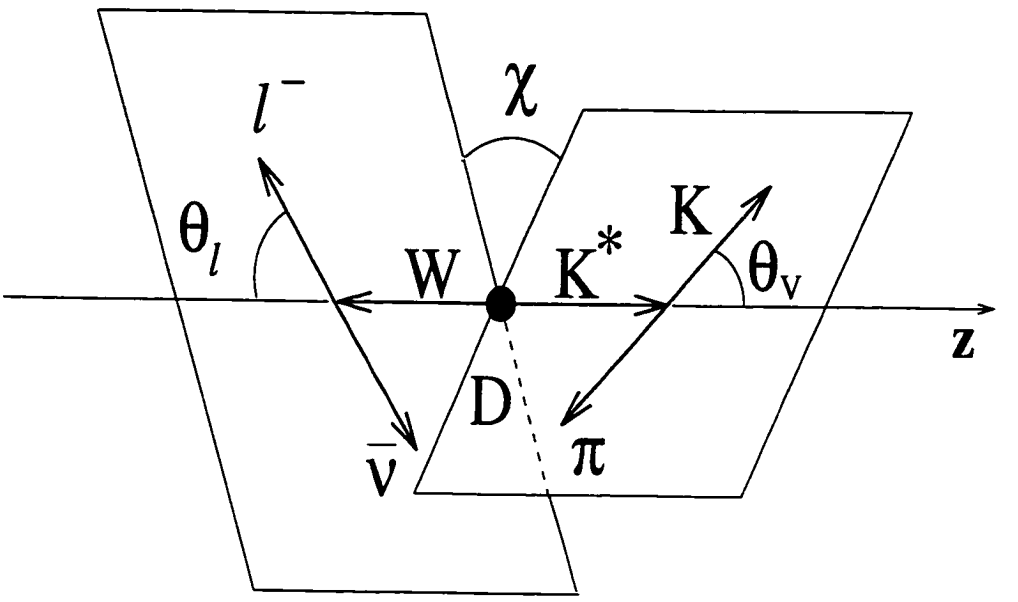

Figure 1.2: Definition of the angles θ_l , θ_V and χ in the decay $D \longrightarrow K^* l\nu$.

In terms of these variables the differential decay rate is given by:

$$\frac{d\Gamma}{dq^2 d(\cos\theta_l) d(\cos\theta_V) d\chi} = \frac{3}{4(4\pi)^4} \cdot \frac{p_K \cdot q^2}{M_D^2} \cdot B(K^* \longrightarrow K^- \pi^+) \mid A \mid^2 \tag{1.13}$$

The expression for the decay amplitude $\mid A \mid^2$ has still to be determined. Its explicit expression is much shorter in the limit of vanishing charged lepton mass.

Reproduced with permission of the copyright owner. Further reproduction prohibited without permission.

1.3 The Case of Zero Lepton Mass

In the limit of vanishing lepton mass, the time component of the lepton current (Eqn. 1.2) is zero in the $\ell\nu$ frame. Since the amplitude of the decay rate contains the scalar product of the lepton and hadron currents, only the spatial part of the hadron current is relevant for the differential decay rate. It is convenient to expand the spatial part of the hadron current H_μ in terms of a helicity basis of the virtual W.

$$\mathbf{H} = H_+\mathbf{e}_+ + H_-\mathbf{e}_- + H_0\mathbf{e}_0 \tag{1.14}$$

where $\mathbf{e}_\pm = \frac{1}{\sqrt{2}}(\mp\mathbf{x} - i\mathbf{y})$, $\mathbf{e}_0 = \mathbf{z}$. The helicity amplitudes $H_\pm$ and H_0 are related to the form factors $A_{1,2}(q^2)$ and $V(q^2)$:

$$H_0(q^2) = \frac{1}{2m_{K^\star}\sqrt{q^2}}\left[(m_D^2 - m_{K^\star}^2 - q^2)(m_D + m_{K^\star})A_1(q^2) - \frac{4m_D^2 p_{K^\star}}{m_D + m_{K^\star}}A_2(q^2)\right] \tag{1.15}$$

$$H_\pm(q^2) = (m_D + m_{K^\star})A_1(q^2) \mp \frac{2m_D p_{K^\star}}{m_D + m_{K^\star}}V(q^2) \tag{1.16}$$

In the above expressions, $p_{K^\star}$ is the 3-momentum of the final state vector meson $K^\star$ in the D meson rest frame. It is given by [1]:

$$p_{K^\star}(q^2) = \left[(m_D^2 - m_{K^\star}^2 - q^2)^2 - 4m_{K^\star}^2 q^2\right]^{\frac{1}{2}}/2m_D \tag{1.17}$$

As a consequence of this approximation (vanishing lepton mass) the form factor A_3 is not relevant for $D^+ \to \overline{K}^{\star 0}\ell^+\nu_\ell$ because the spatial part of $(p_D - p_{K^\star})$ vanishes when evaluated in the $\ell\nu$ frame (Eqns. 1.4 and 1.8).

Following KS[2] and GS[3] and ignoring the lepton mass terms, the expression for the differential decay rate is:

$$\frac{d\Gamma}{dq^2 d\cos\theta_l d\cos\theta_V d\chi} = \frac{3}{8(4\pi)^4}\cdot G_F^2 \cdot |V_{cs}|^2 \frac{p_{K^\star} q^2}{M_D^2}\cdot B(K^\star \longrightarrow K^-\pi^+) \times$$

[1] Due to the measurement uncertainties, the expression under the square root in Eqn. 1.17 might be negative. The way these "unphysical" events are treated is described in Appendix A.

Reproduced with permission of the copyright owner. Further reproduction prohibited without permission.

$$
\begin{aligned}
&\times\{(1+\cos\theta_l)^2\sin^2\theta_V|\ H_+(q^2)\ |^2 + \\
&+(1-\cos\theta_l)^2\sin^2\theta_V|\ H_-(q^2)\ |^2 + \\
&+4\sin^2\theta_l\cos^2\theta_V|\ H_0(q^2)\ |^2 + \\
&+4\sin\theta_l(1+\cos\theta_l)\sin\theta_V\cos\theta_V\cos\chi H_+(q^2)H_0(q^2) - \\
&-4\sin\theta_l(1-\cos\theta_l)\sin\theta_V\cos\theta_V\cos\chi H_-(q^2)H_0(q^2) - \\
&-2\sin\theta_l{}^2\sin\theta_V{}^2\cos 2\chi H_+(q^2)H_-(q^2)\}
\end{aligned}
\tag{1.18}
$$

The definition of the azimuthal angle χ depends on the choice of the local system of coordinates. As in Ref. [2], the orientation of the plane defined by $\mathbf{p_{K^*}}$ and $\mathbf{p_K}$ is taken along $\hat{\mathbf{y}} = \frac{\mathbf{p_K}\times\mathbf{p_{K^*}}}{|\mathbf{p_K}\times\mathbf{p_{K^*}}|}$. With this convention the x component of $\mathbf{p_K}$ is always ≥ 0. The angle χ is the azimuthal angle of the charged lepton momentum $\mathbf{p}_\ell$ (evaluated in the rest frame of the W) with respect to the local system of coordinates: $\hat{\mathbf{z}} = \frac{\mathbf{p_{K^*}}}{|\mathbf{p_{K^*}}|}$, $\hat{\mathbf{y}} = \frac{\mathbf{p_K}\times\mathbf{p_{K^*}}}{|\mathbf{p_K}\times\mathbf{p_{K^*}}|}$ and $\hat{\mathbf{x}} = \hat{\mathbf{y}}\times\hat{\mathbf{z}}$. In the particular case when the planes $(\mathbf{p_K};\mathbf{p_{K^*}})$ and $(\mathbf{p}_\ell;\mathbf{p_W})$ are parallel, the value of χ is 0 if $(\mathbf{p}_\ell)_x \geq 0$, or is π otherwise.

1.4 The Effects of the Lepton Mass

In the case of nonzero lepton mass, the time component of the hadron current must be taken into account. Using the notations of Ref. [2] helicity amplitudes and the form factors are related by:

$$H_\pm = f(q^2) \mp 2m_D p_{K^*} g(q^2) \tag{1.19}$$

$$H_0(q^2) = \frac{m_D}{2m_{K^*}\sqrt{y}}\left\{(1-\frac{m_{K^*}^2}{m_D^2}-y)f(q^2) + 4p_{K^*}^2 a_+(q^2)\right\} \tag{1.20}$$

$$H_t(q^2) = \frac{p_{K^*}}{m_{K^*}\sqrt{y}}\left\{f(q^2) + m_D^2(1-\frac{m_{K^*}^2}{m_D^2})a_+(q^2) + m_D^2 y a_-(q^2)\right\} \tag{1.21}$$

where $y = \frac{q^2}{m_D^2}$ and the connection between the sets of form factors $g(q^2)$, $f(q^2)$, $a_+(q^2)$, $a_-(q^2)$ and $V(q^2)$, $A_1(q^2)$, $A_2(q^2)$, $A_3(q^2)$ is given by Eqns. 1.5 to 1.8.

Compared to the case of vanishing lepton mass, there is an additional helicity amplitude H_t which contains the form factor $a_-(q^2)$ and implicitly $A_3(q^2)$ (Eqn. 1.8). The

Reproduced with permission of the copyright owner. Further reproduction prohibited without permission.

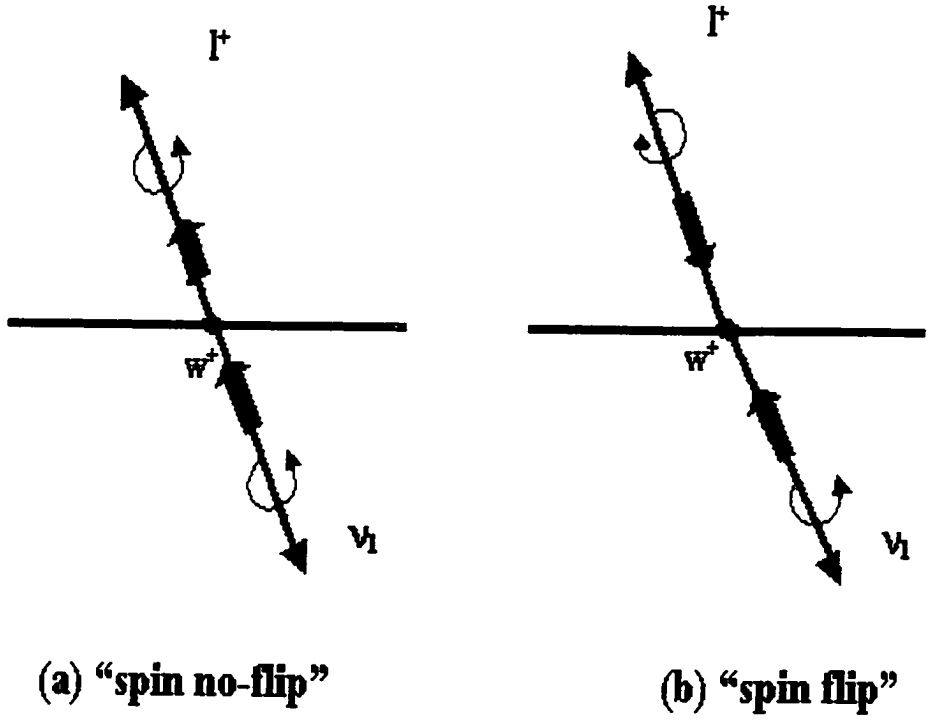

Figure 1.3: Spin-1 component of the W boson (left); Spin-0 component of the W boson.

form factor $A_3(q^2)$ is relevant only in the limit of non-vanishing lepton mass. The helicity amplitude H_t probes the spin-0 component of the W boson and is highly suppressed due to the $V-A$ structure of the weak currents (Fig. 1.3). The extra amplitudes in the differential decay rate generated by the additional helicity amplitude H_t are usually called "spin-flip" amplitudes because the relative orientation of the lepton spins in the W rest frame is opposite to what one might expect if the charged lepton mass is ignored (Fig. 1.3). In addition to the suppression of the "spin-flip" amplitudes due to the $V-A$ structure of the lepton current, there is another reason to believe that these extra amplitudes play a minor role even if the charged lepton has a relatively large mass. As shown in Fig. 1.3, "spin-flip" amplitudes are associated with the spin-0 (scalar) component of the W boson. Since the parent particle (the D^+) is a pseudo-scalar and the $\overline{K}^{*0}$ meson is a vector, the scalar W^+ and the vector $\overline{K}^{*0}$ must have a relative angular momentum $L=1$ in order to

Reproduced with permission of the copyright owner. Further reproduction prohibited without permission.

satisfy total angular momentum conservation. A P-wave decay of the D^+ meson should be highly unfavored in comparison with the normal S-wave decay, simply because of the small spatial extent of the D^+ meson. The helicity amplitude H_t is proportional to the form factor $A_3(q^2)$, and is expected to be small.

In general, with non-zero lepton mass the differential decay rate is given by:

$$\begin{aligned}
\frac{d\Gamma}{dq^2 d\cos\theta_l d\cos\theta_V d\chi} \propto \quad & +\frac{3}{8}(1+\cos^2\theta_l)\frac{3}{4}\sin^2\theta_V d\Gamma_U/dq^2 \\
& +\frac{3}{4}\sin^2\theta_l\frac{3}{2}\cos^2\theta_V d\Gamma_L/dq^2 \\
& -\frac{3}{4}\sin^2\theta_l\cos 2\chi\frac{3}{4}\sin^2\theta_V d\Gamma_T/dq^2 \\
& +\frac{9}{16}\sin 2\theta_l\cos\chi\sin 2\theta_V d\Gamma_I/dq^2 \\
& +\frac{3}{4}\cos\theta_l\frac{3}{4}\sin^2\theta_V d\Gamma_P/dq^2 \\
& +\frac{9}{8}\sin\theta_l\cos\chi\sin 2\theta_V d\Gamma_A/dq^2 \\
& +\frac{3}{4}\sin^2\theta_l\frac{3}{4}\sin^2\theta_V d\tilde{\Gamma}_U/dq^2 \\
& +\frac{3}{2}\cos^2\theta_l\frac{3}{2}\cos^2\theta_V d\tilde{\Gamma}_L/dq^2 \\
& +\frac{3}{4}\sin^2\theta_l\cos 2\chi\frac{3}{4}\sin^2\theta_V 2d\tilde{\Gamma}_T/dq^2 \\
& -\frac{9}{8}\sin 2\theta_l\cos\chi\sin 2\theta_V d\tilde{\Gamma}_I/dq^2 \\
& +\frac{3}{2}\cos^2\theta_V\frac{1}{2}d\tilde{\Gamma}_S/dq^2 \\
& -3\cos\theta_l\frac{3}{2}\cos^2\theta_V d\tilde{\Gamma}_{SL}/dq^2 \\
& +\frac{9}{4}\sin\theta_l\cos\chi\sin 2\theta_V d\tilde{\Gamma}_{ST}/dq^2
\end{aligned} \tag{1.22}$$

where

$$d\Gamma_i/dq^2 = \frac{G_F^2|V_{cs}|^2}{96\pi^3}\frac{p_{K^*}q^2}{m_D^2}\left(1-\frac{m_l^2}{q^2}\right)^2\tilde{H}_i \tag{1.23}$$

$$d\tilde{\Gamma}_i/dq^2 = \frac{m_l^2}{2q^2}d\Gamma_i/dq^2 \tag{1.24}$$

Following KS[2] the notations $i \equiv \Gamma_i$, and $\tilde{i} \equiv \tilde{\Gamma}_i$ stand for:

U $\propto$ $\tilde{H}_U = \ |H_+|^2 + |H_-|^2$ unpolarized transversal

Reproduced with permission of the copyright owner. Further reproduction prohibited without permission.

P	$\propto$	$\tilde{H}_P =$	$\mid H_+ \mid^2 - \mid H_- \mid^2$	parity odd
L	$\propto$	$\tilde{H}_L =$	$\mid H_0 \mid^2$	longitudinal
S	$\propto$	$\tilde{H}_S =$	$3\mid H_t \mid^2$	scalar
SL	$\propto$	$\tilde{H}_{SL} =$	$Re(H_t \cdot H_0^\star)$	scalar- longitudinal interference
T	$\propto$	$\tilde{H}_T =$	$Re(H_+ \cdot H_-^\star)$	transverse interference
I	$\propto$	$\tilde{H}_I =$	$\frac{1}{2}Re(H_+ \cdot H_0^\star + H_- \cdot H_0^\star)$	trans.-longi. interference
A	$\propto$	$\tilde{H}_A =$	$\frac{1}{2}Re(H_+ \cdot H_0^\star - H_- \cdot H_0^\star)$	parity asymmetric
ST	$\propto$	$\tilde{H}_{ST} =$	$\frac{1}{2}Re(H_+ \cdot H_t^\star + H_- \cdot H_t^\star)$	scalar-trans. interference

In the limit of vanishing lepton mass, the above equation reduces to Eqn. 1.18. The "spin-flip" amplitudes are those containing the helicity amplitude H_t: $\tilde{H}_S$, $\tilde{H}_{SL}$ and $\tilde{H}_{ST}$.

There are two main effects caused by the mass of the lepton m_l: a) There is an overall kinematic factor of $(1 - m_l^2/q^2)^2$ which suppresses the decay rate at low q^2. In particular, this suppression affects the longitudinal amplitude H_0, which would otherwise be large in this region.

b) Additional amplitudes are introduced and a new form factor $A_3(q^2)$ becomes relevant. Some of the additional amplitudes are still associated with the spin-1 component of the W boson ($\tilde{H}_U$, $\tilde{H}_P$, $\tilde{H}_L$, $\tilde{H}_T$, $\tilde{H}_I$, $\tilde{H}_A$) and the others ($\tilde{H}_S$, $\tilde{H}_{SL}$, $\tilde{H}_{ST}$) are the "spin-flip" amplitudes associated with the spin-0 component of the W boson. All additional amplitudes are suppressed by a factor m_ℓ^2/q^2, and according to Ref. [7] contribute approximately 5% to the total integrated rate. The Monte Carlo simulation in Fig. 1.4 compares the differential decay rates (integrated over the angular kinematic variables) when the lepton mass is neglected (electronic mode) and when the lepton mass effects are included (muonic mode). In the second case (muonic mode), the contribution of the "spin-flip" amplitudes was ignored (the form factor $A_3(q^2)$ was set to zero). The contribution of the "spin no-flip" amplitudes include extra terms that have the typical overall factor $m_\ell^2/2q^2$ (Eqn. 1.22).

Reproduced with permission of the copyright owner. Further reproduction prohibited without permission.

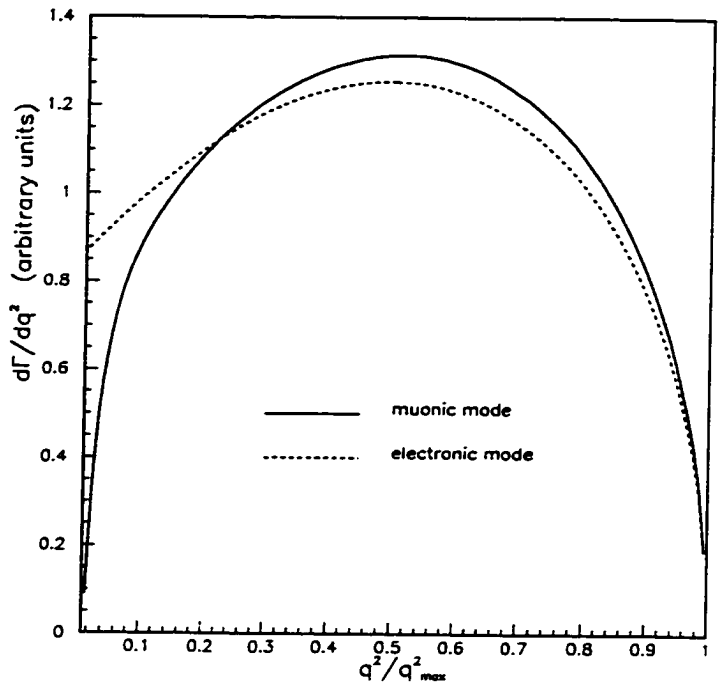

Figure 1.4: Monte Carlo simulation of differential decay rates $d\Gamma/dq^2$ for muon and electron decay modes.

1.5 Theoretical Predictions for the Form Factor Ratios

The differential decay rate (Eqn. 1.22) is a quadratic and homogeneous function of the form factors. Therefore, one form factor evaluated at $q^2 = 0$ can be factored out and included in the overall constant which contains the Fermi constant G_F, the CKM matrix element $| V |_{cs}$ and the branching fraction $B(\overline{K}^{*0} \rightarrow K^-\pi^+)$ (Eqn. 1.18). Since $A_1(q^2)$ contributes to all helicity amplitudes, it is customary to factor out this form factor evaluated at $q^2 = 0$. The parameters measured in this analysis are the form factor ratios:

$$R_V = \frac{V(0)}{A_1(0)} \tag{1.25}$$

$$R_2 = \frac{A_2(0)}{A_1(0)} \tag{1.26}$$

Reproduced with permission of the copyright owner. Further reproduction prohibited without permission.

$$R_3 = \frac{A_3(0)}{A_1(0)} \tag{1.27}$$

In principle, the values of the form factors $V(0)$, $A_1(0)$, $A_2(0)$, $A_3(0)$ can be determined from the values of the measured form factor ratios R_V, R_2, R_3 and additional information about the total decay decay rate, the D^+ lifetime, $\mid V \mid_{cs}$ and $B(\overline{K}^{*0} \rightarrow K^-\pi^+)$. Experimental uncertainties associated with these quantities propagate into the errors on the form factors $V(0)$, $A_1(0)$, $A_2(0)$, $A_3(0)$. Therefore, the comparison of the measured form factor ratios R_V, R_2, R_3 with theoretical predictions is more relevant.

Several theoretical models make predictions for the form factor ratios R_2 and R_V, as summarized in Table 1.1. These theoretical predictions are affected by large uncertainties, and none include the third ratio of form factors R_3 which is related to the lepton mass. Experimental averages calculated from four previously published results [5, 6, 7, 8] are also listed.

The calculations based on quark models estimate meson wave functions and use them to compute the matrix elements of the hadronic currents. The integrals are performed for zero-recoil momentum of the daughter meson ($q^2 = q^2_{max}$) because the $D \rightarrow K$ wave function overlap can be better estimated. The values of the form factors evaluated at $q^2 = q^2_{max}$ are extrapolated to lower q^2 assuming certain q^2-dependences. The models differ from each other in the assumptions made to evaluate the meson wave functions and the q^2-dependence of the form factors. Lattice QCD results are based on numerical calculations using a discrete space-time lattice. These are nonperturbative methods and are still plagued by large uncertainties. In general the central values obtained with lattice QCD calculations agree better with the experimental results.

Reproduced with permission of the copyright owner. Further reproduction prohibited without permission.

Table 1.1: Theoretical predictions for the form factors R_2 and R_V, and the average of previous experimental results.

Group	R_2	R_V
Quark Model		
ISGW[9]	1.0	1.4
WSB[10]	1.3	1.4
KS[2]	1.0	1.0
AW/GS[11, 3]	0.8	2.0
Stech[12]	1.06	1.55
Lattice Gauge		
BKS[13]	$0.7 \pm 0.16 \pm 0.17$	$1.99 \pm 0.22 \pm 0.33$
LMMS[14]	0.4 ± 0.4	1.6 ± 0.2
ELC[15]	0.6 ± 0.3	1.3 ± 0.2
APE[16]	0.7 ± 0.4	1.6 ± 0.3
UKQCD[17]	0.9 ± 0.2	$1.4^{+0.5}_{-0.2}$
Sum Rules		
BBD[18]	1.2 ± 0.2	2.2 ± 0.2
Experimental Average	0.74 ± 0.09	1.90 ± 0.12

Reproduced with permission of the copyright owner. Further reproduction prohibited without permission.

Chapter 2

E791 Experimental Setup

E791 is a fixed-target charm hadroproduction experiment. Charm particles were produced in the collisions of a 500 GeV/c π^- beam with five thin targets, one platinum and four diamond. The goal of this experiment was to explore charm physics with better sensitivity than previous experiments by recording a large number (about 2×10^{10}) of charm candidate events. To extract data corresponding to certain charm decay modes, the E791 spectrometer provides accurate information on:

- production and decay vertices (vertexing system).
- track trajectories (tracking system).
- track momenta (dipole magnets).
- particle identification (Čerenkov counters, calorimeters, muon walls).

The E791 spectrometer, including the target, is shown in Fig. 2.1. The spectrometer componenets relevant for this analysis are briefly described in this chapter. More details about the E791 spectrometer can be found in Ref. [19, 20, 21, 22].

Reproduced with permission of the copyright owner. Further reproduction prohibited without permission.

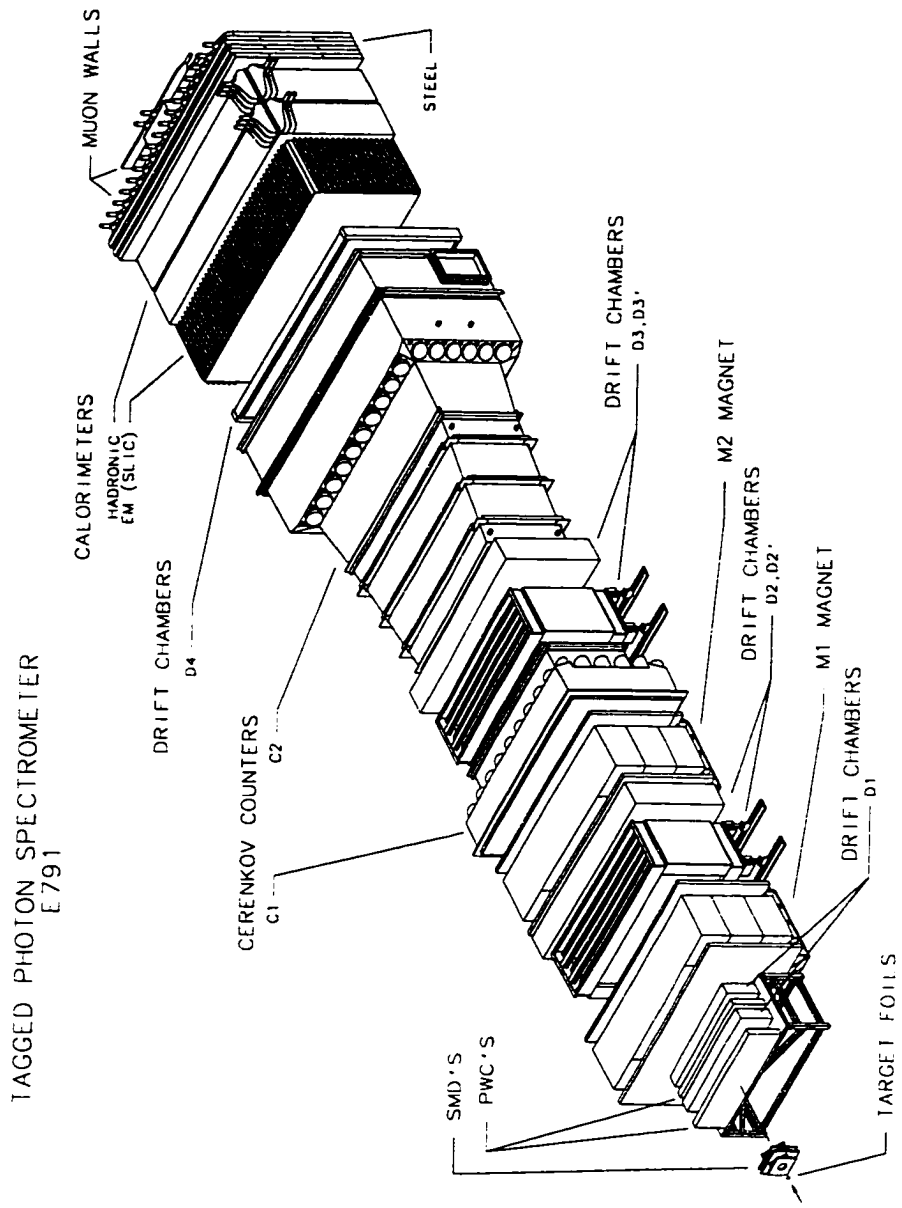

Figure 2.1: The E791 Spectrometer.

Reproduced with permission of the copyright owner. Further reproduction prohibited without permission.

2.1 Charm Production

2.1.1 Beamline

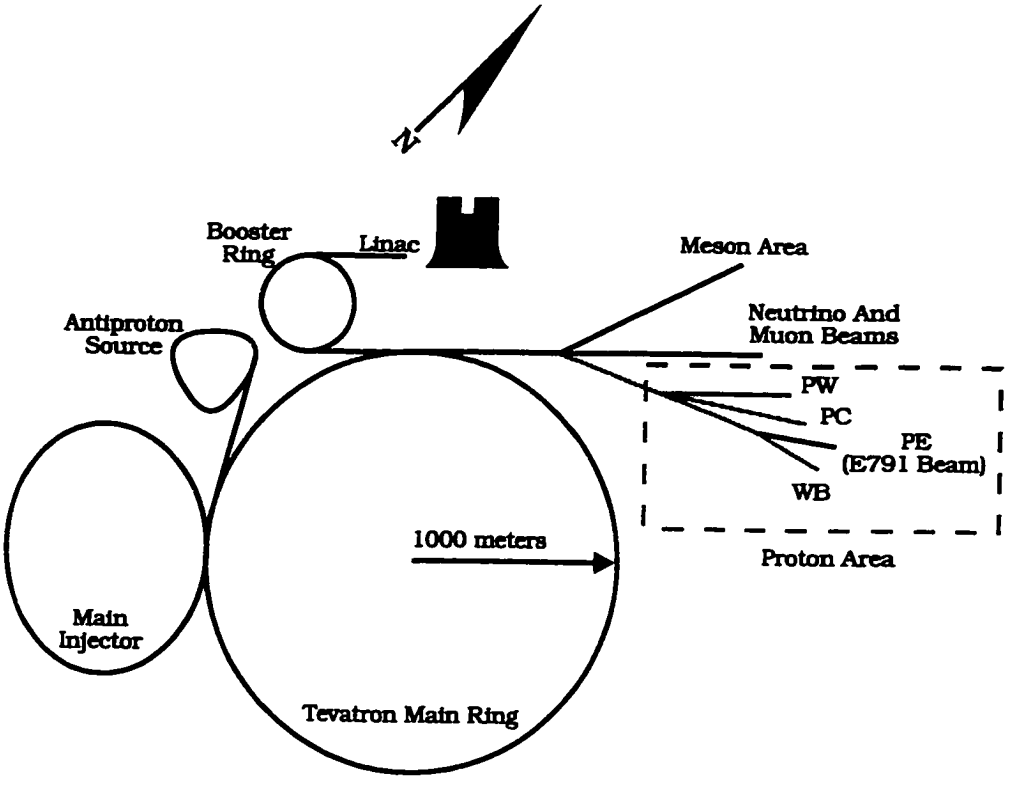

Figure 2.2: Layout of the Fermilab beam lines.

Protons of 800 GeV/c were extracted from the main ring of the Tevatron at Fermilab and injected into one of the three beamlines used in three distinct fixed-target experimental areas. Each extraction, called a spill, lasted 23 seconds out of every 57 seconds and contained about 10^{13} protons. Two teraprotons/spill were allocated to E791. Upstream from the spectrometer, the proton beam hit a 30-cm long beryllium target and high energy pions created during the collisions were charge- and momentum-selected, then collimated into a beam of negatively-charged pions with momentum (500 ± 20) GeV/c. The beam

Reproduced with permission of the copyright owner. Further reproduction prohibited without permission.

intensity typically was 2 million pions per second. The layout of the different beamlines and the Tevatron is shown in Fig. 2.2.

2.1.2 Target

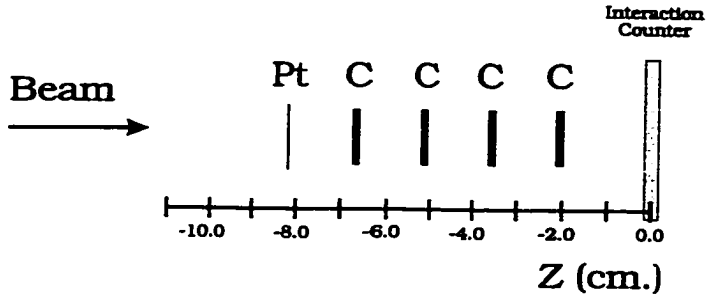

Figure 2.3: The schematic layout of the E791 target foils.

Charm particles were produced in the interactions of the 500 GeV/c negatively charged pions with a fixed target. To obtain a large sample of charm events, the target should be thick compared to the interaction length. On the other hand, a thick target increases multiple scattering and secondary interactions which mimic decays. The target design had to compromise between these conflicting requirements. The choice was to use five thin targets (Fig. 2.3). The spacing between the target foils (1.5 cm) ensures that most charm particles produced in any of the five targets decay outside the target foils. The first of the five targets was made of platinum (0.5 mm thick) and the other four were made of industrial-quality diamond (1.5 mm thick). The ideal target material should have a) high density (to maximize the production rate) and b) low Z (to minimize the multiple scattering). Platinum satisfies only the first condition. Therefore, the foil made of platinum is thinner and it is located upstream of the other target foils. Diamond is a fairly good compromise between the two conditions. The total thickness of the five targets was 6.5 mm corresponding to about 2.2% of the interaction length. The geometry

Reproduced with permission of the copyright owner. Further reproduction prohibited without permission.

of the target allowed good discrimination between the production vertex (primary) and the decay vertex (secondary). Typically, the momenta of the charm particles were about 200 GeV/c and the mean decay length was about 1 cm.

2.2 Tracking and Vertexing System

2.2.1 E791 Coordinate System

The z-axis of the E791 coordinate system was chosen to lie along the incident pion beam. The x and y axes were in the plane perpendicular to the z-axis and define a right-hand coordinate system (Fig. 2.4). The origin was just downstream of the targets.

In addition to the x, y and z axes, E791 used u, v, w and w′ directions to align the detectors. The u view axis was rotated by 20.5 degrees with respect to the positive direction of the x-axis toward the positive direction of the y-axis. Similarly, the w view axis was rotated by 60.0 degrees in the same direction as the u-axis. The v and w′ axes were rotated by -20.5 degrees and -60.0 degrees respectively with respect to the positive x-axis toward the negative direction of the y-axis (Fig. 2.4).

2.2.2 Silicon Microstrip Detectors

The silicon microstrip detector (SMD) consisted of 23 vertical planes used for precision tracking and vertexing. Six of the SMD planes were upstream of the target for accurate beam position determination, and 17 downstream for early tracking. The resolution of the SMD's is determined by the center-to-center separation (the pitch) of the conducting aluminium strips deposited on the silicon. Spatial resolutions achieved by the SMD's ranged from 7 to 15 μm in the direction perpendicular to the strips.

Reproduced with permission of the copyright owner. Further reproduction prohibited without permission.

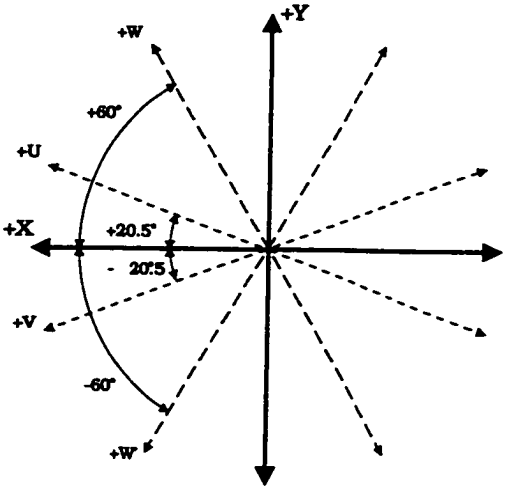

Figure 2.4: The E791 coordinate system showing x, y, u, v, w and w' axes. The z-axis points into the page.

2.2.3 Proportional Wire Chambers

Eight proportional wire chambers (PWC's) were used for beam tracking and finding the primary vertex. To increase the tracking capabilities two more PWC's were installed downstream of the target.

High energy charged particles ionize the gas inside the PWC's and resulting free electrons are collected by the nearest wire connected to a positive high voltage. The position of each charged particle is determined by the location of the wire which registered the electric pulse. Each PWC plane is perpendicular to the beam axis and can measure the position of the charged particle along the direction perpendicular to the wires. The resolution of the position measurement is proportional to the wire spacing. Table 2.1 contains the most important characteristics of the PWC's. The X′ view was offset by half a cell

Reproduced with permission of the copyright owner. Further reproduction prohibited without permission.

from the X view to improve the resolution.

PWC Characteristics		
Parameter	Upstream Station	Downstream Station
Planes	8	2
Z Position (cm)	-3117 and -1212	118.5 and 161.1
Size (cm×cm)	6.4 × 3.2	53.0 × 28.8
Wire Spacing (mm)	1.0	2.0
Views	X, X' and Y, W	X, Y

Table 2.1: Characteristics of the E791 PWC systems.

2.2.4 Drift Chambers

In addition to SMD and PWC's, the E791 tracking system was equipped with four modules of planar drift chambers containing a total of 35 vertical planes. Just as for the PWC's, the incident charged particle ionizes the gas inside the drift chamber. The freed electrons migrate to the nearest anode wire with a drift velocity which depends on the applied electric field and on the chemical and physical properties of the gas. The position of incident charged particle was determined from the time-of-flight to the anode. The resolution of the drift chambers ranged from 250 to 350 μm.

The first module of drift chamber planes (D1) was located upstream of the first analysis magnet M1 and together with SMD and PWC's, provided information about the first part of the track trajectory. The second module (D2) was located between the two bend magnets. The third drift chamber module (D3) was positioned after the second magnet M2 and before the Čerenkov counters. The last module (D4) was located past the Čerenkov counters and just before the calorimeters. The characteristics of the four drift chamber modules are summarized in Table 2.2.

Reproduced with permission of the copyright owner. Further reproduction prohibited without permission.

DC Characteristics				
Parameter	D1	D2	D3	D4
Z Positions (cm)	142.5 to 183.7	381.4 to 500.8	928.1 to 1047.1	1738.0 to 1749.2
Planes	8	12	12	3
Assemblies	2	4	4	1
Views	X, X', U, V	U, X, V	U, X, V	U, X, V
U, V Cell Size (cm)	0.476	0.892	1.487	2.97
X, X' Cell Size (cm)	0.446	0.953	1.588	3.18
Size (cm×cm)	126 × 71	285 × 143	323 × 143	511 × 259
Resolution (μm)	400	300	300	450

Table 2.2: Characteristics of the E791 drift chambers.

2.3 Momentum and Charge Measurement

E791 was equipped with two large-aperture, copper-coil magnets for momentum and charge measurement. The charged particles detected by E791 spectrometer have a large boost along the beam axis. Therefore, to a good approximation, the change of the transverse momentum produced by the magnetic field, referred to as p_T kick, does not depend on the total track momentum. The track trajectory is bent in the horizontal plane and the trajectory's curvature (measured by the tracking system) is inversely proportional to the track momentum. The values of the p_T kick for the two magnets were 212 MeV/c and 320 MeV/c respectively and were oriented in the same direction.

Reproduced with permission of the copyright owner. Further reproduction prohibited without permission.

2.4 Particle Identification

2.4.1 Čerenkov Counters

In this analysis the hadrons (kaons and pions) were identified with two Čerenkov threshold counters (C1 and C2) filled with different gas mixtures. A charged particle passing through a Čerenkov counter emits light (Čerenkov radiation) if it has a momentum greater than a threshold value p_{th}:

$$p_{th} = \frac{mc}{\sqrt{n^2 - 1}} \tag{2.1}$$

where m is the particle mass and n is the gas mixture index of refraction. For a given particle, the threshold momenta are different in C1 and C2 because the refraction indices are different. The discrimination power between different particle types is better in certain momentum ranges. For example, in the momentum range 20 to 36 GeV/c a pion would emit light in both C1 and C2, a kaon would emit light only in C1 and a proton would not emit light in either C1 or C2. Some of the Čerenkov counters characteristics are shown in Table 2.3. The particles best separated are shown in Table 2.4 for various momentum ranges.

The light emitted by charged particles traversing a Čerenkov detector was collected by spherical mirrors coupled to light collecting devices called Winston cones. Using many mirrors allows the simultaneous detection of charged particles whose light cones do not overlap at the position of the mirrors. The views of the two Čerenkov counters are shown in Figures 2.5 and 2.6 and the arrangement of the mirrors is shown in Fig. 2.7. The Winston cones funnel the light collected by the mirrors into a photomultiplier tube (PMT). For each particle type the number of photons emitted as Čerenkov radiation can be predicted in terms of particle momentum [23]. Based on this knowledge and on the observed number of photons, a probability is assigned to each charged particle for being an electron, a muon, a pion, a kaon or a proton. In this analysis, the information from Čerenkov detectors was useful only for identifying the kaons and pions.

Reproduced with permission of the copyright owner. Further reproduction prohibited without permission.

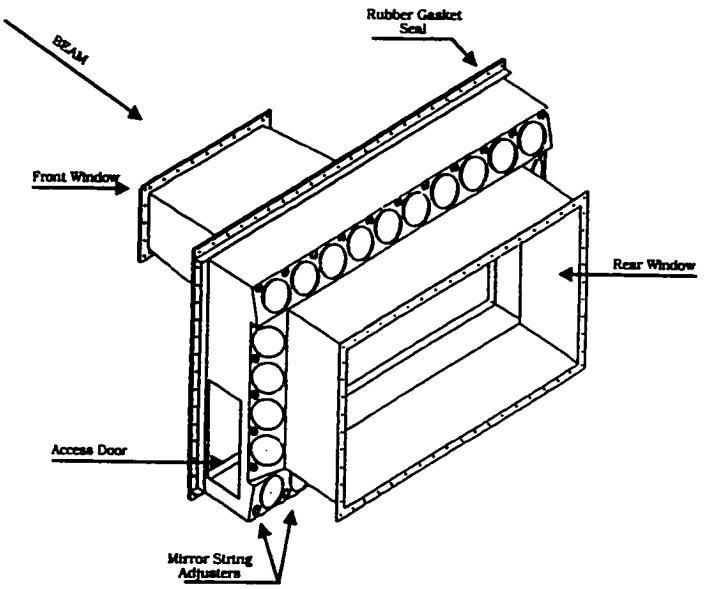

Figure 2.5: Schematic of the first Čerenkov detector, C1.

Čerenkov Detector Characteristics		
Parameter	C1	C2
Medium	100% N_2	80% He, 20% N_2
$(n-1)$	290×10^{-6}	86×10^{-6}
p_{th} for π (GeV/c)	5.7	10.5
p_{th} for K (GeV/c)	20.2	38.5
p_{th} for p (GeV/c)	38.5	70.6
Number of Mirrors	28	32

Table 2.3: Some important characteristics of the two Čerenkov detectors C1 and C2. The threshold momentum for each Čerenkov detector indicates the point at which a given particle starts to emit Čerenkov radiation.

Reproduced with permission of the copyright owner. Further reproduction prohibited without permission.

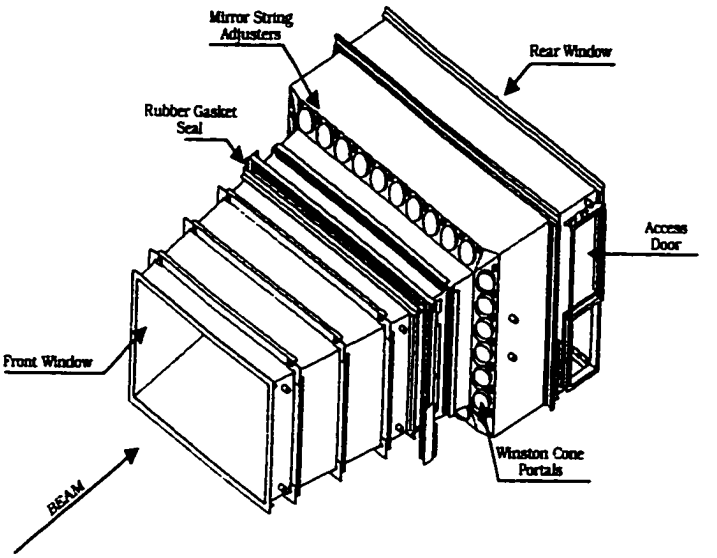

Figure 2.6: Schematic of the second Čerenkov detector, C2.

Čerenkov Separation for π, K and p	
Momentum Range (GeV/c)	Separation Achieved
0 - 5.7	No Separation
5.7 - 10.5	π / K p
10.5 - 20.2	π / K p
20.2 - 37.1	π / K / p
38.5 - 70.6	π K / p
70.6 - 200.0	No Separation

Table 2.4: The Čerenkov separation for π, K, and p achieved in different momentum ranges.

Reproduced with permission of the copyright owner. Further reproduction prohibited without permission.

C1 MIRROR ARRAY

<table>
<tr><td colspan="2">13</td><td colspan="2">9</td><td colspan="3">2</td><td colspan="2">10</td><td>14</td></tr>
<tr><td colspan="2">11</td><td>7</td><td>5</td><td>3</td><td>1</td><td>4</td><td>6</td><td>8</td><td>12</td></tr>
<tr><td colspan="2">25</td><td>21</td><td>19</td><td>17</td><td>15</td><td>18</td><td>20</td><td>22</td><td>26</td></tr>
<tr><td colspan="2">27</td><td colspan="2">23</td><td colspan="3">16</td><td colspan="2">24</td><td>28</td></tr>
</table>

C2 MIRROR ARRAY

<table>
<tr><td colspan="2">15</td><td colspan="2">11</td><td colspan="3">2</td><td colspan="2">12</td><td>16</td></tr>
<tr><td colspan="2">13</td><td>9</td><td>7</td><td>5</td><td>3</td><td>1</td><td>4</td><td>6</td><td>8</td><td>10</td><td>14</td></tr>
<tr><td colspan="2">29</td><td>25</td><td>23</td><td>21</td><td>19</td><td>17</td><td>20</td><td>22</td><td>24</td><td>26</td><td>30</td></tr>
<tr><td colspan="2">31</td><td colspan="2">27</td><td colspan="3">18</td><td colspan="2">28</td><td>32</td></tr>
</table>

Figure 2.7: Schematic of the mirror segmentation in C1 and C2 Čerenkov detectors.

Reproduced with permission of the copyright owner. Further reproduction prohibited without permission.

2.4.2 Segmented Liquid Ionization Calorimeter (SLIC)

A segmented liquid ionization calorimeter (SLIC) was designed for identifying those particles that interact mainly electromagnetically with matter. The E791 SLIC was used for electron and photon identification. High energy electrons passing through dense materials (such as lead) lose energy mainly because of bremsstrahlung radiation. The energy loss caused by electromagnetic radiation is proportional to $1/m^2$ of the incident particle. Therefore, this mechanism of energy loss is dominant only for electrons. The thickness of the SLIC is equivalent to about 20 radiation lengths for electrons and photons, and to only about 1.5 interaction lengths for hadrons. The absorbtion of muons in the SLIC was negligible. So, energy deposition in the SLIC is dominated by electrons and photons. A schematic view of the SLIC is shown in Fig. 2.8.

The SLIC consists of 60 layers of lead and liquid scintillator. The bremsstrahlung radiation develops in the lead layers and then e^+e^- pairs are created. The light is generated in the liquid scintillator layers by the e^+e^- pairs. Each liquid scintillator layer was optically separated into parallel strips by teflon-coated corrugated aluminium sheets which provided channels with total reflection surfaces. The design of the liquid scintillation layers is appropriate for both creating and guiding the scintillation light along certain directions. The scintillation light was mostly in the ultraviolet region and it was converted to the visible range by wavelength-shifter bars in order to improve the efficiency of the photomultiplier tubes.

The overall spatial resolution for locating the electron shower centroid was about 7 mm. The energy deposited by a charged particle or a photon is proportional to the photomultiplier tubes' output, after correction for the attenuation in the scintillator and wavelength-shifter bars. Precise location of the shower position (centroid) allowed the identification of the track consistent with the centroid position. The comparison between the energy (E) of the track determined by the SLIC and the track momentum (p) gave information on whether the track was an electron (for electrons E must be consistent with p within spectrometer resolution). The most important characteristics of the SLIC are

Reproduced with permission of the copyright owner. Further reproduction prohibited without permission.

summarized in Table 2.5.

SLIC Characteristics	
Parameter	Value
Z position (cm)	1866 to 1962
Number of Channels	334
Usable Area (cm×cm)	490 × 240
Radiation Length	20
Absorption Length	1.5
Energy Resolution $\left(\frac{\Delta E}{E}\right)^2$	$(11.5\%)^2 + \left(\frac{17.4\%}{E}\right)^2$
Position Resolution (cm)	0.7

Table 2.5: Important Characteristics of the SLIC.

2.4.3 Muon Identification

Electrons, photons and hadrons are almost completely absorbed in the electromagnetic calorimeter (SLIC), hadron calorimeter and additional steel shielding (106 cm thick), while muons leave only a small fraction of their energy in the calorimeters and steel shielding. Therefore most of the particles that survive behind the steel shielding are muons.

E791 used two planes of scintillation counters (called X and Y muon walls), to identify muons. Only muons with momentum above 4 GeV/c passed through material equivalent to 239 cm of iron in order to reach the muon walls.

The X wall consisted of 15 plastic scintillation counters (paddles), aligned vertically, in order to measure the x-position of the charged particles passing through it. Four additional paddles were mounted behind the central X paddle. These four additional paddles were used in coincidence with the X wall to reduce noise in the central region of the beam line. The second plane of scintillation counters (the Y wall), located 176 cm downstream from

Reproduced with permission of the copyright owner. Further reproduction prohibited without permission.

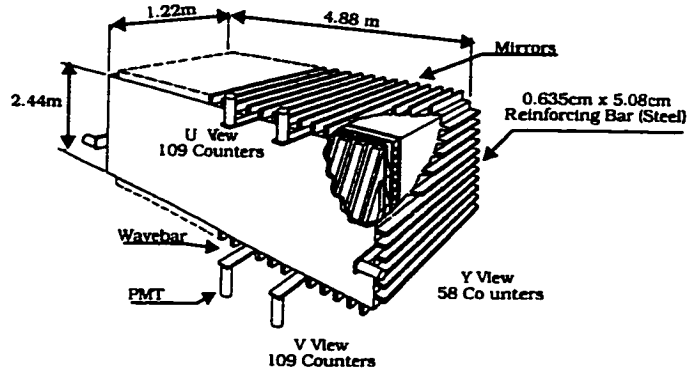

Figure 2.8: Schematic view of the SLIC.

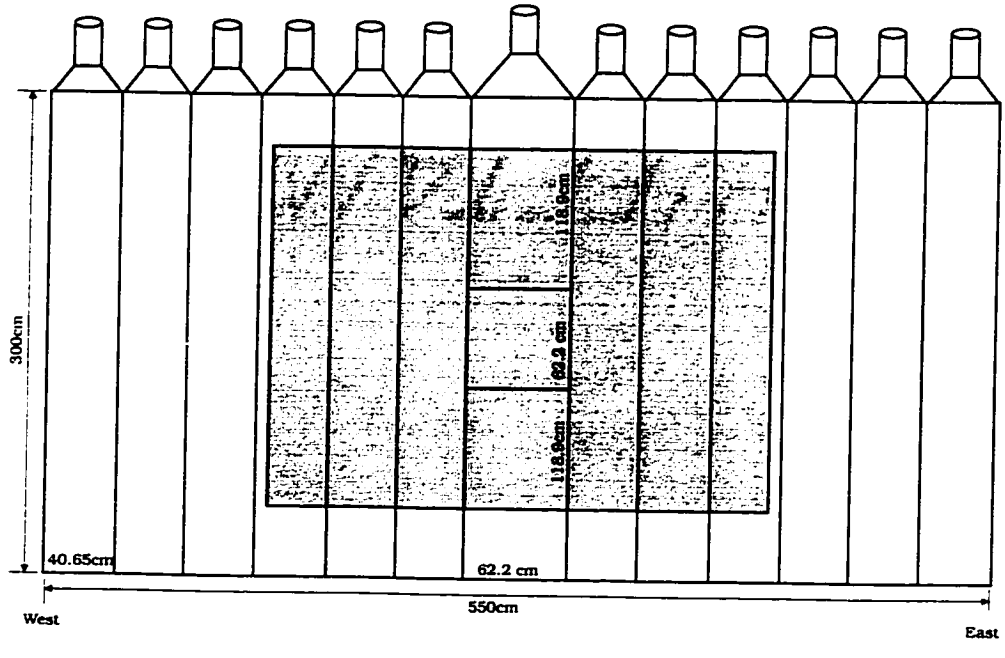

Figure 2.9: The geometry of the X muon wall. The shaded region shows the area of the X wall that overlaps with the Y wall.

Reproduced with permission of the copyright owner. Further reproduction prohibited without permission.

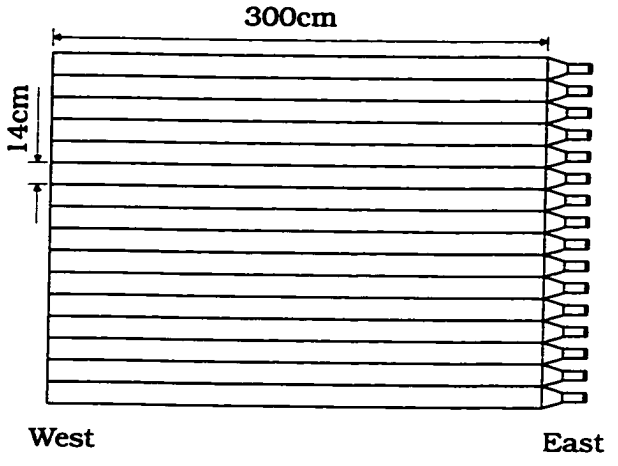

Figure 2.10: Geometry of the Y muon wall.

the X wall, had 16 paddles oriented horizontally to measure the y-position of the charged particles passing through them. The geometries of the two walls are shown in Fig. 2.9 and Fig. 2.10. The most important characteristics of the two muon walls are listed in Table 2.6.

Muon Wall Characteristics		
Parameter	X Wall	Y Wall
z-position (cm)	2243	2319
Area (cm^2)	550×300	300×224
Number of paddles	15	16
Efficiency (%)	69 ± 3	99 ± 1

Table 2.6: Characteristics of the X and Y muon walls.

The light created in a scintillation paddle by a charged particle passing through it was collected by the photomultiplier tube attached to the paddle. The electrical signal generated by the photomultiplier tube was sent to discriminators and also to time-to-

Reproduced with permission of the copyright owner. Further reproduction prohibited without permission.

digital converters (TDC's). TDC information from Y wall provided information about the x-position at Y wall with about 50 cm resolution, while the resolution of y-position is determined by the paddle width (14.2 cm). TDC information from X wall was not reliable and was not used in this analysis. Efficiency for X and Y walls were $(69 \pm 3)\%$ and $(99 \pm 1)\%$, respectively [21, 24].

2.5 Trigger

E791 used loose trigger requirements, hence recorded events at a high rate with little bias from the trigger itself. During the six months of run period, about 50 Terabytes of raw data were recorded on 24,000 8mm video tapes. An event was saved if it passed the following conditions:

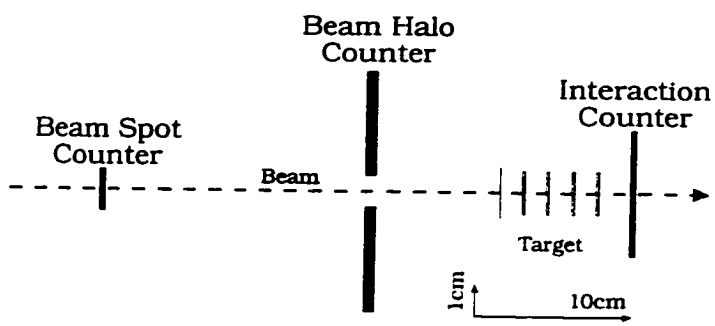

Figure 2.11: Schematic of scintillating paddles used in trigger decision.

- Only one beam particle was detected upstream of the targets. The number of beam particles was determined with a scintillation paddle (beam spot counter) placed in the beam path, as shown in Fig. 2.11.
- No signal was recorded by the beam halo counter. The beam halo counter was a scintillation paddle with a 1 cm diameter hole at its center (Fig. 2.11). This

Reproduced with permission of the copyright owner. Further reproduction prohibited without permission.

requirement ensures that beam pions are not too far from the beam axis, and that additional halo tracks were not present.

- At least four charged particles were detected by the interaction counter located downstream the targets (Fig. 2.11).
- $E_T > 4$ GeV/c, where E_T is the energy deposited in the SLIC and hadrometer transverse to the beam direction.
- $E_T < 700$ GeV/c, in order to reject events with multiple beam particles.

Beam pions interacted with the targets at 40 kHz. About half of these interactions passed the trigger requirements.

Reproduced with permission of the copyright owner. Further reproduction prohibited without permission.

Chapter 3

Data Selection

The decay channel studied was the sequential decay $D^+ \to \overline{K}^{*0}\mu^+\nu_\mu$ followed by $\overline{K}^{*0} \to K^-\pi^+$ (charge conjugate decays are implied). Due to the loose trigger, most events do not contain a charm decay. Out of 20 billion raw data events, only about 200,000 charm decays were reconstructed. To eliminate the huge background, tight cuts were applied to tracks, vertices and particle identification. The final data sample contained about 3000 decays after subtracting 600 background events.

Events were selected if they contained a decay vertex determined by the best estimate of the intersection point of three tracks that have been identified as a muon, a kaon and a pion. The longitudinal separation between this candidate decay vertex and the production point was required to be at least 15 times the estimated error on the separation. The two hadrons were required to have opposite charge. If the kaon and the muon had opposite charge, the event was assigned to the "right-sign" sample; if they had the same charge, the event was assigned to the "wrong-sign" sample used to model the background. Since the lepton charge was always the same as the decay vertex charge, the background was modeled by the wrong-sign sample with no extra weight. The event selection criteria used for this analysis were the same as for the electronic-mode form factor analysis [4], except for those related to lepton identification.

Reproduced with permission of the copyright owner. Further reproduction prohibited without permission.

The most important sources of background were:

- Random tracks identified as a kaon, a pion, and a muon which by chance originated from the same vertex.
- Other charm decays.

The wrong-sign sample correctly accounts for background due to the random tracks and for some of the other charm decays (like $D_s^+ \to K^- K^+ \mu^+ \nu_\mu$). There are still charm decays (like $D^+ \to K^- \pi^+ \pi^+ \pi^0$ with a charged pion misidentified as a muon) that contribute only to the right-sign sample. This kind of background, as well as background associated with random tracks, was substantially reduced mainly by the cut applied to vertex separation (SDZ), and by the minimum kinematically allowed mass of the $D^\pm$.

3.1 Strip, Substrip and Microstrip

This analysis is based on 100% of the E791 data sample. The events passed the standard E791 filter and strip stages; these cuts are described in Ref. [20]. In the next two stages the events passed the KSU semileptonic substrip and microstrip cuts. The selection criteria for the combination of filter, strip substrip and microstrip are:

- The muon candidate has a momentum larger than 7 GeV.
- The muon candidate hits either X or Y wall within 3 σ from the projected paddle. The value of σ is determined by the expected Coulomb multiple scattering of the muon candidate.
- The primary vertex lies upstream of the interaction counter: $z_{prim} < -1.0$ cm.
- The vector sum of momentum components perpendicular to D^+ direction of flight of the three tracks is less than 1.5 GeV/c.

Reproduced with permission of the copyright owner. Further reproduction prohibited without permission.

- The probability for the tracks in the secondary vertex to have come from the primary is low (IPMIN > 6).

3.2 Nanostrip

The nanostrip level produces an event reduction of about 5 to 1. At this level the cut most effective for reducing the background was the one applied to the longitudinal separation between production and decay vertices divided to its estimated error (SDZ variable). The criterion used for cut optimization was to maximize the significance of the signal $S/\sqrt{B}$, where S is the signal and B is the background. The values of S and B were extracted from right-sign (RS) and wrong-sign (WS) samples. By definition: $S = RS - WS$ and $B = WS$. The values of $S/\sqrt{B}$ were plotted in Fig. 3.1 for different cuts applied on SDZ. All cuts implemented at nanostrip level were:

1. Secondary Vertex Cuts
   - Well-separated (SDZ > 15) secondary vertex contained 3 tracks, and had charge ± 1.
   - Vertex χ^2/dof was less than 9.0.
   - Vertex was outside of a target foil by at least one standard deviation.
2. Track Quality Cuts
   - Each track was detected in all three regions of the spectrometer (upstream of the first magnet, between the two magnets, and downstream of the second magnet).
   - Track χ^2/dof was less than 5.0.
3. Particle Identification Cuts
   - One track had kaon probability, as determined from Cerenkov information, greater than 0.13.

Reproduced with permission of the copyright owner. Further reproduction prohibited without permission.

4. Mass Cuts

- Invariant mass $M_{K\pi}$ of the K^{*0} candidate, was between 0.64 and 1.30 GeV.
- The minimum kinematically allowed mass of the $D^{\pm}$ candidate was between 1.1 and 2.3 GeV. It was defined as:

$$M_{min} = p_t + \sqrt{m_{vis}^2 + p_t^2} \tag{3.1}$$

where m_{vis} and p_t refer to the invariant mass and the sum of the transverse momenta, respectively, of the three visible particles.

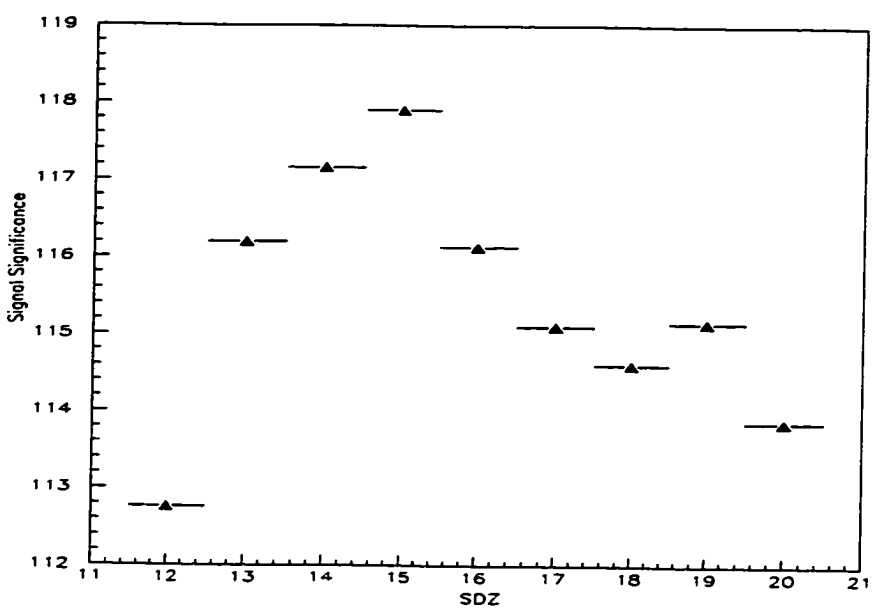

Figure 3.1: Significance of the signal when SDZ cut changes from $SDZ > 12$ to $SDZ > 20$. The optimized cut is $SDZ > 15$.

The $D^{\pm}$ candidate mass cannot be fully reconstructed due to the undetected neutrino. At best, the neutrino momentum (and the D mass) can be reconstructed up to a quadratic ambiguity (Appendix A).

Reproduced with permission of the copyright owner. Further reproduction prohibited without permission.

3.3 Analysis Cuts

After the last set of cuts (nanostrip) the data sample had a manageable size (two tapes). To further improve the quality of the signal tighter cuts were needed. The final set of cuts produced a clean $D^+ \longrightarrow \bar{K}^{*0}\mu^+\nu_\mu$ sample ($S/\sqrt{B} > 124$). At this stage tighter cuts were applied to muon and hadron identification, to secondary vertex position, and to $M_{K\pi}$ and M_{min} mass ranges. The final muon identification was based on tighter requirements imposed on the information provided by the Y muon wall. The information provided by Y wall was more reliable, and therefore it was mostly used for muon identification. More details about muon identification are given in Appendix B.

1. Muon identification:
   - $p_\mu > 8$ GeV.
   - Identification on Y direction: the projected y position of the muon candidate track at Y wall was within 1 σ from the hit paddle ($n_{\sigma_y} < 1.0$).
   - Identification on X direction: the projected x position of the muon candidate track at Y wall was consistent with the TDC information ($abs(dist) < 8.0$ [1]).
2. Kaon probability as determined by Cerenkov counters : $K_{Prob} > 0.4$.
3. Pion probability of the pion candidate: $\pi_{Prob} > 0.4$.
4. $0.85 < M_{K\pi} < 0.94$ GeV.
5. $1.6 < M_{min} < 2.0$ GeV.
6. $z_{secondary} < -0.4$ cm.
7. The invariant mass of the three visible particles with the muon treated as pion, was outside the region $(1.82; 1.92)$ GeV.

[1] The definitions of n_{σ_y} and *dist* variables are given in Appendix B.

Reproduced with permission of the copyright owner. Further reproduction prohibited without permission.

The last cut removed the feedthrough from the hadronic decay due to particle misidentification $D \to K\pi\pi$.

In addition to these cuts, there was also a cut established with the Binary Tree Algorithm commercial software CART [26]. The CART cut is a linear combination of four variables that have high discrimination power against the background. The four variables used by CART are:

1. Sigma - Number of standard deviations the secondary vertex was outside the target foil or interaction counter.
2. SDIP - The distance-of-closest-approach in the x-y plane of the reconstructed D^+ candidate (allowing for the missing neutrino information) with respect to the primary vertex, measured in standard deviations.
3. SDZ - The separation of primary and secondary vertices measured in standard deviations.
4. Sratio - The product of ratios of SSISO/SPISO for each of the three tracks. SSISO (SPISO) was the distance of closest approach of a track to the secondary (primary) vertex measured in standard deviations.

The coefficients of the linear combination are summarized in the Table 3.1. Without the CART cut, and with all the other cuts applied, the data sample contained 4245 right-sign and 967 wrong-sign events, compared with 3629 right-sign and 595 wrong-sign when the CART cut was also applied. The CART cut had little effect on improving the significance of the signal but it had a big effect on increasing the signal to background ratio (from 3.39 to 5.10). In conclusion, the CART cut increased the nominal sensitivity by a small amount, and reduced the systematic uncertainties associated with the background substantially. The effects of CART and M_{min} cuts on background reduction can be seen in Fig. 3.2. All cuts applied, except those related to muon ID, were the same as those used for the electron mode $D^+ \to \overline{K}^{*0} e^+ \nu_e$.

Reproduced with permission of the copyright owner. Further reproduction prohibited without permission.

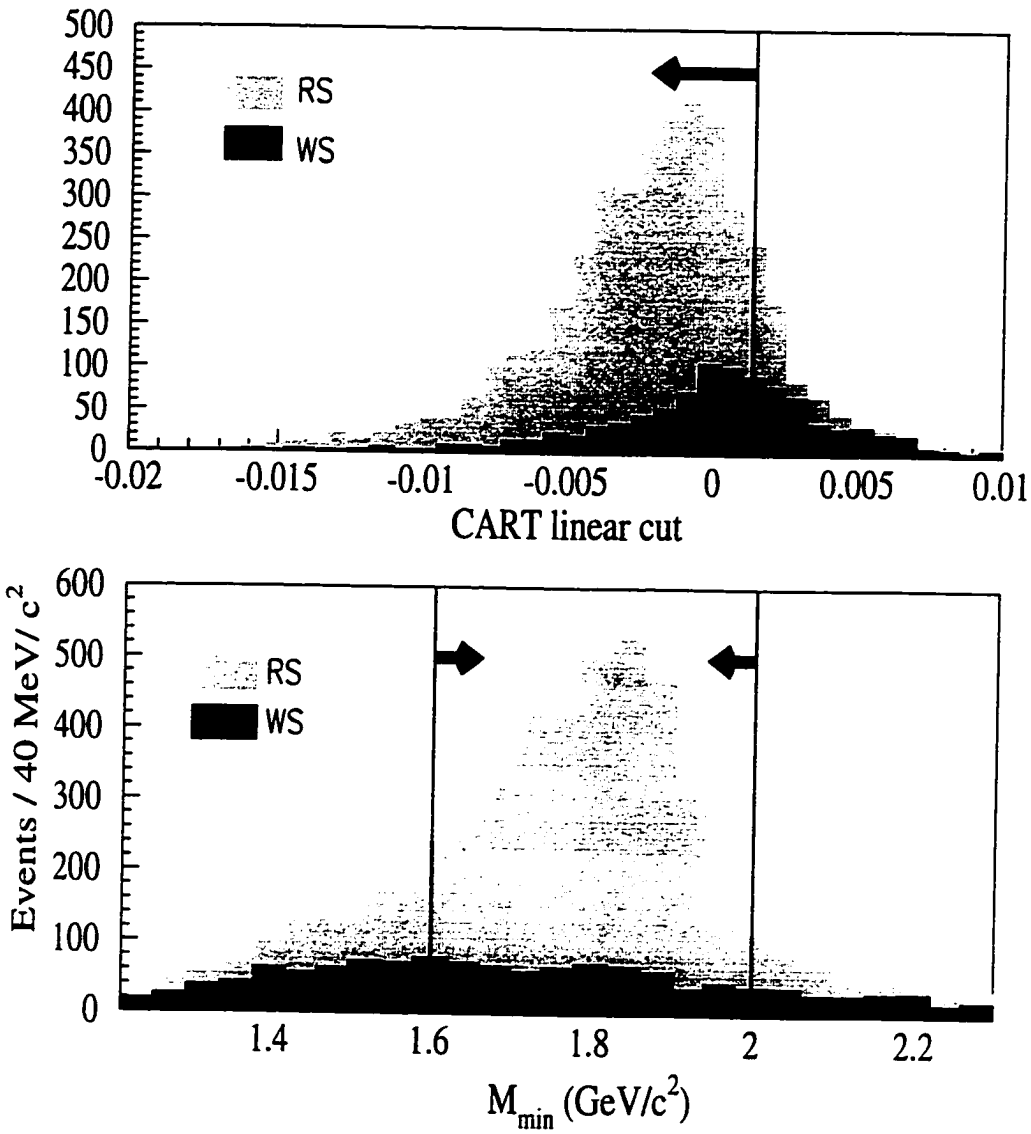

Figure 3.2: Right-sign (clear histograms) and wrong-sign (shaded) distributions of the linear combination chosen by CART (top) and minimum parent mass (bottom). Events lying to the left of the vertical line (top plot) and between the two vertical lines (bottom plot) are kept, and the rest are discarded.

Reproduced with permission of the copyright owner. Further reproduction prohibited without permission.

Table 3.1: Summary of the cuts chosen by CART to produce the clean $D^+ \to \bar{K}^{*0}\mu^+\nu_\mu$ sample. Each column gives the coefficients of the six parameters plus a constant which represents the cut $C_1 * Sigma + C_2 * SDIP + C_3 * SDZ + C_4 * Sratio + Constant > 0$.

Parameter	CART Cut Coefficients
Sigma	2.79×10^{-4}
SDIP	-2.39×10^{-4}
SDZ	2.39×10^{-5}
Sratio	-1.00
Constant	-1.37×10^{-3}

3.4 $D^+ \to \overline{K}^{*0}\mu^+\nu_\mu$ Signal

After all cuts there were 3629 right-sign and 595 wrong-sign events in the final data sample. The top left plot in Fig. 3.3 shows the M_{min} distribution for both the right- sign and wrong-sign events, following all cuts except the M_{min} cut. The $M_{K\pi}$ distribution is shown in the top right plot in Fig. 3.3 for those events lying in the $1.6 < M_{min} < 2.0$ GeV window. The bottom plot shows the distribution of the $K\pi$ invariant mass for the background subtracted data ("right-sign" minus "wrong-sign") fitted to a Breit-Wigner function. The mean (M_{K^*}) and width (Γ_0) values of the Breit-Wigner distribution are in fairly good agreement with the PDG values ($m_{K^*} = 895.40 \pm 0.7$ MeV and $\Gamma = 54.2 \pm 2.0$ MeV compared to $m_{K^*} = 896.10 \pm 0.28$ MeV and $\Gamma = 50.5 \pm 0.6$ MeV).

The distributions of kinematic variables are shown in Fig. 3.4. Kinematic variables can be calculated using either the negative solution of the neutrino momentum or the positive one. The set of cuts used to obtain this data sample will be referred to *standard cuts*.

Reproduced with permission of the copyright owner. Further reproduction prohibited without permission.

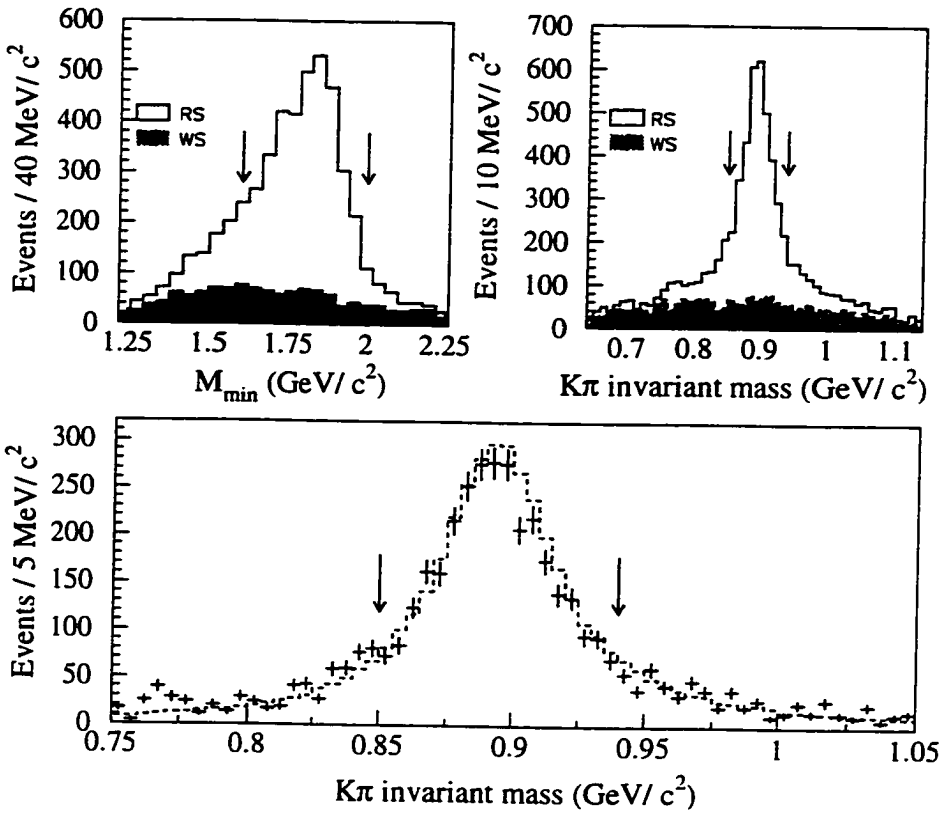

Figure 3.3: Distributions of minimum parent mass M_{min} and $K\pi$ invariant mass for $D^+ \rightarrow \overline{K}^{*0}\mu^+\nu_\mu$ candidate events. Right-sign (RS) and wrong-sign (WS) samples are defined in the text. Top left: M_{min} for events with $K\pi$ mass in the range 0.85 to 0.94 GeV/c^2. Top right: $K\pi$ invariant mass for events with M_{min} in the range 1.6 to 2.0 GeV/c^2. Bottom: background-subtracted (RS-WS) $K\pi$ mass distribution (crosses) compared to Monte Carlo prediction (dashed histogram) for events with M_{min} in the range 1.6 to 2.0 GeV/c^2. All candidates pass all the other final selection cuts. The arrows indicate the range of the final sample.

Reproduced with permission of the copyright owner. Further reproduction prohibited without permission.

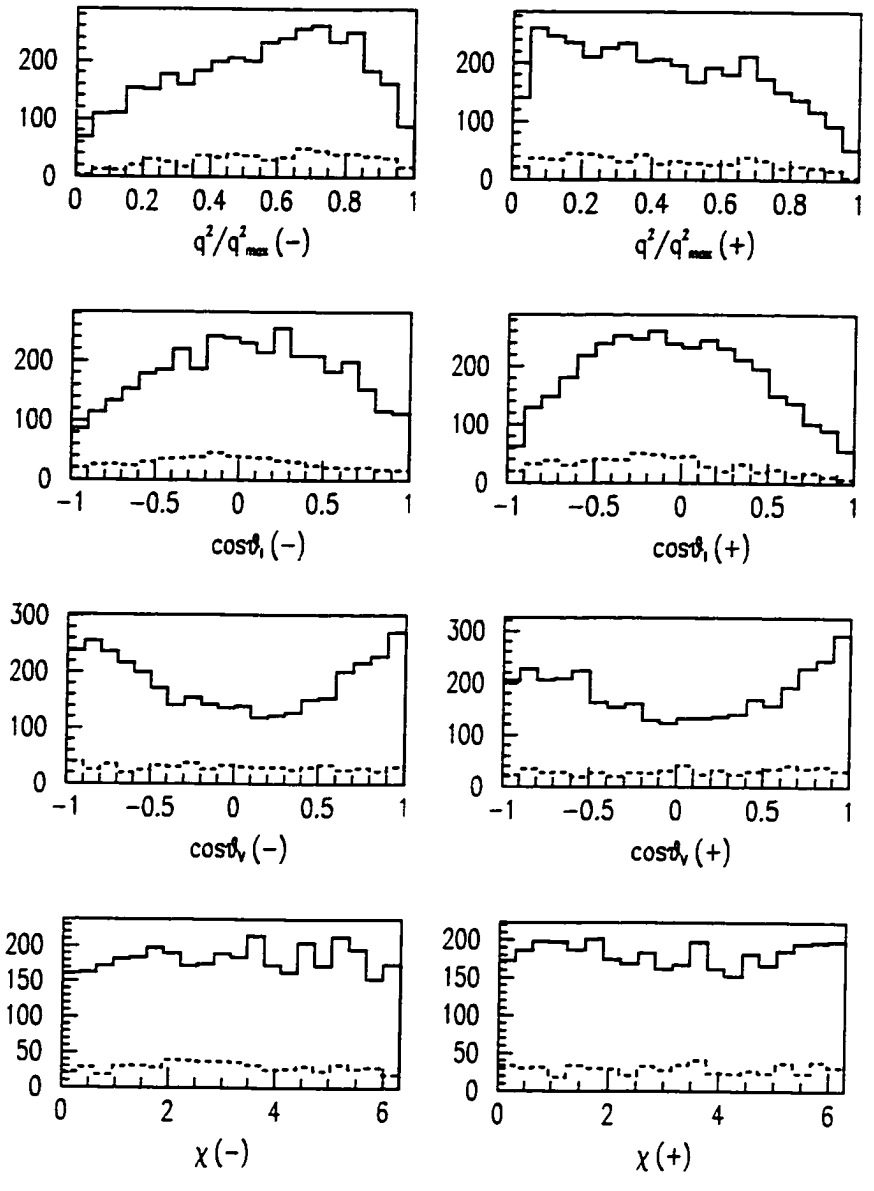

Figure 3.4: Distributions of the four kinematic variables for RS data events calculated using the negative solution of neutrino momentum (left) and the positive solution (right). The distributions of WS events are drawn with dash lines.

Reproduced with permission of the copyright owner. Further reproduction prohibited without permission.

3.5 Summary of the Cuts

The final values of all cuts are summarized below:

1. The vector sum of the momenta of the three tracks in the secondary vertex, perpendicular to the flight direction of the D^+ (Pt balance) was less than 1.5 GeV.

2. Low probability for the tracks in the secondary vertex to have come from the primary vertex (χ^2 of impact parameter > 6).

3. The primary vertex was upstream of the interaction counter ($Z_{prim} < -1.0$ cm).

4. Secondary Vertex Cuts

   - Well separated (SDZ $>$ 15) secondary vertex, contained 3 tracks, and had charge ± 1.
   - Vertex χ^2/dof was less than 9.0.
   - Vertex was outside a target foil by at least one standard deviation.
   - Vertex was upstream of the interaction counter ($Z_{sec} < -0.4$ cm).

5. Track Quality Cuts

   - Each track was detected in all three regions of the spectrometer.
   - Track χ^2/dof was less than 5.0.

6. Particle Identification Cuts

   - $p_\mu > 8$ GeV.
   - $n_{\sigma_y} < 1.0$ (n_{σ_y} is defined in Appendix B).
   - $abs(dist) < 8.0$ ($dist$ is defined in Appendix B).
   - The charge of the track identified as muon was the same as the charge of the secondary vertex.

Reproduced with permission of the copyright owner. Further reproduction prohibited without permission.

- The kaon candidate had a kaon probability, as determined from Cerenkov information, greater than 0.4.
- The pion candidate had a pion probability, as determined from Cerenkov information, greater than 0.4.

7. Mass Cuts

- The invariant mass of the K^{*0} candidate was between 0.85 and 0.94 GeV.
- The minimum parent mass (M_{min}) was between 1.6 and 2.0 GeV.
- The invariant mass of $K\pi\pi$ (the muon candidate interpreted as a pion) was not between 1.82 and 1.92 GeV.

In addition to these cuts there was also a CART cut:

$$-2.79 \cdot 10^{-4} \cdot sigma + 2.39 \cdot 10^{-4} \cdot sdip - 2.39 \cdot 10^{-5} \cdot SDZ + sratio < 0.137 \cdot 10^{-2}.$$

Reproduced with permission of the copyright owner. Further reproduction prohibited without permission.

Chapter 4

Fitting Technique

In principle, the form factor ratios can be extracted by fitting the distribution of data points in the four-dimensional kinematic variable space to the full expression for the differential decay rate (Eqn. 1.22). In practice this easy procedure cannot succeed because of "real world effects" like:

- Smearing of position in four-dimensional space.
    1. Spectrometer resolution.
    2. Neutrino momentum ambiguity.
- Non-uniform acceptance.
- Background.

A solution to these problems is to use the unbinned maximum likelihood method developed by the E691 Collaboration [25]. This method was our primary fitting technique, and it has been used in the past in similar analysis by other groups [5, 7, 8]. In this method all data and Monte Carlo decays were reconstructed using the lower laboratory-frame neutrino momentum solution.

Reproduced with permission of the copyright owner. Further reproduction prohibited without permission.

To check for any potential bias in the fit results due to this choice for the neutrino momentum, a second fitting technique was developed by the author. This secondary fitting technique, referred as the matrix method, is a binned maximum likelihood method that includes in the fit decays reconstructed with both neutrino momentum solutions. The systematic uncertainties are larger when the fits are performed with the second fitting technique (Chapter 5), and this is the reason for choosing the results obtained with the unbinned maximum likelihood method as our primary results. However, the matrix method was not plagued by systematic shifts of the fit results (Appendix C) and it also took into account both neutrino momentum solutions.

The general strategy of both fitting techniques was to compare data with Monte Carlo simulated events. The large Monte Carlo sample includes all detector effects (smearing and acceptance). In both fitting techniques background was simulated by the wrong-sign sample.

4.1 Monte Carlo Sample

Approximately 25 million Monte Carlo events with at least one $D^+ \to \bar{K}^{*0}\mu^+\nu_\mu$ (or charge conjugate) in the event, were generated on the Kansas State University computer farm for this analysis. The GEANT-based Monte Carlo simulation includes a physiscs generator which simulates the D meson decays acording to the full expression of the differential decay rate (Eqn. 1.22). The values of the form factor ratios used to generate Monte Carlo events were: $R_2 = 0.82$, $R_V = 2.00$ and $R_3 = 0.00$. The Monte Carlo events were passed through the same analysis cuts as data. The numbers of Monte Carlo events that passed different stages of the analysis are summarized in the Table 4.1.

The distributions of kinematic variables (at reconstruction level) are plotted in Fig. 4.1. A comparison between background subtracted data and Monte Carlo is shown in Fig. 4.2 for $M_{K\pi}$ and M_{min} distributions.

Reproduced with permission of the copyright owner. Further reproduction prohibited without permission.

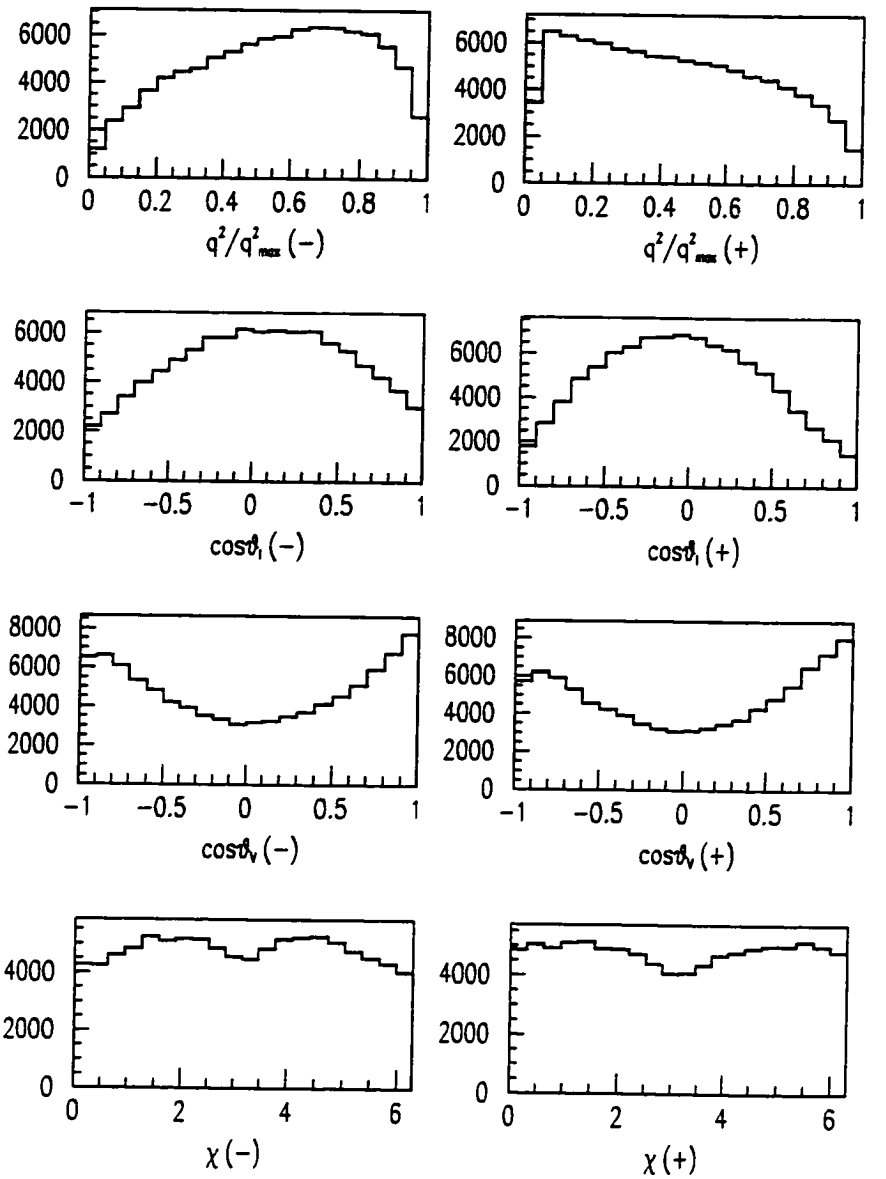

Figure 4.1: Distributions of the four kinematical variables for Monte Carlo events calculated using the negative solution of neutrino momentum (left) and the positive solution (right).The plots were done using the whole MC sample (95,579 events).

Reproduced with permission of the copyright owner. Further reproduction prohibited without permission.

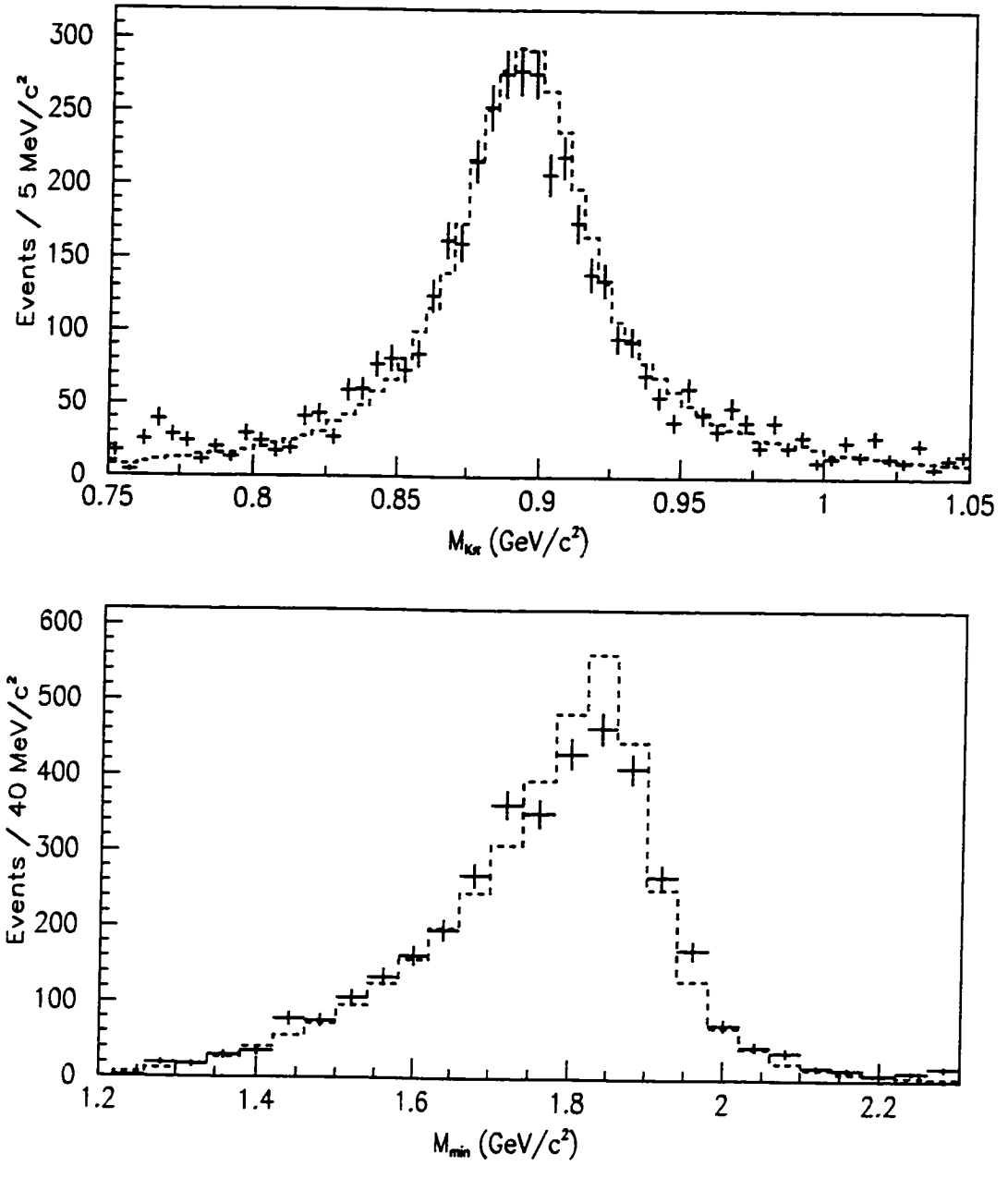

Figure 4.2: The distributions of $M_{K\pi}$ (top) and M_{min} (bottom) in background subtracted data (cross hatches) overlaid with Monte Carlo (dashed line).

Reproduced with permission of the copyright owner. Further reproduction prohibited without permission.

Table 4.1: Monte Carlo events passing each set of cuts.

	No. of events	% passing
Generated	25,000,000	100
Filter	11,734,215	46.94
Strip, substrip, microstrip	1,356,792	5.43
Nanostrip	532,599	2.14
Analysis cuts	95,579	0.38

4.2 Kinematic Variable Resolutions

Semileptonic decays cannot be fully reconstructed due to the undetected neutrino. With the available information about the D^+ direction of flight and the charged daughter particle momenta, the neutrino momentum (and also the kinematic variables q^2, $\cos\theta_l$, $\cos\theta_V$, and χ) can be determined up to a two-fold ambiguity. Among the four kinematic variables, q^2/q^2_{max} changes most when the decay is reconstructed with the wrong neutrino momentum solution (Fig. 3.4 and Fig. 4.1).

The resolutions of the kinematic variables can be determined from the Monte Carlo simulation for both neutrino momentum solutions. Table 4.2 compares the RMS values for $X_{reconstructed} - X_{true}$ where X stands for each of the four kinematic variables when the decays were reconstructed with either lower or higher neutrino momentum solutions.

The resolutions of kinematic variables seem not to depend on the choice of neutrino momentum solution. However, reconstructing decays with the lower neutrino momentum solution depletes the region of low q^2 (Fig. 4.1). This observation suggests that the smearing of the kinematic variables might have a different effect on the observed differential decay rate. To test this assumption, the differential decay rate is evaluated for each Monte Carlo event using the kinematic variables reconstructed with the lower neutrino mo-

Reproduced with permission of the copyright owner. Further reproduction prohibited without permission.

Table 4.2: Resolutions of the kinamatic variables reconstructed with the lower and higher neutrino momentum solutions.

	RMS (low)	RMS (high)
$(q^2/q^2_{max})_{rec.} - (q^2/q^2_{max})_{true}$	0.139	0.146
$(\cos\theta_l)_{rec.} - (\cos\theta_l)_{true}$	0.142	0.140
$(\cos\theta_V)_{rec.} - (\cos\theta_V)_{true}$	0.150	0.148
$(\chi)_{rec.} - (\chi)_{true}$	0.605	0.600

mentum (Γ_-), the kinematic variables reconstructed with the higher neutrino momentum solution (Γ_+) and the kinematic variables reconstructed with the correct solution of the neutrino momentum (Γ_{true}). The distributions of the fractional errors $(\Gamma_- - \Gamma_{true})/\Gamma_{true}$ and $(\Gamma_+ - \Gamma_{true})/\Gamma_{true}$ are shown in Fig. 4.3. The RMS's of these two distributions (0.470 and 0.574) show that the differential decay rate is better approximated by the decays reconstructed with the lower neutrino momentum. This fact can be explained by the better acceptance for the events containing high charged particle momenta and low neutrino momentum. This statement is also confirmed by the lower statistical errors when the fits were performed with decays reconstructed lower neutrino momentum (Chapter 5 Table 5.12).

4.3 Maximum Likelihood

Each data event is associated with a point in the four-dimensional phase space defined by the four kinematic variables q^2 , $\cos\theta_l$, $\cos\theta_V$ and χ. If smearing and acceptance effects are ignored, the probability distribution function of these points is related to the decay rate formula:

$$F(x;\mu) = \frac{\Gamma(x;\mu)}{\int dx\Gamma(x;\mu)} \tag{4.1}$$

where x is the position in four-dimensional phase-space, and μ is the set of the unknown form factor ratios R_2 , R_V and R_3.

Reproduced with permission of the copyright owner. Further reproduction prohibited without permission.

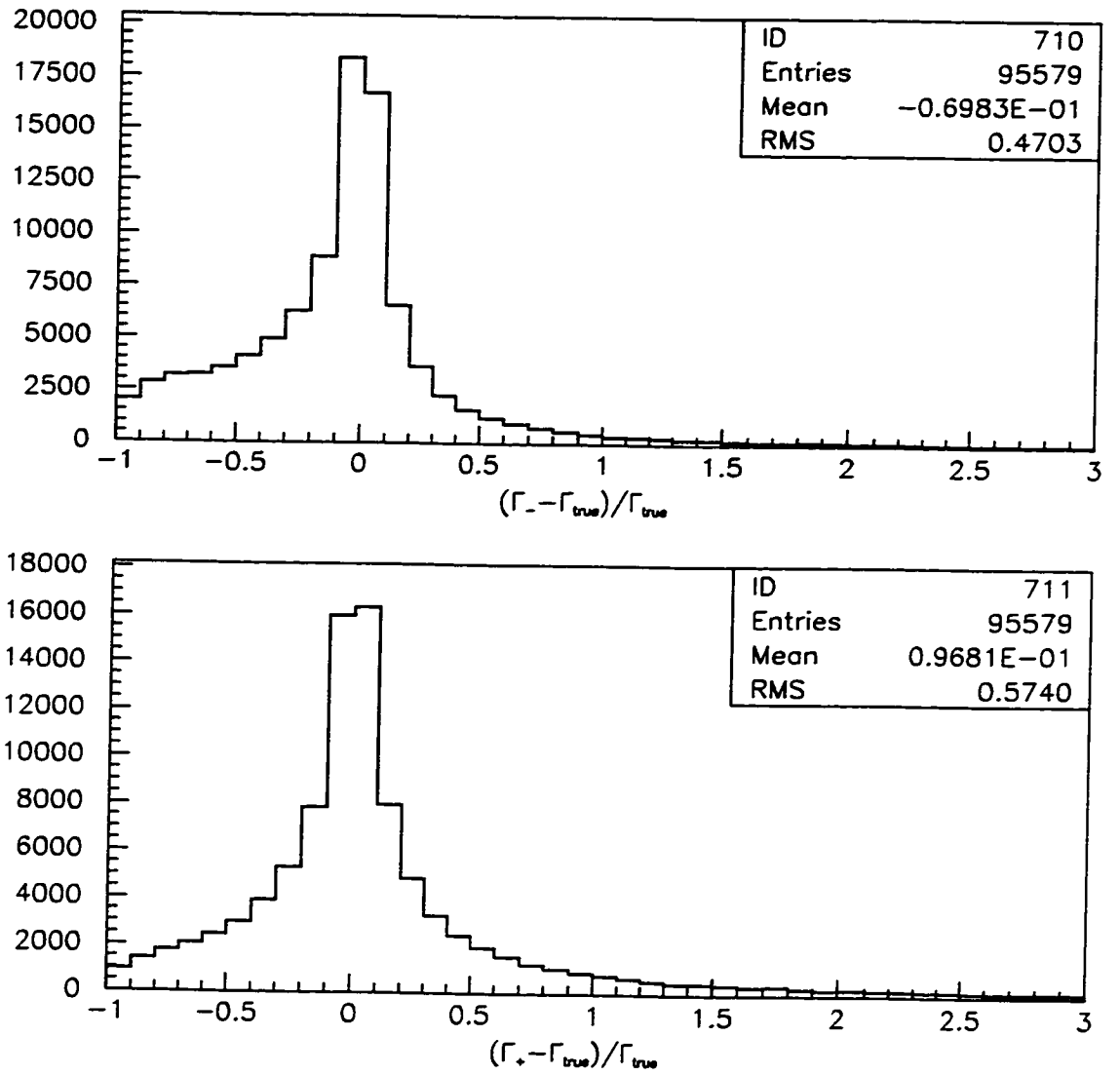

Figure 4.3: Resolution of the decay rate when Monte Carlo events were reconstructed using the lower neutrino momentum solution (top) and the higher neutrino momentum solution (bottom).

Reproduced with permission of the copyright owner. Further reproduction prohibited without permission.

For a given data sample consisting of n events, the best estimate of the parameters μ maximizes the likelihood function $\mathcal{L}$ defined by:

$$\mathcal{L} = \prod_{i=1}^{n} F(x_i; \mu) \tag{4.2}$$

As n goes to infinity μ is guaranteed to converge to the true value, provided the normalization condition for $F(x; \mu)$ is fulfilled.

4.4 Smearing and Acceptance Effects

4.4.1 Distorted Distribution Function

When generated, the events were distributed according to the differential decay rate $\Gamma(x, \mu)$ (Eqn. 1.22). At the reconstruction level, the events were distributed according to a distorted distribution function $F(\tilde{x}, \mu)$ because of smearing and acceptance effects. As in Ref. [25] the symbol $\tilde{x}$ is used for the reconstructed position in phase space and x for the generated position. In general F is related to Γ by:

$$F(\tilde{x}, \mu) \propto \int dx A(x) S(\tilde{x}, x) \Gamma(x; \mu) \tag{4.3}$$

$A(x) \longrightarrow$ acceptance function

$S(\tilde{x}, x) \longrightarrow$ smearing function

The effects of the unknown functions $A(x)$ and $S(\tilde{x}, x)$ are modeled by the Monte Carlo simulation. At the reconstruction level, the Monte Carlo events were distributed according to $F(\tilde{x}; \mu_0)$. The parameters μ_0, used to generate the Monte Carlo sample, were chosen to be $R_2 = 0.82$ and $R_V = 2.00$ and $R_3 = 0.00$ in agreement with the results from a previous experiment (E653 [7]).

Reproduced with permission of the copyright owner. Further reproduction prohibited without permission.

4.4.2 Sources of Smearing Effects

Smearing effects are a serious problem for this analysis because they have the tendency to flatten distribution functions. As a result, the final values of form factors might be systematically biased. There are two major sources of smearing effects:

1. Limited resolution of the spectrometer.

2. The twofold ambiguity of the neutrino momentum (Appendix A).

The magnitude of smearing effects can be estimated from Monte Carlo studies by comparing the generated to reconstructed values of the kinematic variables. For reasons described in Section 4.2 the decays were reconstructed using the lower neutrino momentum solutions. Roughly, about 50 % of events were reconstructed with the wrong solution of the neutrino momentum. The smearing due to this uncertainty is not negligible. Table 4.3 compares the smearing caused only by limited resolution of the spectrometer with total smearing.

Table 4.3: The widths of the differencies $x_{rec} - x_{gen}$ when both sources of smearing are present (RMS1) and when the decays are affected only by the detector smearing (RMS2).

	RMS1	RMS2
q^2/q^2_{max}	0.138	0.079
$\cos\theta_l$	0.141	0.098
$\cos\theta_V$	0.149	0.097
χ	0.603	0.361

If the smearing originating from the neutrino momentum ambiguity is excluded, the resolution of the position in the four-dimensional kinematic variable space increases by a factor 6.4; thus this ambiguity dominates the resolution of kinematic variables.

Reproduced with permission of the copyright owner. Further reproduction prohibited without permission.

4.5 Smearing and Acceptance Effects

To include smearing and acceptance effects, the Monte Carlo sample had to pass the same analysis procedure as real data. The distorted distribution function was approximated by the distribution function of reconstructed Monte Carlo events.

$$F_{MC}(x;\mu_0) = \frac{1}{N_{MC}} \sum_{i=1}^{N_{MC}} \delta^4(x - \tilde{x}_i) \tag{4.4}$$

where x is an arbitrary point in the four-dimensional kinematic variable space and the $\tilde{x}_i$'s are the positions of Monte Carlo reconstructed events. The distribution function is normalized and includes all smearing and acceptance, but without free parameters cannot be used to fit the data. The most convenient solution to this problem is to weight each Monte Carlo event with the ratio of decay weight $\Gamma(x;\mu)$ evaluated with a trial set of form factors μ, to decay weights $\Gamma(x;\mu_0)$ evaluated with the generated weights μ_0.

$$W(x;\mu,\mu_0) = \frac{\Gamma(x;\mu)}{\Gamma(x;\mu_0)} \tag{4.5}$$

The general expression for the distribution function becomes:

$$F_{MC}(x;\mu) = \frac{\sum_{i=1}^{N_{MC}} W(x_i;\mu,\mu_0)\delta^4(x - \tilde{x}_i)}{\sum_{j=1}^{N_{MC}} W(x_j;\mu,\mu_0)} \tag{4.6}$$

The weights are evaluated at the generated positions of Monte Carlo events, while the arguments of the delta functions contain the reconstructed positions ($\tilde{x}_i$'s).

4.6 Unbinned Maximum Likelihood Method

4.6.1 General Description

This fitting technique was developed by E691 Collaboration [8] for a similar analysis. In this method, the probability distribution function, evaluated at a data point, is approximated by the the average of the distribution function, Eqn 4.4, over a volume centered on the data point.

$$\bar{F}_{MC}(x_i;\mu) = \frac{1}{V}\int_V d^4x F_{MC}(x;\mu) \tag{4.7}$$

Reproduced with permission of the copyright owner. Further reproduction prohibited without permission.

Ideally, the volume V surrounding a data point should be small to minimize the difference between $\bar{F}_{MC}$ and F_{MC} and to maintain the normalization of $\bar{F}_{MC}$. On the other hand, the expression for F_{MC} was determined by the distribution of a finite number of Monte Carlo events, and therefore it is itself an approximation. This approximation works better if the volume V contains many Monte Carlo events, and this requirement implies that V should be large. The best compromise between the two conflicting conditions is achieved when the values of form factors are stable against the variation of volume V. The nominal volume was chosen at 1/625 from the total phase-space volume

$$V = \Delta q^2 \Delta \cos\theta_l \Delta \cos\theta_V \Delta\chi. \tag{4.8}$$

Each of the four projections of V is as large as one fifth of the phase-space available to the corresponding kinematic variable.

If a data point is close to the edge of phase-space, then the volume V is shrunk such that it is still centered on the data point. In those cases when the volume V does not contain a minimum number of Monte Carlo points (we require at least 4) the data points are rejected from the fit. This happens for about 3% of right-sign events.

The approximation implied by Eqn. 4.7 is the major source of systematic shifts of the fitted form factors. The values of the systematic shifts can be determined precisely from Monte Carlo studies. More details about the origin of the systematic shifts are given in Appendix C.

4.6.2 Including Background

The right-sign sample contained a mixture of true $D^+ \to K^-\pi^+\mu^+\nu_\mu$ events and background. The probability distribution function, Eqn. 4.7, is valid only for the true D decays. It was assumed that background is correctly modeled by the sample of wrong-sign events (the kaon has charge opposite that of the muon). The probability distribution function of

Reproduced with permission of the copyright owner. Further reproduction prohibited without permission.

background was determined by the distribution of wrong-sign events:

$$F_{BG} = \frac{1}{N_{WS}} \sum_{i=1}^{N_{WS}} \delta^4(x - \tilde{x}_i). \tag{4.9}$$

The likelihood for a right-sign event to be background was approximated by the average of F_{BG} over a volume V_{BG} centered on the data point:

$$\bar{F}_{BG}(x) = \frac{1}{V_{BG}} \int_{V_{BG}} d^4x F_{BG}(x). \tag{4.10}$$

The general expression for the probability distribution function is a linear combination of $\bar{F}_{MC}$ and $\bar{F}_{BG}$, weighted according to the estimated amount of background in the right-sign sample:

$$F(x;\mu) = \frac{N_{RS} - N_{WS}}{N_{RS}} \cdot \bar{F}_{MC}(x;\mu) + \frac{N_{WS}}{N_{RS}} \bar{F}_{BG}(x). \tag{4.11}$$

Performing the integrals in Eqns. 4.7 and 4.10, the likelihood function $\mathcal{L}$ is given by:

$$\mathcal{L} = \prod_{i=1}^{N_{RS}} \left[\frac{N_{RS} - N_{WS}}{N_{RS}} \frac{\sum_{\tilde{x}_i in V_i} W(x_i;\mu)}{\sum_{j=1}^{N_{MC}} W(x_j;\mu) V_i} + \frac{N_i}{(V_{BG})_i N_{RS}} \right] \tag{4.12}$$

where N_i is the number of wrong-sign events within the volume $(V_{BG})_i$.

The best estimate of form factors μ, minimized the function $-\log \mathcal{L}$. Numerical calculations were done using the package MINUIT.

4.7 Matrix Method

4.7.1 Motivation

Checks for any potential bias due to neutrino momentum ambiguity were performed by employing a second fitting technique, which treats both neutrino momentum solutions on equal footing. As shown in Section 4.4, the neutrino momentum ambiguity is a major source of smearing. Using this fitting procedure, an attempt was made to eliminate the effects of event misreconstruction due to the two-fold ambiguity of longitudinal neutrino momentum. As a binned method, there are also two additional advantages in comparison to the unbinned loglikelihood:

Reproduced with permission of the copyright owner. Further reproduction prohibited without permission.

1. The normalization of the distribution function is exact and therefore no systematic shifts are expected.

2. No data point is rejected from the fit.

The biggest disadvantage of the method is a lower sensitivity due to the limited number of bins. Unfortunately, systematic errors caused by binning are significantly larger when this second method is used.

4.7.2 General Description

Each Monte Carlo (or data) event can be associated with two points in the four-dimensional kinematic variable space, corresponding to the two ways to reconstruct a decay. For N Monte Carlo generated events there are $2\dot{N}$ points in phase space. Half of these points (N) correspond to the events reconstructed with the correct solution of the neutrino momentum.

Assuming that the four-dimensional phase-space is divided into α bins, the number of points N_i that fall in bin "i" is given by:

$$N_i = p_i \cdot N + \sum_{j=1}^{\alpha} p_j P_{ij} N \tag{4.13}$$

- p_i is the probability for a point determined with the correct solution of neutrino momentum to fall in box "i".

- P_{ij} is the probability for a point determined with the wrong solution of neutrino momentum to fall in box "i", *and* the point determined with the correct solution to fall in box "j".

There are three observations about Eqn. 4.13 :

1. The N_i's do not include any information about the correct choice of neutrino momentum. They are calculated using all $2N$ points.

Reproduced with permission of the copyright owner. Further reproduction prohibited without permission.

2. P_{ij}'s depend exclusively on the D meson momentum in the laboratory frame. They do not depend on the decay mechanism and thus they are not related to the form factors.

3. The probabilities p_i's are the interesting quantities. They are directly related to the decay rate.

To calculate the p_i's it is useful to evaluate first the matrices:

$$A_{ij} = \delta_{ij} + P_{ij} \tag{4.14}$$

$$B_i = \frac{N_i}{N} \tag{4.15}$$

These matrices were evaluated making use of the whole Monte Carlo sample. The kinematic variables are calculated at reconstruction level in the same way as for real data. In order to calculate the matrix A (P_{ij}) the information about the correct sign of neutrino momentum is also needed. This is available from the truth table which contains all information about the decay particles momenta.

The matrices A and B can be used to solve the Eqns 4.13 for p_i's:

$$p = A^{-1} \cdot B \tag{4.16}$$

The probability p_i corresponds to the smeared distribution function $F(\tilde{x}; \mu_0)$ (integrated over the bin "i"), evaluated with the generated form factors μ_0. Using the weighting procedure described in 4.3, the distribution function for arbitrary form factors, $F(\tilde{x}; \mu)$, can be obtained from $F(\tilde{x}; \mu_0)$.

For real data the matrix B had to be recalculated, but the same matrix A could be used because it did not depend on form factors. The information about the decay mechanism is entirely included in matrix B.

Equationn 4.16 can be used again to calculate the probabilities $p_{Data}(i)$. This set of probabilities corresponds to the distribution function $F(\tilde{x}; \mu_{Data})$. The binned loglikelihood method can be applied to extract the best estimate for μ_{Data}. The likelihood for the

Reproduced with permission of the copyright owner. Further reproduction prohibited without permission.

number of events in box "i" is given by:

$$P_i = \frac{\sum_{i=1}^{n_i} W_i(x_i;\mu,\mu_0)}{\sum_{j=1}^{N_{MC}} W_j(x_j;\mu,\mu_0)} \tag{4.17}$$

where n_i is the number of Monte Carlo events found at the reconstruction level within box "i". The numbers n_i are evaluated using the correct sign of the neutrino momentum. N_{MC} is the total number of Monte Carlo events. The best estimate of μ_{Data} is given by the values of the free parameters μ that minimize

$$FCN = -\sum_{i=1}^{\alpha} N_i^{\star} \log P_i(\mu). \tag{4.18}$$

P_i are given by (4.17) and $N_i^{\star}$ is the number of data events with the correct sign of neutrino momentum that fall in box "i". $N_i^{\star}$'s are not directly available, because the correct choice for the neutrino momentum is unknown. However, a good estimate of these numbers is provided by the probabilities $p_{Data}(i)$ multiplied by the number of reconstructed events.

$$N_i^{\star} = p_{Data}(i) \times N \tag{4.19}$$

where N is the total number of real data events after background subtraction.

4.7.3 Including Background

The values of $p_{Data}(i)$ were calculated using Eqn. 4.16. The matrix A is completely determined by the Monte Carlo sample, and the matrix B must be evaluated from real data.

The real data sample contained in fact two subsamples: right-sign, which is a mixture of signal and background; and wrong-sign, which is only background. The matrix B in 4.16 should be simply the difference between B_{RS} and B_{WS}.

$$B = B_{RS} - B_{WS} \tag{4.20}$$

It was assumed that the WS sample correctly models the background in the RS sample. Typically the background is a small fraction of the signal ($\approx 1/5$). Therefore, even if the

Reproduced with permission of the copyright owner. Further reproduction prohibited without permission.

WS sample doesn't model very well the background from RS, one wouldn't expect big changes in the final result unless the extra background in RS, which is not "seen" in WS, is concentrated in a small subregion of the phase-space. As an example, this is the case with the background coming from $D^+ \longrightarrow K^-\pi^+\pi^+$ when the pion is misidentified as an electron. This kind of background was present only in the RS sample. Although this contamination accounts for less than 2% of the total number of RS events, it affects the final results at the 10% level.

4.8 Particle Identification Efficiency

Reference [26] includes a study of the particle identification efficiency in real data versus Monte Carlo. The reason for this study was an earlier observation that particle identification efficiency is not perfectly modeled by the Monte Carlo simulation. The study was done for electrons, kaons and pions. Clean data samples of kaons, pions and electrons were obtained from the constrained decays $D^+ \rightarrow K^-\pi^+\pi^+$ and from photo-conversion ($\gamma \rightarrow e^+e^-$), without applying cuts on particle identification. In this analysis the results given in Ref. [26] for hadrons were used. The relative efficiencies, which are momentum dependent, are listed in Table 4.4.

To take into account the differences in particle identification efficiency between data and Monte Carlo, the weights W_i from Eqn. 4.5 were replaced by:

$$W_i(x;\mu,\mu_0) \longrightarrow W_i(x;\mu,\mu_0) \cdot w_K(p_K)w_\pi(p_\pi) \tag{4.21}$$

where the w's stand for relative particle identification efficiency of data relative to Monte Carlo.

A similar study cannot be done for muons at the same level of accuracy, because there is no constrained decay with muons in the final state to provide enough events for such a study. The eventual mismatch between data and Monte Carlo with respect to muon ID was treated as a distinct source of systematic errors.

Reproduced with permission of the copyright owner. Further reproduction prohibited without permission.

Table 4.4: Weights correcting the inaccuracies in the Monte Carlo K and π identification efficiency for different ranges of track momentum.

Momentum Range (GeV)	K Weight	π Weight
0 - 3	-	0.999 ± 0.022
3 - 6	-	1.003 ± 0.009
6 - 9	0.843 ± 0.038	1.086 ± 0.010
9 - 12	0.943 ± 0.030	1.153 ± 0.012
12 - 15	0.965 ± 0.020	1.288 ± 0.019
15 - 18	0.956 ± 0.019	1.303 ± 0.020
18 - 21	0.961 ± 0.020	1.303 ± 0.021
21 - 24	1.027 ± 0.029	1.236 ± 0.020
24 - 27	1.086 ± 0.038	1.255 ± 0.023
27 - 30	1.116 ± 0.041	1.252 ± 0.025
30 - 33	1.106 ± 0.044	1.269 ± 0.028
33 - 36	1.150 ± 0.051	1.332 ± 0.034
36 - 39	1.172 ± 0.059	1.274 ± 0.034
39 - 42	1.787 ± 0.148	1.315 ± 0.039
42 - 45	2.961 ± 0.389	1.240 ± 0.035
45 - 48	6.489 ± 1.580	1.214 ± 0.039
48 - 51	3.403 ± 0.765	1.240 ± 0.044
51 - 54	4.690 ± 1.524	1.210 ± 0.040
54 - 57	3.912 ± 1.363	1.227 ± 0.048
> 57	3.173 ± 1.180	1.202 ± 0.049

Reproduced with permission of the copyright owner. Further reproduction prohibited without permission.

Chapter 5

Systematic Checks

Systematic uncertainties were classified into three categories depending on which source produced them:

1. Fitting technique.
2. Monte Carlo simulation of detector effects and production mechanism.
3. Background subtraction.

Bin size and systematic shifts are the main sources of systematic uncertainties associated with the fitting technique. Inaccuracies of Monte Carlo simulation generated systematic uncertainties included in the second category. The third category contains systematic uncertainties associated with our lack of knowledge of the background. The amount and shape of the background are sources of systematic uncertainties that contribute to this category.

5.1 Introduction

The ratios of the form factors for the decay channel $D^+ \to K^-\pi^+\mu^+\nu_\mu$ were calculated in a similar way to those for the electronic mode. With the unbinned loglikelihood method,

Reproduced with permission of the copyright owner. Further reproduction prohibited without permission.

the standard Monte Carlo volume was 1/625 of the total phase-space volume. The volume size of each kinematical variable was 1/5 of the total range. For background, the nominal volume was lower, 1/81 of the total. In this case the bin size of each kinematic variable was 1/3 of the full range. The distribution function of background was approximated by the distribution of the wrong-sign events. If the volume centered on the data point did not contain at least 4 Monte Carlo points, then the event was removed from the fit. Because of this restriction, 96 events out of 3629 were removed from the fit. Including the third ratio of form factors as a free parameter in the fit, the results are:

$$R_2 = 0.67 \pm 0.08 \qquad R_V = 1.93 \pm 0.11 \qquad R_3 = -0.07 \pm 0.33$$

where the errors are statistical only, and do not include corrections for the systematic shifts discussed in.

The second fitting technique was intended to be be a check for the first one. In this case the binning was 1/4 of the total range for q^2 and $\cos\theta_l$, 1/5 for $\cos\theta_V$ and 1/3 for χ. The total number of bins was 240. In this method no events were excluded from the fit. The values of the form factor ratios calculated with this fitting technique are:

$$R_2 = 0.72 \pm 0.08 \qquad R_V = 1.90 \pm 0.11 \qquad R_3 = -0.26 \pm 0.34.$$

5.2 Checks of Fitting Techniques

5.2.1 Fit with Known Form Factors

As it was shown in the previous chapter, the unbinned loglikelihood method may be affected by systematic shifts due to approximate normalization of the distribution function and to non-linearity effects. The goal of this study is to evaluate the systematic shifts. The form factors were calculated for subsamples of Monte Carlo events treated as real data. How far away the fitted values are from the generated ones is an accurate estimate of the systematic shifts.

Reproduced with permission of the copyright owner. Further reproduction prohibited without permission.

The full Monte Carlo sample was divided into 32 subsamples, each of them containing about 3000 events. The size of Monte Carlo subsamples was chosen to be comparable with the size of the real data set. The distribution of fit values of R_2, R_V and R_3 for all 32 subsamples are plotted in Fig. 5.1.

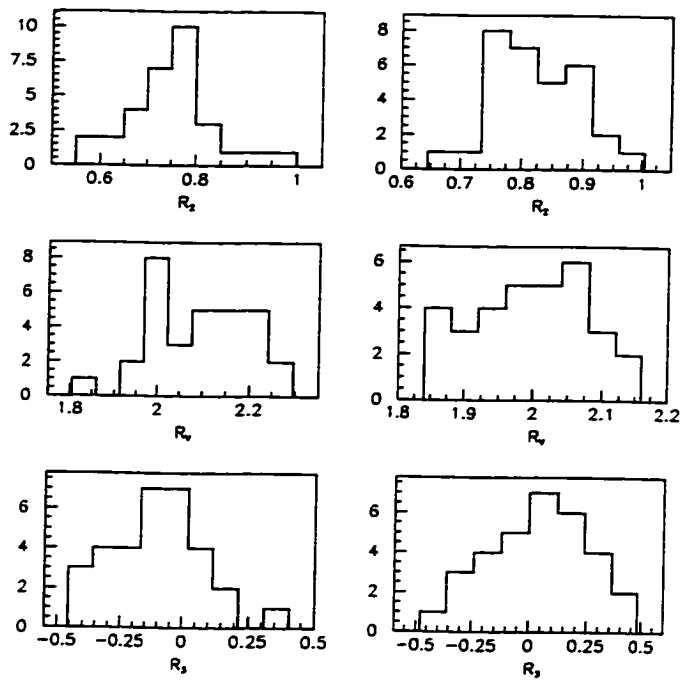

Figure 5.1: Distributions of R_2, R_V and R_3 for the 32 Monte Carlo subsamples. The form factor ratios were calculated with the unbinned loglikelihood method (left side plots) and with the matrix method (right side plots).

The average values of the form factors are

$$\bar{R}_2 = 0.737 \pm 0.014 \qquad \bar{R}_V = 2.090 \pm 0.019 \qquad \bar{R}_3 = -0.107 \pm 0.060.$$

Comparing these values with the generated values of form factors, the systematic shifts are $\delta R_2 = -0.08 \pm 0.01$, $\delta R_V = +0.09 \pm 0.02$, $\delta R_3 = -0.11 \pm 0.06$. These corrections have to be applied to the fitted values of form factor ratios. With the second fitting

Reproduced with permission of the copyright owner. Further reproduction prohibited without permission.

technique, normalization of the probability distribution function is automatically fulfilled, and therefore the systematic shifts are much lower: $\delta R_2 = +0.004 \pm 0.014$, $\delta R_V = 0.001 \pm 0.019$, $\delta R_3 = -0.012 \pm 0.060$.

5.3 Monte Carlo Volume Size

When fits were performed with the unbinned method, the distribution function was estimated from Monte Carlo points that fall within a volume centered on each data point. The size of this volume was determined by the binning of each kinematical variable. The full range of each kinematical variable is: $q^2/q^2_{max} = [0;1]$, $\cos\theta_l = [-1;1]$, $\cos\theta_V = [-1;1]$ and $\chi = [0;2\pi]$. In the standard binning, the nominal volume corresponded to 1/5 of the full range for each variable. If the data point is close to the edge of phase space, the volume is shrunk such that the volume remains centered on the data point. In this way the results are not affected if the distribution function varies linearly within the volume. Ideally, the volume centered on a data point should be very small to avoid non-linearity effects and to ensure the normalization condition. On the other hand, for small volumes the estimated distribution function is affected by large uncertainties due to limited statistics of the Monte Carlo sample. It is expected that results should be stable for a range of volume sizes.

A check was done to determine the stability ranges of each variable and the systematic errors related to the change of Monte Carlo volume size. The volume size was varied from 1 to 1/9 of the total range in one variable at a time, holding the size of the other three constant. The systematic shifts, very sensitive to binning, were calculated in each case. The corrected values of form factors are plotted in Fig. 5.2 and Fig. 5.3. The fifth point from the left (open circle) represents the standard nominal volume size.

The fit was stable for the following ranges of volume size: $0.11 < q^2/q^2_{max} < 0.33$; $0.22 < \cos\theta_l < 0.67$; $0.22 < \cos\theta_V < 0.67$; $0.70 < \chi < 6.28$. In the stable region the fluctuations of form factor ratios are $\sigma_{R_2} = 0.02$, $\sigma_{R_V} = 0.02$, $\sigma_{R_3} = 0.12$.

Reproduced with permission of the copyright owner. Further reproduction prohibited without permission.

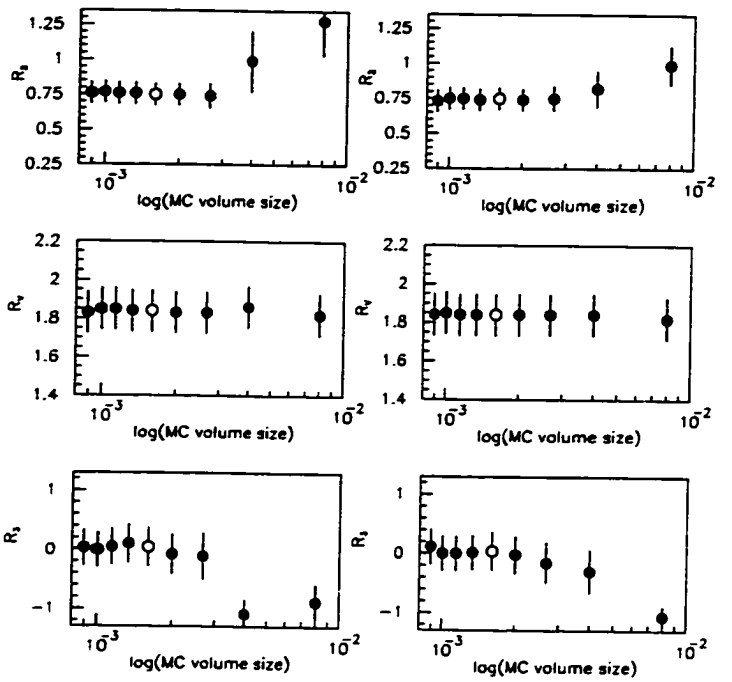

Figure 5.2: Values of form factor ratios calculated with different Monte Carlo volume sizes. The ranges of q^2/q^2_{max} (left side) and $\cos\theta_l$ (right side) were varied from 1 to 1/9 of the total range. The open circle corresponds to standard binning. Fits were performed with the first fitting technique.

A similar study was done with the second fitting technique. The size of each bin was varied by a factor up to 2 for each variable, holding the other three at the nominal value. In this case the fit is approximately stable in the following ranges of volume size: $0.14 < q^2/q^2_{max} < 0.33$; $0.22 < \cos\theta_l < 0.67$; $0.22 < \cos\theta_V < 0.67$ and $1.57 < \chi < 6.28$. The fluctuations of the form factor ratios are $\sigma_{R_2} = 0.06$, $\sigma_{R_V} = 0.10$, $\sigma_{R_3} = 0.30$.

Reproduced with permission of the copyright owner. Further reproduction prohibited without permission.

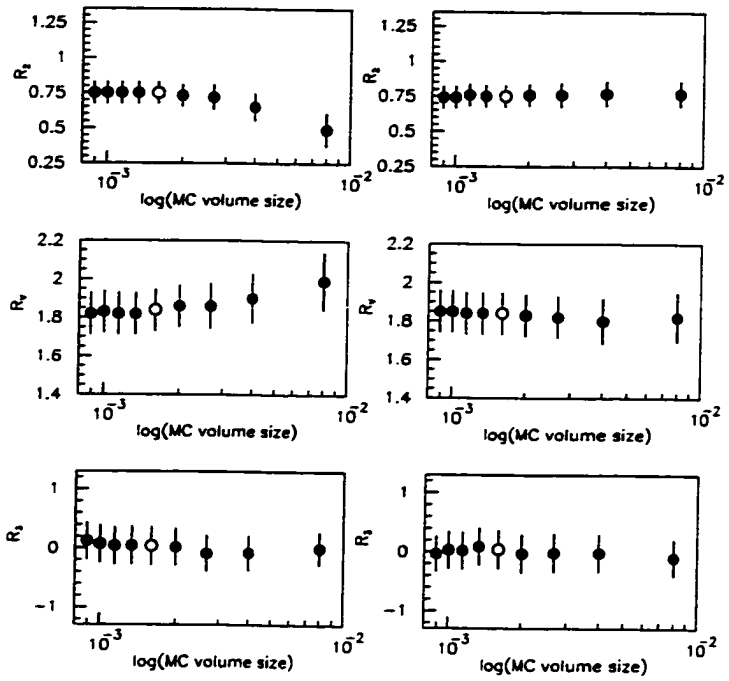

Figure 5.3: Values of form factor ratios calculated with different Monte Carlo volume sizes. The ranges of $\cos\theta_V$ (left side) and χ (right side) were varied from 1 to 1/9 of the total range. The open circle corresponds to standard binning. Fits were performed with the first fitting technique.

5.3.1 Number of Monte Carlo Points Associated with Each Data Point

As mentioned before, the Monte Carlo points that fall in the small volume centered on a data point determine the likelihood function. With many such points found within a small volume, the likelihood function is accurately determined. The minimum number of Monte Carlo points required to fall within the volume surrounding a data point was 4. If this condition was not met, the data point was removed from the fit. Raising the value of the minimum number of Monte Carlo points (n_{MCmin}) the resolution of the likelihood function increases, but there are more data points that are excluded from the fit. Values

Reproduced with permission of the copyright owner. Further reproduction prohibited without permission.

of form factor ratios were determined as n_{MCmin} was varied from 1 to 7. The results are in Table 5.1.

Table 5.1: Values of form factor ratios calculated with various conditions on the minimum number of Monte Carlo points (n_{MCmin}).

n_{MCmin}	R_2	R_V	R_3	# rej.
1	0.76 ± 0.08	1.84 ± 0.11	-0.20 ± 0.23	23
2	0.74 ± 0.08	1.85 ± 0.11	-0.10 ± 0.36	53
3	0.74 ± 0.08	1.84 ± 0.11	-0.03 ± 0.35	77
4	0.75 ± 0.08	1.84 ± 0.11	0.04 ± 0.34	96
5	0.75 ± 0.08	1.84 ± 0.11	0.12 ± 0.34	127
6	0.75 ± 0.08	1.84 ± 0.11	0.06 ± 0.33	142
7	0.75 ± 0.08	1.85 ± 0.11	0.07 ± 0.32	160

The variations of form factor ratios are $\sigma_{R_2} = 0.01$, $\sigma_{R_V} = 0.01$, $\sigma_{R_3} = 0.18$.

With the second fitting technique there is no similar requirement. Bins in this case do not intersect and they cover the whole phase space. Therefore no data point was removed from the fit, whatever the size of the bins. However, a small value of the bin size would lower the statistics of Monte Carlo points found within each bin and consequently the resolution in determining the distribution function would be low. In the case of standard binning (240 bins) there were on average about 400 Monte Carlo points per bin. The fluctuations of the results when the bin size was modified, were studied in the previous subsection.

5.4 Simulation of Detector Effects

The accuracy of the results depends heavily on how well the Monte Carlo sample incorporates detector effects. As already mentioned in Chapter 4, the efficiency of hadron

Reproduced with permission of the copyright owner. Further reproduction prohibited without permission.

identification was not the same in data and Monte Carlo. Some other inconsistencies were studied, and their contributions to the systematic errors were evaluated.

5.4.1 Hadron Identification

In this analysis the hadron identification was based on Cerenkov information. The identification efficiency was not the same in data and Monte Carlo. As pointed out in Ref. [26], the relative identication efficiencies, data vs. Monte Carlo, are momentum-dependent. They are listed in Table 4.4 for both the kaon and the pion, and are plotted in Fig. 5.4 as functions of hadron momentum. The effects of these corrections on the values of form factor ratios are shown in Table 5.2. The corrections to hadron identification were according to either the step functions from Table 4.4, or the continuous functions plotted in Fig. 5.4.

Table 5.2: The values of form factor ratios calculated with different combinations of hadron ID corrections.

	R_2	R_V	R_3
K and π ID corr. applied	0.75 ± 0.08	1.84 ± 0.11	0.04 ± 0.33
No hadron ID corr. applied	0.71 ± 0.08	1.93 ± 0.11	0.32 ± 0.33
K ID corr. applied	0.74 ± 0.08	1.87 ± 0.11	0.03 ± 0.33
π ID corr. applied	0.72 ± 0.08	1.90 ± 0.11	0.25 ± 0.33
Smooth corrections applied	0.74 ± 0.08	1.85 ± 0.11	0.02 ± 0.33

The corrections on kaon identification efficiency have a larger effect on the values of form factor ratios than the pion identification efficiency corrections. To determine the systematic errors associated to these corrections, for each of the two hadrons 100 fits were performed, where the weight associated with each momentum bin was modified by a gaussian fluctuation with the resolution given by the error on the weight. The study was done for both fitting techniques, and the results are summarized in Table 5.3.

Errors related to hadron efficiecy corrections are well below the statistical and other sys-

Reproduced with permission of the copyright owner. Further reproduction prohibited without permission.

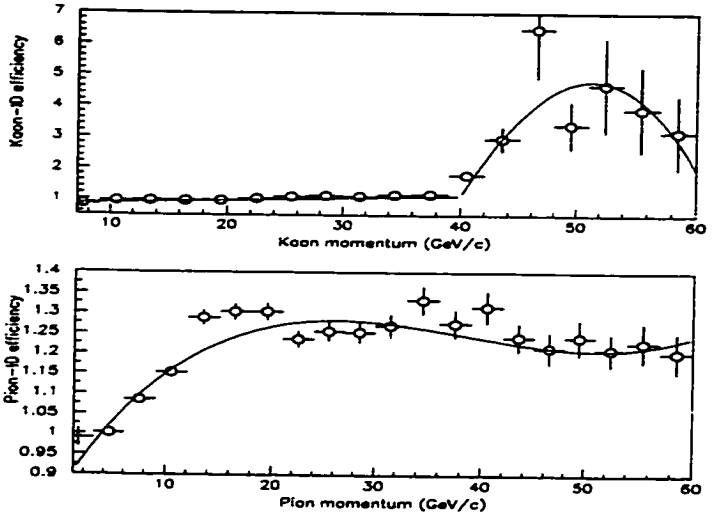

Figure 5.4: Weights correcting the inaccuracies in the Monte Carlo K and π identification efficiency for different ranges of track momentum. Continuous curves represent a fit to polynomial functions.

tematic errors.

5.4.2 Muon Identification

It is known that Monte Carlo simulation does not always describe properly all the effects that might contribute to muon identification (muon wall efficiencies, multiple scattering, TDC information, noise, choosing the muon candidate, etc.). Therefore an effort was made to keep as many muon candidates as possible in order to make the analysis less dependent on how well Monte Carlo models real data. The sources of systematic errors due to muon identification were classified in two categories:

1. Detector effects related to muon identification (muon wall efficiencies, multiple scattering, TDC, noise).

Reproduced with permission of the copyright owner. Further reproduction prohibited without permission.

Table 5.3: Systematic errors due to hadron identification efficiencies.

	First Method			Second Method		
Particle ID	σ_{R_2}	σ_{R_V}	σ_{R_3}	σ_{R_2}	σ_{R_V}	σ_{R_3}
kaon	0.005	0.004	0.021	0.011	0.012	0.021
pion	0.001	0.001	0.001	0.003	0.002	0.005
total	0.01	0.01	0.02	0.01	0.01	0.02

2. Ambiguity in choosing the muon candidate when two tracks from the secondary vertex passed all muon ID cuts.

Detector effects

The muon identification schema described in Appendix B keeps about 85% of the muons that passed substrip cuts and had momentum larger than 8 GeV. Still, the data sample may not contain the "same" muons as the Monte Carlo sample. All detector effects related to muon identification depend on muon momentum. Therefore, the variations of the fit values of form factors for different cuts applied to muon momentum are a good measure of the systematic errors related to detector effects. Table 5.4 contains the values of the form factor ratios for different cuts on the lower bound of muon momentum as well as the numbers of events that passed all cuts.

Compared to $p_\mu > 8$ GeV, which is the analysis cut on muon momentum, the largest variation of R_2 is $\delta R_2 = 0.074$ and it occurs for $p_\mu > 14$ GeV. Part of this variation is due to statistical fluctuations. To evaluate statistical contribution, form factor ratios were first calculated for 32 Monte Carlo subsamples with the cut $p_\mu > 8$ GeV and then with a tighter cut on muon momentum ($p_\mu > 14$ GeV). The RMS for the differences of R_2 between the two sets of results was 0.050. The largest variation of R_2 due to muon identification procedure was estimated at $\delta R_2 = \sqrt{0.074^2 - 0.050^2} = 0.05$. In a similar manner the largest variations of R_V and R_3 were determined: $\delta R_V = 0.06$ and $\delta R_3 = 0.15$.

Reproduced with permission of the copyright owner. Further reproduction prohibited without permission.

Table 5.4: Values of form factor ratios calculated with the unbinned method, for different cuts on the lower bound of muon momentum. Fit values were not corrected for systematic shifts.

p_μ	RS	WS	MC	R_2	R_V	R_0
7	3795	635	98408	0.77 ± 0.08	1.88 ± 0.11	-0.11 ± 0.34
8	3628	595	95579	0.75 ± 0.08	1.84 ± 0.11	-0.27 ± 0.34
9	3445	561	92297	0.75 ± 0.08	1.80 ± 0.11	-0.33 ± 0.34
10	3287	530	88506	0.74 ± 0.09	1.77 ± 0.11	-0.29 ± 0.35
11	3114	490	84393	0.74 ± 0.10	1.78 ± 0.12	-0.34 ± 0.36
12	2942	461	80035	0.70 ± 0.10	1.78 ± 0.12	-0.23 ± 0.37
13	2789	431	75405	0.70 ± 0.10	1.81 ± 0.12	-0.31 ± 0.38
14	2604	402	70700	0.68 ± 0.10	1.76 ± 0.13	-0.21 ± 0.44
15	2422	374	66138	0.71 ± 0.11	1.77 ± 0.13	-0.01 ± 0.47
16	2249	339	61708	0.74 ± 0.11	1.74 ± 0.13	$+0.10 \pm 0.49$

Ambigiuty of the muon candidate

In addition to the hardware effects described in the previous subsection, there are also systematic errors related to assignment of the muon candidate. This happens when two tracks pass muon ID cuts. The data contains 8.4% such events while Monte Carlo only 4.7%; the Monte Carlo didn't describe properly the complexity of a real event. In the standard procedure, the track with the highest muon category was chosen as the muon candidate. If the event didn't pass the other cuts, then the second possibility was also tested. To estimate the uncertainties due to this effect, the form factors were calculated for two other reasonable ways to select the muon candidate:

1. The muon candidate always has the highest muon category.

2. Both combinations are kept in the data sample if they pass all selection criteria.

Reproduced with permission of the copyright owner. Further reproduction prohibited without permission.

The results of the fit are shown in Table 5.5.

Table 5.5: The values of form factor ratios, calculated with the unbinned method, for different ways (described in the text) to solve the ambiguity of muon candidate.

	RS	WS	MC	R_2	R_V	R_0
"Standard"	3628	595	95579	0.75 ± 0.08	1.84 ± 0.11	0.04 ± 0.33
1	3461	534	93910	0.79 ± 0.08	1.82 ± 0.11	-0.06 ± 0.33
2	3686	597	96261	0.77 ± 0.08	1.88 ± 0.11	0.03 ± 0.34

Similar calculations were performed with the second fitting technique. The results for muon identification systematic errors are summarized in the Table 5.6. The contribution of this source to the systematic uncertainties associated with muon identification is comparable with the hardware effects for R_2 and R_V, and is three times lower for R_3.

Table 5.6: The systematic errors due to muon identification.

	First Method			Second Method		
Source	σ_{R_2}	σ_{R_V}	σ_{R_3}	σ_{R_2}	σ_{R_V}	σ_{R_3}
Detector effects	0.03	0.04	0.10	0.04	0.03	0.10
Ambiguity of muon cand.	0.03	0.04	0.03	0.02	0.04	0.04
Total muon ID	0.04	0.06	0.10	0.05	0.04	0.11

5.4.3 Production Mechanism

Because D mesons are spinless, details of the production mechanism should not play an important role in this analysis. However, it is important that the D momentum distributions be correctly modeled by Monte Carlo sample. Figure 5.5 shows the distributions of D total momentum (in lab frame) and of the transverse component with respect to the beam axis. For the total D momentum the agreement between data and Monte Carlo

Reproduced with permission of the copyright owner. Further reproduction prohibited without permission.

was fairly good, but this was not the case with the second distribution. The transverse D momentum distribution is directly correlated with acceptance effects.

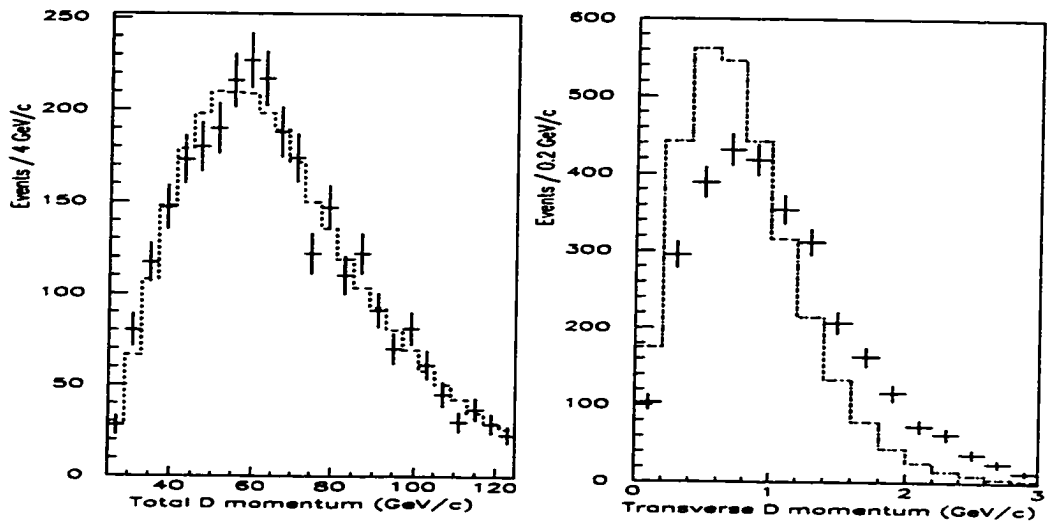

Figure 5.5: D momentum distributions for background subtracted data (error bars) overlaid with the similar Monte Carlo distributions.

To account for these differences, each Monte Carlo event was weighted with the ratio of data to Monte Carlo efficiencies. The values of the weights are plotted in Fig. 5.6 as a function of transverse momentum. Table 5.7 contains the values of form factor ratios when weights were applied, and when weights were not applied. Overall, the effect of these corrections is rather small.

Table 5.7: The values of form factor ratios calculated with different combinations of $(p_D)_\perp$ corrections.

	R_2	R_V	R_3
Correction applied	0.75 ± 0.08	1.84 ± 0.11	0.04 ± 0.33
No correction applied	0.75 ± 0.08	1.82 ± 0.11	-0.04 ± 0.34
Smooth correction applied	0.75 ± 0.08	1.84 ± 0.11	-0.01 ± 0.33

Reproduced with permission of the copyright owner. Further reproduction prohibited without permission.

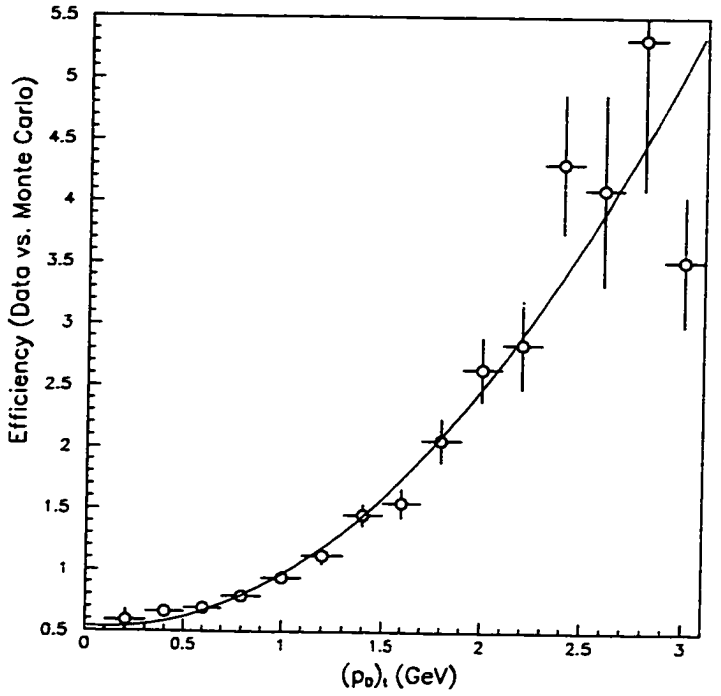

Figure 5.6: Weights correcting the inaccuracies in the Monte Carlo $(p_D)_\perp$ distribution. Continuos curves represent a fit to a polynomial function.

To estimate the systematic errors due to this correction, 100 fits were performed where the weight associated with each transverse momentum bin was modified by a gaussian fluctuation with the resolution given by the error on the weight. The RMS spread of the fit values gave the uncertainty due to this effect. The systematic errors are rather small for all three form factor ratios:

first method:	$\delta R_2 = 0.01$	$\delta R_V = 0.01$	$\delta R_3 = 0.02$
second method:	$\delta R_2 = 0.01$	$\delta R_V = 0.01$	$\delta R_3 = 0.03$

Reproduced with permission of the copyright owner. Further reproduction prohibited without permission.

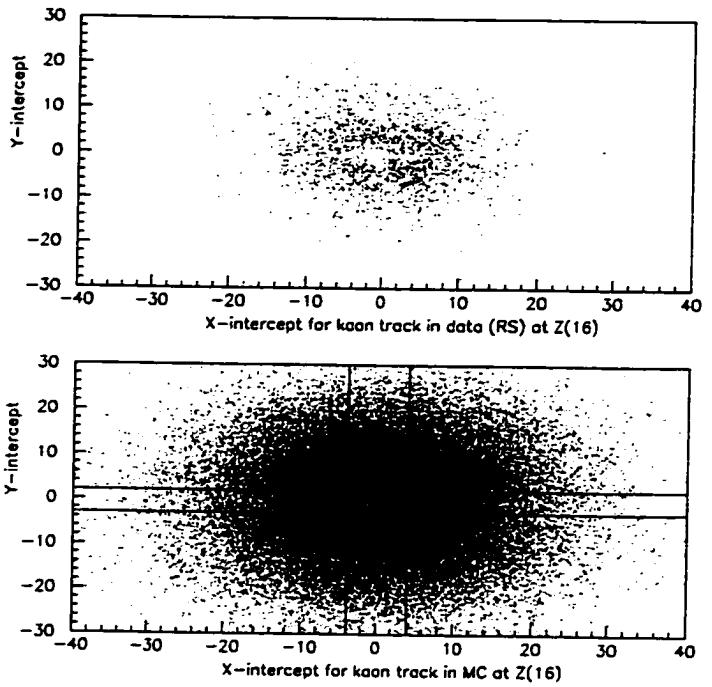

Figure 5.7: Distribution of muon tracks intercepts, data (top) and Monte Carlo (bottom), at the z-position of the 16th drift chamber. The points were determined by their x and y positions measured in cm.

5.4.4 Spectrometer acceptance

The flux of high energy particles is much more intense in the region close to the beam axis of the spectrometer than in the outer regions. Therefore the detection efficiency of the drift chambers decreased in time in a small region around the beam axis. The Monte Carlo sample included this effect in an integrated manner. In the Monte Carlo simulation the extent of the "DC hole" was assumed to be as big as one would expect at the middle of the run. An illustration of the "DC hole" at the 16th drift chamber is shown in Fig. 5.7. This model of the time-dependent "DC hole" is correct if Monte Carlo sample simulates the entire data sample, and if the decrease of the drift chambers efficiency is

Reproduced with permission of the copyright owner. Further reproduction prohibited without permission.

linear in time. The inaccuracies of the Monte Carlo simulation related to modeling of the spectrometer acceptance associated with the "DC hole" were addressed as a source of systematic uncertainties.

To estimate the systematic errors associated with this effect, the form factor ratios were determined with different assumptions about the size and the detection efficiency in the "DC hole" region. Monte Carlo events that have at least one track passing through the "DC hole" were weighted by a factor which was varied from 0 to 2. The fits were performed for three different sizes of the "DC hole", determined by their x and y positions evaluated at the z-position of the 16th drift chamber plane:

1. $-5.0 < x < 5.0$ cm $\quad -5.5 < y < 4.5$ cm
2. $-2.5 < y < 1.5$ cm
3. $-4.0 < x < 4.0$ cm $\quad -3.0 < y < 2.0$ cm

The fit value results for different definitions of the "DC hole" are shown in Table 5.8. Fits were performed with the first fitting technique. The first column in Table 5.8 contains the index of the "DC hole" definition (shown above) and the second column contains the weight applied to Monte Carlo events. No weighting was applied to data events. The systematic uncertainties associated to acceptance effects are $\sigma_{R_2} = 0.03$, $\sigma_{R_V} = 0.02$ and $\sigma_{R_3} = 0.08$. When the fits were performed with the second fitting technique, the systematic errors are $\sigma_{R_2} = 0.02$, $\sigma_{R_V} = 0.02$ and $\sigma_{R_3} = 0.09$.

5.4.5 Final Cut Selection

The goal of these checks was to estimate how well Monte Carlo simulation models the variables used in the final cut selection (CART cut). The final analysis cut was replaced by 14 other CART cuts. Results obtained with the first fitting technique are summarized in Table 5.9.

Reproduced with permission of the copyright owner. Further reproduction prohibited without permission.

Table 5.8: Study of the systematic uncertainties associated with spectrometer acceptance effects.

DC hole def.	MC	weight	R_2	R_V	R_3
1	54385	0.0	0.82 ± 0.08	1.83 ± 0.11	0.21 ± 0.32
1	74819	0.5	0.78 ± 0.08	1.82 ± 0.11	0.13 ± 0.33
1	116339	1.5	0.73 ± 0.08	1.85 ± 0.11	-0.02 ± 0.33
1	136773	2.0	0.71 ± 0.08	1.86 ± 0.11	-0.03 ± 0.33
2	59127	0.0	0.78 ± 0.08	1.80 ± 0.11	0.16 ± 0.33
2	77353	0.5	0.76 ± 0.08	1.82 ± 0.11	0.07 ± 0.33
2	113805	1.5	0.74 ± 0.08	1.86 ± 0.11	0.02 ± 0.33
2	132031	2.0	0.73 ± 0.08	1.87 ± 0.11	-0.01 ± 0.33
3	79070	0.0	0.77 ± 0.08	1.84 ± 0.11	0.16 ± 0.33
3	87324	0.5	0.75 ± 0.08	1.84 ± 0.11	0.06 ± 0.33
3	103834	1.5	0.74 ± 0.08	1.84 ± 0.11	0.02 ± 0.33
3	112088	2.0	0.74 ± 0.08	1.84 ± 0.11	0.00 ± 0.33

The spread of the results around the average values are: $\sigma_{R_2} = 0.03$, $\sigma_{R_V} = 0.04$ and $\sigma_{R_3} = 0.09$ for the first fitting method and $\sigma_{R_2} = 0.03$, $\sigma_{R_V} = 0.05$ and $\sigma_{R_3} = 0.13$ when the fits were performed with the second fitting method.

The final data sample was quite clean, but still contained background events. The major source of backgound was fake vertices due to reconstruction errors. This background component is modeled by the wrong-sign sample. In addition to this background, the final data sample might also contain other charm decay modes. To account for any background contribution one should know precisely the number of events corresponding to each decay mode and also details about the decay mechanism in each case (decay rate expressions, form factors, phases, etc.). This level of detail is impossible to obtain. Instead, we estimated the systematic errors due to the lack of knowledge about the charmed background

Reproduced with permission of the copyright owner. Further reproduction prohibited without permission.

Table 5.9: The number of events and the values of form factors calculated with the unbinned method for 14 sets of CART cuts.

	RS	WS	MC	R_2	R_V	R_3
standard cuts	3629	595	95579	0.75 ± 0.08	1.84 ± 0.11	0.04 ± 0.33
CART1	3517	538	93384	0.75 ± 0.08	1.92 ± 0.11	0.17 ± 0.33
CART2	3676	621	95214	0.75 ± 0.08	1.87 ± 0.11	0.24 ± 0.32
CART3	3416	585	87419	0.77 ± 0.08	1.86 ± 0.11	0.04 ± 0.34
CART4	3767	688	93462	0.74 ± 0.08	1.91 ± 0.11	0.02 ± 0.33
CART5	3198	420	85929	0.81 ± 0.08	1.87 ± 0.11	0.17 ± 0.32
CART6	3744	656	96146	0.70 ± 0.08	1.86 ± 0.11	0.09 ± 0.33
CART7	3133	424	84980	0.71 ± 0.08	1.79 ± 0.11	0.14 ± 0.32
CART8	3228	461	85587	0.74 ± 0.08	1.93 ± 0.11	0.25 ± 0.31
CART9	3960	739	100089	0.74 ± 0.08	1.90 ± 0.11	0.16 ± 0.33
CART10	3371	524	86298	0.71 ± 0.08	1.92 ± 0.11	0.11 ± 0.33
CART11	3697	606	96864	0.74 ± 0.08	1.86 ± 0.11	-0.02 ± 0.31
CART12	3399	524	89696	0.72 ± 0.08	1.84 ± 0.11	0.25 ± 0.34
CART13	3523	549	91272	0.79 ± 0.08	1.85 ± 0.11	0.02 ± 0.33
CART14	3583	590	95142	0.71 ± 0.08	1.83 ± 0.11	-0.02 ± 0.33

by adding up (in quadrature) the variations of form factor ratios when:

1. the amount of non-charmed background was varied within a large range;
2. the shape of the non-charmed background was changed.

5.4.6 Number of Background Events

The number of background events in the right-sign sample was assumed to be the same as in the wrong-sign sample. We may expect that this assumption was not totally correct.

Reproduced with permission of the copyright owner. Further reproduction prohibited without permission.

A check was done to estimate how much the results of the fit change when the expected number of background events was varied. The amount of background was varied by 50% around the expected value by weighting the wrong-sign events with a factor between 0.5 and 1.5. When the fits were performed with the unbinned method, the values of R_V and R_3 are approximately stable; R_2 fluctuated with a bit more than half of the statistical error. Results of the fits are shown in Fig. 5.8. Systematic errors associated with background amount uncertainties are $\sigma_{R_2} = 0.04$, $\sigma_{R_V} = 0.02$, $\sigma_{R_3} = 0.06$.

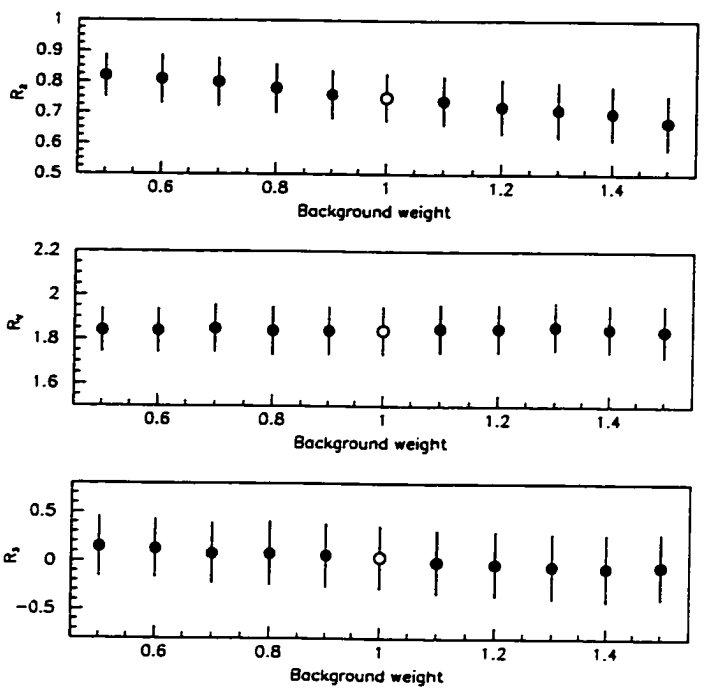

Figure 5.8: The values of form factor ratios for different background weights.

When the fits were performed with the second fitting technique, the weights applied to wrong-sign events were also in the range from 0.5 to 1.5. The results are shown in Table 5.10.

With this method, the amount of background cannot be overestimated by too large a factor because the number of wrong-sign events may then be larger than the number

Reproduced with permission of the copyright owner. Further reproduction prohibited without permission.

Table 5.10: Values of form factor ratios calculated with different background weights. Fits were performed with the second fitting technique.

Weight	R_2	R_V	R_3
0.7	0.74 ± 0.08	1.91 ± 0.11	-0.01 ± 0.33
0.8	0.73 ± 0.08	1.91 ± 0.11	-0.13 ± 0.34
0.9	0.73 ± 0.08	1.90 ± 0.11	-0.24 ± 0.34
1.0	0.72 ± 0.08	1.90 ± 0.11	-0.25 ± 0.34
1.1	0.72 ± 0.08	1.89 ± 0.11	-0.35 ± 0.34
1.2	0.71 ± 0.08	1.88 ± 0.11	-0.42 ± 0.34
1.3	0.70 ± 0.08	1.87 ± 0.11	-0.47 ± 0.33
1.4	0.69 ± 0.09	1.87 ± 0.11	-0.49 ± 0.32
1.5	0.67 ± 0.09	1.86 ± 0.11	-0.50 ± 0.35

of right-sign ones in some bins, and background subtraction would be meaningless. The systematic errors due to the amount of background estimation are $\sigma_{R_2} = 0.04$, $\sigma_{R_V} = 0.03$, $\sigma_{R_3} = 0.25$.

5.4.7 Background Shape

The systematic uncertainties associated with background shape were due to two sources:

1. The model used to describe the background.
2. The limited size of the estimated background.

Background model

In this analysis background is modeled by the wrong-sign decays reconstructed in the signal region. To test the sensitivity of the form factor ratios to background shape, wrong-sign

Reproduced with permission of the copyright owner. Further reproduction prohibited without permission.

events were weighted by a linear-shaping function for each kinematic variable at a time:

$$weight = 1 + slope(x - \overline{x})$$

where x can be any of the four kinematic variables and $\overline{x}$ is the mean value of x.

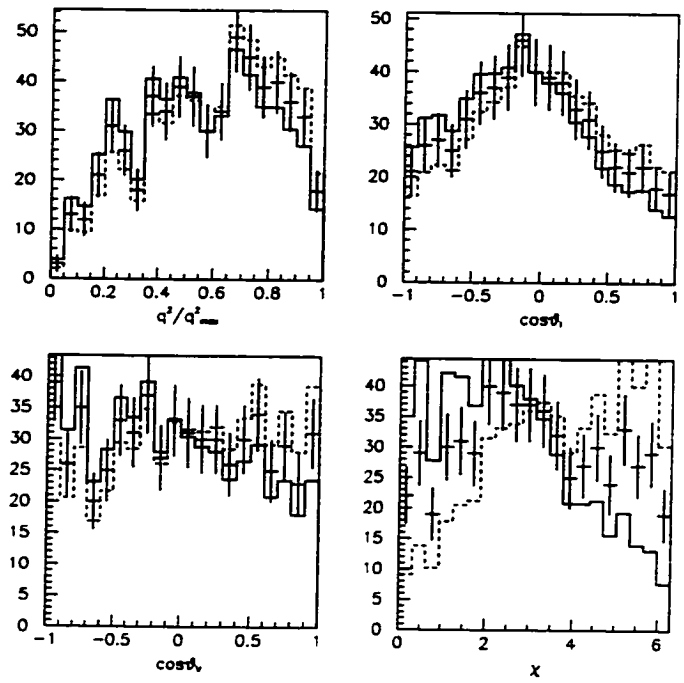

Figure 5.9: Distributions of kinematic variables for WS events within the signal region (crosses), overlaid with two extreme distributions of background (continuous and dotted lines).

Values of the slope were varied in the ranges $(-0.5; 0.5)$ for q^2/q^2_{max}, $(-0.25; 0.25)$ for $\cos\theta_l$ and $\cos\theta_V$ and $(-0.2; 0.2)$ for χ. Figure 5.9 shows how much the background shape has changed when this weighting procedure was applied. Comparison of the background estimated from wrong-sign events in the signal region, and from a sample of right-sign events with a large background component ($K\pi$ mass outside the signal region), shows

Reproduced with permission of the copyright owner. Further reproduction prohibited without permission.

that background shape cannot change more than in Fig. 5.10.

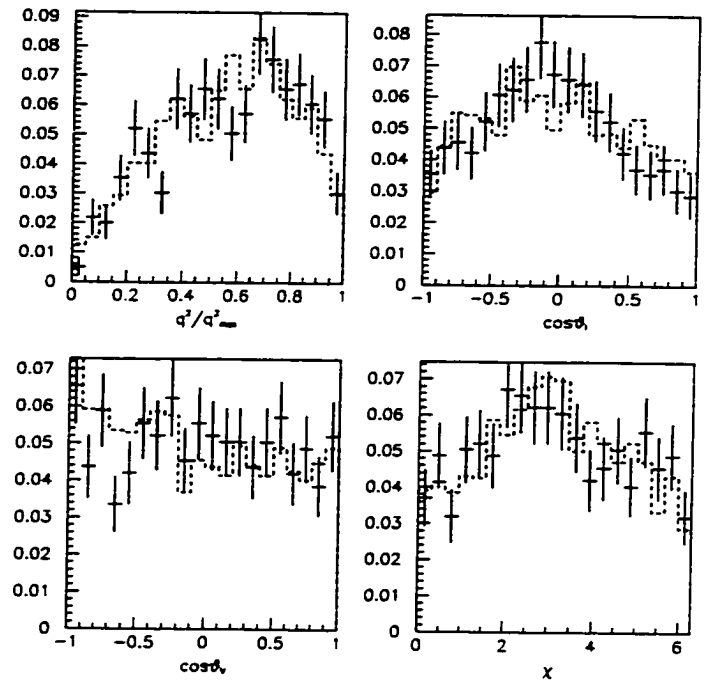

Figure 5.10: Distributions of kinematic variables outside the signal region ($M_{K\pi}$ not in (0.85;0.94) GeV). RS events are shown as black dots, overlaid with the corresponding distributions of WS events in the signal region.

The systematic uncertainties due to the background model are $\sigma_{R_2} = 0.03$, $\sigma_{R_V} = 0.04$ and $\sigma_{R_3} = 0.04$ when the fits were performed with the first fitting technique, and $\sigma_{R_2} = 0.03$, $\sigma_{R_V} = 0.04$ and $\sigma_{R_3} = 0.08$ when the fits were performed with the second fitting technique.

Background volume size

In the unbinned method, the number of wrong-sign events within a volume centered on a data point, divided by the total number of wrong sign events, is assumed to be an

Reproduced with permission of the copyright owner. Further reproduction prohibited without permission.

estimate of the background distribution function evaluated at the position of the data point. Thus, the shape of the background (the distribution function) depends on the background volume size. With a very large WS sample the background volume size can be chosen very small and this source of systematic uncertainties wouldn't exist.

In the same way as was done for Monte Carlo volume size, the range of each variable was varied from 1 to 1/5, holding the other three at the nominal value 1/3. The variations of the form factor ratios are $\sigma_{R_2} = 0.02$, $\sigma_{R_V} = 0.02$, $\sigma_{R_3} = 0.05$.

The second fitting technique does not contain any binning for background. The number of wrong-sign events is subtracted from the number of right-sign events that fall in each bin, before performing the fit.

The two systematic uncertainties associated with background shape (background model and background volume size) were added in quadrature. The final values of the systematic uncertainties due to background shape are $\sigma_{R_2} = 0.04$, $\sigma_{R_V} = 0.04$ and $\sigma_{R_3} = 0.06$ when the fits where performed with the first fitting technique, and $\sigma_{R_2} = 0.04$, $\sigma_{R_V} = 0.04$ and $\sigma_{R_3} = 0.08$ when the fits were performed with the second fitting technique.

5.5 Other Checks

The checks described in this section were not included as distinct sources of systematic errors. Their goal was to check the consistency of the statistical errors returned by fitting routines, and also to check the systematic errors determined in the previous three sections. All fits were performed only with the first fitting technique.

5.5.1 Fitting Subsamples of the Data

The full data sample was divided into two and three independent subsamples. The results are shown in Table 5.11. The fit results are consistent with one another and with the results of the fit to the entire data sample. Also the statistical errors increase roughly by

Reproduced with permission of the copyright owner. Further reproduction prohibited without permission.

a factor $\sqrt{2}$ in the first case and $\sqrt{3}$ in the second case, as expected.

Table 5.11: Results of systematic checks of data selection. The fits were performed with the unbinned loglikelihood method and corrections for systematic shifts were applied.

2 subsamples						
No.	RS	WS	MC	R_2	R_V	R_3
1	1821	291	95579	0.72 ± 0.11	1.86 ± 0.15	0.20 ± 0.49
2	1808	304	95579	0.76 ± 0.11	1.82 ± 0.15	0.14 ± 0.43
3 subsamples						
1	1217	191	95579	0.80 ± 0.14	1.77 ± 0.18	0.40 ± 0.42
2	1199	209	95579	0.79 ± 0.15	2.02 ± 0.19	-0.16 ± 0.59
3	1213	195	95579	0.85 ± 0.19	1.78 ± 0.18	-0.45 ± 0.78
D Charge						
D^+	1534	298	47069	0.79 ± 0.14	1.86 ± 0.17	-0.21 ± 0.44
D^-	2095	297	48510	0.78 ± 0.10	1.86 ± 0.14	0.31 ± 0.36
$M_{K\pi}$ Mass						
$M_{K\pi} \in (0.84; 0.896)$	1996	292	50785	0.74 ± 0.11	1.82 ± 0.14	-0.20 ± 0.38
$M_{K\pi} \in (0.896; 0.94)$	1663	303	44794	0.80 ± 0.13	1.95 ± 0.17	0.34 ± 0.43
Choice of Neutrino Momentum						
negative	3629	595	95579	0.75 ± 0.08	1.84 ± 0.11	0.04 ± 0.33
positive	3629	595	95579	0.63 ± 0.11	1.77 ± 0.12	-0.30 ± 0.54
matrix method	3629	595	95579	0.72 ± 0.08	1.90 ± 0.11	-0.25 ± 0.34

5.5.2 Charge Dependence

Fits were performed separately for the D^+ and D^- samples. Each subsample was fit with a Monte Carlo sample having events with the same vertex charge as data. The results of the fits are shown in Table 5.11. The differences between the two sets of results are within

Reproduced with permission of the copyright owner. Further reproduction prohibited without permission.

the statistical errors.

5.5.3 $M_{K\pi}$ Dependence

The signal region corresponds to $M_{K\pi} \in (0.85; 0.94)$ GeV. Fits were performed for two subsamples having $M_{K\pi}$ lower and higher than the central value of M_{K^*} (= 0.896 GeV). The results are listed in Table 5.11. The values of form factor ratios are consistent with each other and with the results of the fit to the entire data sample.

5.5.4 Choice of Neutrino Momentum

The events $D^+ \to K^-\pi^+\mu^+\nu_\mu$ cannot be fully reconstructed due to the undetected neutrino. Using the constraint of D mass there is still a two-fold ambiguity for the longitudinal neutrino momentum (see Appendix A) caused by the missing information about the parent particle momentum. When the fits were performed with the unbinned method, the events were reconstructed with the negative solution of neutrino momentum. This choice is motivated by the significantly higher systematic shifts when the events are reconstructed with the positive solution ($\delta R_2 = -0.17$, $\delta R_V = 0.12$, $\delta R_3 = -0.03$), and also by higher anticorrelation between R_2 and R_3 (-0.568 comparred to -0.211). The results of the fit when the events were reconstructed with the positive solution of the neutrino momentum are shown in Table 5.11. The above corrections for the systematic shifts were applied after the fit.

The second fitting technique is not affected by the choice of neutrino momentum. Intuitively, one would expect the results obtained with this second method to be in between the results when the fits were performed with the first method when the events were reconstructed with either positive or negative solution. The results on the last line in Table 5.11 confirm this expectation for R_2 and R_3.

Reproduced with permission of the copyright owner. Further reproduction prohibited without permission.

5.5.5 Stability of the Fit

The extra terms and factors which account for non-vanishing lepton mass have the largest contribution at low q^2. Assuming that the effects of lepton mass were correctly taken into account, the fit should be stable against a cut on q^2/q^2_{max}. The results varied within about 1 σ if the lower bound of q^2/q^2_{max} cut was in the range from 0.0 to 0.5. The values of form factor ratios are shown in Fig. 5.11.

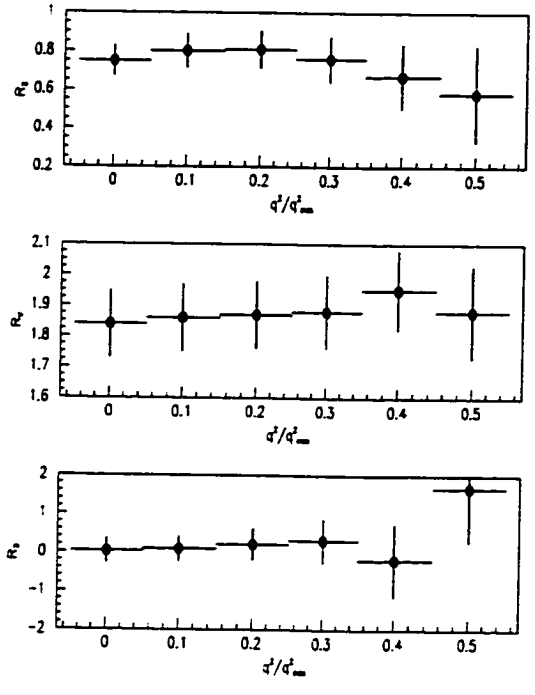

Figure 5.11: Stability of R_2, R_V and R_3 against a cut on the minimum allowed value of q^2/q^2_{max}. Only statistical errors are shown.

The small variations of form factor ratios in the region of low q^2/q^2_{max} shows that the effects of non-zero lepton mass were correctly included in the decay rate formula.

Reproduced with permission of the copyright owner. Further reproduction prohibited without permission.

5.5.6 M_{min} Cut

The cut on M_{min} substantially reduced charmed as well as non-charmed background. Variation of the results when M_{min} cut is changed should be consistent with statistical and systematic errors due to background subtraction and detector effects. The fit values of form factor ratios are plotted in Fig. 5.12 for a cut on the lower bound of M_{min} varying from 1.50 GeV to 1.70 GeV, while the upper bound was kept constant at the standard value of 2.0 GeV. A similar study was done for the upper bound of M_{min}, which was varied from 1.90 GeV to 2.10 GeV, holding the lower bound constant at 1.60 GeV. The values of the form factor ratios are plotted in Fig. 5.12.

The variations of the results were less than the 1 σ statistical error, and are consistent with the systematic errors determined in the previous sections.

5.6 Summary of the Systematic Errors

All systematic errors studied in the previous sections are listed in Table 5.12. The last line of the table contains the systematic errors added in quadrature.

For the first fitting technique, the unbinned loglikelihood method, the largest contributions to systematic errors came from muon ID, background subtraction and cut selection. In addition to these sources of systematic errors, the second fitting technique is relatively more sensitive to the binning. Overall, the systematic errors of the first two form factor ratios are close to statistical uncertainties.

Reproduced with permission of the copyright owner. Further reproduction prohibited without permission.

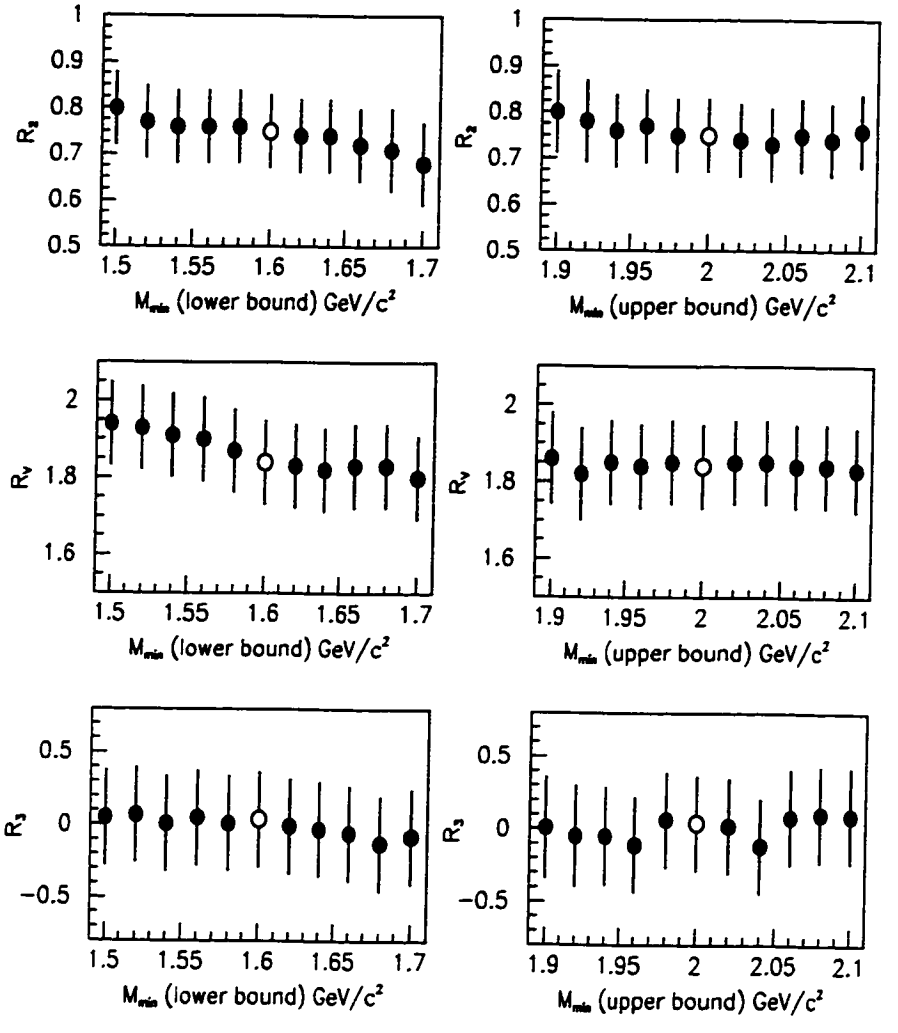

Figure 5.12: Values of R_2 , R_V and R_3 for varying cuts on M_{min}. The lower bound of M_{min} was varied from 1.5 to 1.7 GeV holding the upper bound constant at 2.0 GeV (left side plots). The upper bound of M_{min} was varied from 1.9 to 2.1 GeV holding the lower bound constant at 1.6 GeV (right side plots). Open circles correspond to standard cuts on M_{min}.

Reproduced with permission of the copyright owner. Further reproduction prohibited without permission.

Table 5.12: The main contributions to form-factor uncertainties.

	First Method			Second Method		
Source	σ_{R_2}	σ_{R_V}	σ_{R_3}	σ_{R_2}	σ_{R_V}	σ_{R_3}
Simulation of detector effects	0.06	0.08	0.16	0.06	0.07	0.19
Hadron ID	0.01	0.01	0.02	0.01	0.01	0.02
Muon ID	0.04	0.06	0.10	0.05	0.04	0.11
Production mechanism	0.01	0.01	0.02	0.01	0.01	0.03
Acceptance	0.03	0.02	0.08	0.02	0.02	0.09
Cut Selection	0.03	0.04	0.09	0.03	0.05	0.13
Fitting technique	0.02	0.03	0.22	0.06	0.10	0.30
MC volume size	0.02	0.02	0.12	0.06	0.10	0.30
Number of MC points	0.01	0.01	0.18	-	-	-
Systematic shift	0.01	0.02	0.06	0.01	0.02	0.06
Background	0.06	0.04	0.08	0.06	0.05	0.26
Number of bgnd. events	0.04	0.02	0.06	0.04	0.03	0.25
Bgnd. shape	0.04	0.04	0.06	0.04	0.04	0.08
Total	0.09	0.09	0.29	0.10	0.13	0.44

Reproduced with permission of the copyright owner. Further reproduction prohibited without permission.

Chapter 6

Results and Conclusions

6.1 Final Results

The values of form factor ratios were calculated with both fitting techniques described in Chapter 4. The fit values obtained with the unbinned loglikelihood method (the first fitting technique) are our final results:

$$R_2 = 0.75 \pm 0.08 \pm 0.09, \quad R_V = 1.84 \pm 0.11 \pm 0.09, \quad R_3 = 0.04 \pm 0.33 \pm 0.29.$$

The correlation coefficients between pairs of form factor ratios are:

$$CC_{R_2 R_V} = -0.090 \quad CC_{R_2 R_3} = -0.211 \quad CC_{R_V R_3} = -0.087$$

The second fitting technique (matrix method) was developed as a check of the first method. The values of the form factor ratios calculated with the second method are close to the previous results:

$$R_2 = 0.72 \pm 0.08 \pm 0.10, \quad R_V = 1.90 \pm 0.12 \pm 0.13, \quad R_3 = -0.25 \pm 0.34 \pm 0.44.$$

This method for extracting the form factor ratios uses the same $D^+ \to \overline{K}^{*0}\mu^+\nu_\mu$ candidates as the previous method, but used both neutrino-momentum solutions. This is true both for the data and for the Monte Carlo sample used in the likelihood function calculation, so the results of this fit could differ from those of the previous fit. The values

Reproduced with permission of the copyright owner. Further reproduction prohibited without permission.

of the form factor ratios obtained with the two methods agree well, providing further assurance that selecting the lower neutrino momentum solution in the primary method and correcting for the systematic bias gives the correct result.

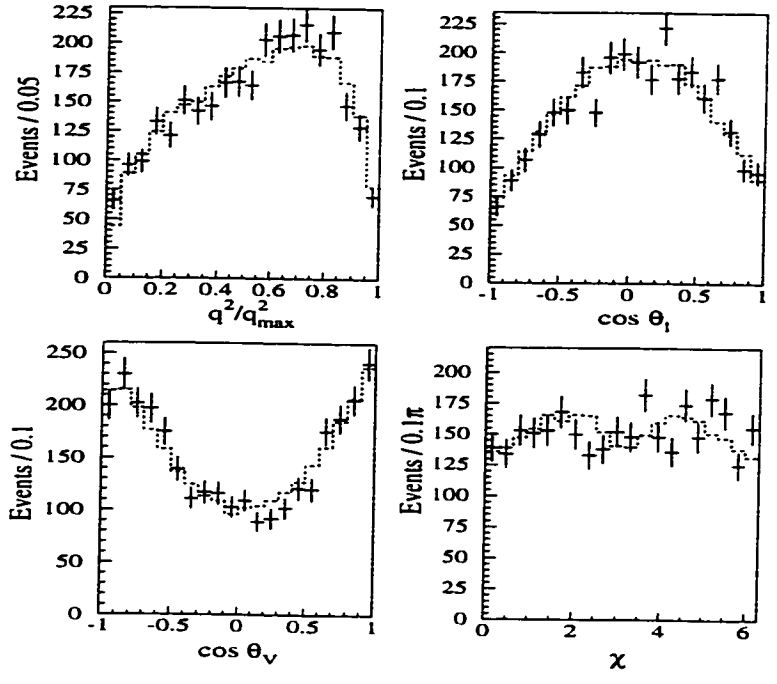

Figure 6.1: Background subtracted data distributions (cross hatches) overlaid with Monte Carlo (dashed line) with best fit values for the form factor ratios.

The distributions of the four kinematic variables overlaid with the similar distributions of Monte Carlo events, weighted according to the fit results, are shown in Fig. 6.1. The formalism predicts a partial suppression of transverse helicity amplitudes at low q^2. As a consequence of this fact, the decay distributions should exhibit stronger $\cos^2\theta_V$ and $\sin^2\theta_l$ components as q^2 decreases. This behavior can be seen in Fig. 6.2, where the angular variables were plotted in various slices of the four-dimensional kinematic variable space.

Reproduced with permission of the copyright owner. Further reproduction prohibited without permission.

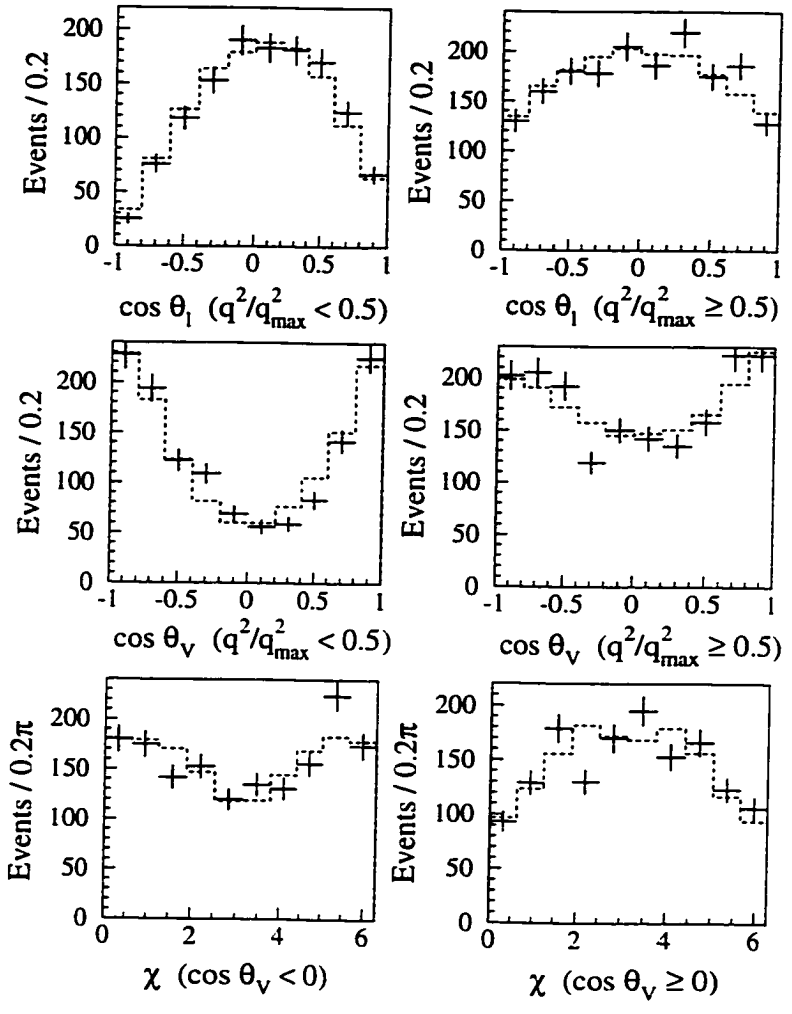

Figure 6.2: Comparison of single-variable distributions of background-subtracted data (crosses) with Monte Carlo predictions (dashed histograms) using best-fit values for the form factor ratios. In the plots of $\cos\theta_l$ and $\cos\theta_V$ data has been divided into two ranges of q^2/q^2_{max}, while the distribution of χ is shown for two ranges of $\cos\theta_V$.

Reproduced with permission of the copyright owner. Further reproduction prohibited without permission.

6.2 Conclusions

6.2.1 $D^+ \to \overline{K}^{*0}\mu^+\nu_\mu$

The fit was performed on 3034 candidate $D^+ \to \overline{K}^{*0}\mu^+\nu_\mu$ events (3629 right-sign and 595 wrong-sign). Systematic errors related to simulation of detector effects, fitting technique and background subtraction were estimated, and these contributions were added in quadrature. Statistical and systematic errors have about the same magnitude. The determination of the form factor ratios for $D^+ \to \overline{K}^{*0}\mu^+\nu_\mu$ presented here and for the similar decay channel $D^+ \to \overline{K}^{*0}e^+\nu_e$ [5] follow the same analysis procedure except for the charged lepton identification. Both results as well as other previously published experimental results are shown in Table 6.1.

Table 6.1: Comparison of E791 results with previous experimental results. The E791 electron result for r_V is 0.06 higher than the value reported in Ref. [5] because we have corrected for inaccuracies in the earlier modeling of the D^+ transverse momentum.

Exp.	Events	$r_V = V(0)/A_1(0)$	$r_2 = A_2(0)/A_1(0)$
E791	6000 $(e+\mu)$	$1.87 \pm 0.08 \pm 0.07$	$0.73 \pm 0.06 \pm 0.08$
E791	3000 (μ)	$1.84 \pm 0.11 \pm 0.09$	$0.75 \pm 0.08 \pm 0.09$
E791[5]	3000 (e)	$1.90 \pm 0.11 \pm 0.09$	$0.71 \pm 0.08 \pm 0.09$
E687[6]	900 (μ)	$1.74 \pm 0.27 \pm 0.28$	$0.78 \pm 0.18 \pm 0.10$
E653[7]	300 (μ)	$2.00^{+0.34}_{-0.32} \pm 0.16$	$0.82^{+0.22}_{-0.23} \pm 0.11$
E691[8]	200 (e)	$2.0 \pm 0.6 \pm 0.3$	$0.0 \pm 0.5 \pm 0.2$

The values of the form factors are in agreement with the previously published results within the estimated errors. The E791 experimental errors are now significantly lower than theoretical uncertainties quoted by most models (Table 1.1).

Using form factor ratios, one can calculate the values of the form factors A_1, A_2, A_3 and V evaluated at a particular value of q^2. Using the world averages for $B(D^+ \to \overline{K}^{*0}\mu^+\nu_\mu)$

Reproduced with permission of the copyright owner. Further reproduction prohibited without permission.

D^+ lifetime and CKM matrix element V_{cs}, one can extract the values of form factors evaluated at $q^2 = 0$. Table 6.2 compares the measured results for $A_1(0)$, $A_2(0)$ and $V(0)$ with theoretical predictions.

Table 6.2: Comparison of the measured form factor values $A_1(0)$, $A_2(0)$ and $V(0)$ with theoretical predictions.

Group	$A_1(0)$	$A_2(0)$	$V(0)$
E791 (this work)	0.59 ± 0.01	0.44 ± 0.06	1.08 ± 0.09
APE[13]	0.67 ± 0.11	0.49 ± 0.34	1.08 ± 0.22
Wuppertal[24]	$0.61^{+0.11}_{-0.09}$	$0.83^{+0.23}_{-0.22}$	$1.34^{+0.31}_{-0.28}$
UKQCD[14]	$0.70^{+0.07}_{-0.10}$	$0.66^{+0.10}_{-0.15}$	$1.01^{+0.30}_{-0.13}$
ELC[12]	0.64 ± 0.16	0.41 ± 0.28	0.86 ± 0.24

The errors quoted for the experimental values (the first line in Table 6.2) are related only to the errors on the fit values of form factor ratios (statistical and systematic added in quadrature). They do not include the experimental errors on branching fraction, lifetime and V_{cs}. The value of $A_3(0)$ is 0.02 ± 0.26. The central values of branching fraction, lifetime and V_{cs} used for the evaluation of the form factors are: $BR = 0.045$, $\tau = 1.057 \times 10^{-12} s$, and $V_{cs} = 0.975$.

This is the first measurement of R_3, which is relevant only for non-vanishing lepton mass, and probes the spin 0 component of the W^+ boson (page 8). The precision of R_3 measurement is low, but still the measured value of this form factor ratio ($R_3 = 0.04 \pm 0.33 \pm 0.29$) suggests that S-wave decay of the D^+ is highly favored over P-wave decay.

Reproduced with permission of the copyright owner. Further reproduction prohibited without permission.

6.2.2 $D^+ \to \overline{K}^{*0}\ell^+\nu_\ell$

The analysis for muon mode followed the same steps as our previous analysis on form factor ratios for electron mode. The similarities between the two analysis refer to:

1. Data selection (except for lepton identification).
2. Spectrometer effects.
3. Fitting technique.
4. Size of final data sample.

Assuming that the hadronic weak current (which contains the form factors) does not depend on the leptonic W decay, the values of the form factor ratios measured in the electron and muon modes can be combined. To evaluate the systematic errors of the combined results, the general procedure described in Ref. [27] was followed. The systematic uncertainties of the combined results were evaluated for each source, from the systematic errors measured for each decay channel and the correlations between them:

$$\sigma_x^{e+\mu} = \frac{1}{2}\sqrt{(\sigma_x^e)^2 + (\sigma_x^\mu)^2 + 2\sigma_x^e\sigma_x^\mu(x^e, x^\mu)} \tag{6.1}$$

where $x = R_2$ or R_V and (x^e, x^μ) is the correlation coefficient between the two measurements.

The values of the combined systematic uncertainties and the correlations between the two sets of measurements are shown in Table 6.3. When the correlation coefficients were not determined, the systematic errors measured for the two decay channels were (conservatively) assumed to be totally correlated.

Reproduced with permission of the copyright owner. Further reproduction prohibited without permission.

Table 6.3: The main contributions to form factor uncertainties measured for $D^+ \to \overline{K}^{*0}\ell^+\nu_\ell$.

Source	$\sigma^e_{R_2}$	$\sigma^\mu_{R_2}$	$\sigma^e_{R_V}$	$\sigma^\mu_{R_V}$	(R^e_2, R^μ_2)	(R^e_V, R^μ_V)	$\sigma^{e+\mu}_{R_2}$	$\sigma^{e+\mu}_{R_V}$
Detector effects	0.03	0.05	0.06	0.07	-	-	0.047	0.051
Hadron ID	0.01	0.01	0.01	0.01	≈ 1	≈ 1	0.010	0.010
Lepton ID	0.01	0.04	0.05	0.06	0.000	0.000	0.021	0.039
Production mech.	-	0.01	-	0.01	≈ 1	≈ 1	0.010	0.010
Acceptance	-	0.03	-	0 02	≈ 1	≈ 1	0.030	0.020
Cut sel.	0.03	0.03	0.03	0.04	0.357	-0.213	0.025	0.022
Fitting Technique	0.04	0.02	0.04	0.03	-	-	0.020	0.030
MC vol. size	0.04	0.02	0.04	0.02	-0.532	0.135	0.017	0.024
No. of MC pts.	0.01	0.01	0.01	0.01	-0.194	-0.258	0.006	0.006
Shift	0.01	0.01	0.01	0.02	0.000	0.000	0.007	0.015
Background	0.07	0.04	0.04	0.03	-	-	0.064	0.044
No. of bgd. evts	0.05	0.04	0.02	0.02	0.974	-0.237	0.045	0.013
Bgnd. vol. size	0.05	0.02	0.04	0.02	0.966	-0.673	0.035	0.015
Bgnd. shape (model)	-	0.03	-	0.04	≈ 1	≈ 1	0.030	0.040
Total	0.09	0.09	0.09	0.09	-	-	0.081	0.073

The combined values of the form factor ratios are:

$$\boldsymbol{R_2 = 0.73 \pm 0.06 \pm 0.08 \qquad R_V = 1.87 \pm 0.08 \pm 0.07}$$

Figure 6.3 compares E791 values of form factor ratios for $D^+ \to \overline{K}^{*0}\ell^+\nu_\ell$ with previously published results (top) and with theoretical predictions (bottom). At this time the spread of the theoretical results is significantly higher than E791 errors.

Reproduced with permission of the copyright owner. Further reproduction prohibited without permission.

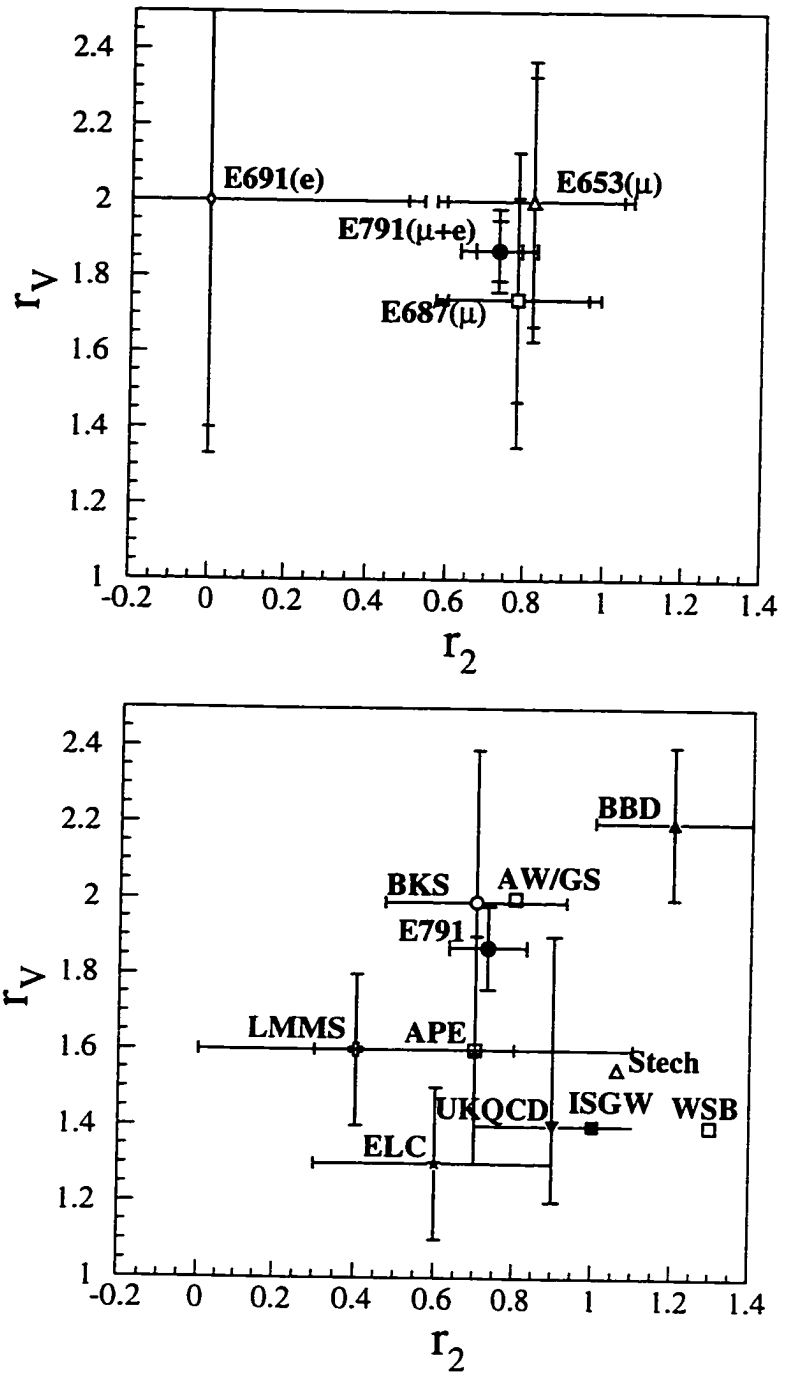

Figure 6.3: Top: Comparison of experimental measurements of form factor ratios r_V and r_2 for $D^+ \to \overline{K}^{*0}\ell^+\nu_\ell$ in the muon (μ), electron (e) and combined ($\mu + e$) channels. The smaller error bars indicate the statistical errors and the larger ones indicate the statistical and sytematic errors added in quadrature. Bottom: Comparison of theoretical predictions with the E791 ($\mu + e$) result.

Reproduced with permission of the copyright owner. Further reproduction prohibited without permission.

6.3 Future Improvements

Statistical and systematic uncertainties contribute about the same to the total errors of the form factors. Significantly better results cannot be obtained only by increasing the statistics. It is necessary to decrease the systematic errors at least as much as the statistical errors. This can be done by improving:

- Lepton identification.
- Vertexing system.
- Monte Carlo simulation.

Better lepton identification can be achieved by increasing the segmentation of electromagnetic calorimeter and by using at least three high-efficiency muon planes in addition to extra tracking devices on muon side. These improvements would be helpful for lowering the systematic uncertainties related to lepton ID and also for reducing the component of the background due to lepton misidentification.

A better vertexing system should attempt to lower the longitudinal vertex resolution from about 320 μm to about 200 μm and consequently to reduce by factor around 2 the background due to fake vertices. The hardware component which is most effective for improving the vertex resolution is the silicon microstrip detector. Spatial resolutions of silicon planes are currently at around 10 μm and can be improved to 3 μm.

Many systematic uncertainties evaluated in this form factor measurement originated from the inaccuracies of the Monte Carlo simulation. A more precise measurement can be done with a better understanding of the detector, reflected in a more reliable Monte Carlo. With only this software improvement the systematic uncertainties would be reduced by at least 20%. With all previously suggested improvements, systematic uncertainties would decrease by a factor of 1.5 to 2.

Reproduced with permission of the copyright owner. Further reproduction prohibited without permission.

Bibliography

[1] N. Isgur and M. B. Wise, Phys. Rev. D 42 (1990) 2388.

[2] J.G. Körner and G.A. Schuler, Phys. Lett. B 226 (1989) 185.

[3] F.J. Gilman and R.L. Singleton,Jr., 1990, Phys. Rev. D **41**, 93.

[4] Particle Data Group, Review of Particle Physics, Phys. Rev. D 50 (1994) 1568.

[5] Fermilab E791 Collaboration, E.M. Aitala et al., Phys. Rev. Lett. 80 (1998) 1393.

[6] Fermilab E687 Collaboration, P.L. Frabetti et al., Phys. Lett. B 307 (1993) 262.

[7] Fermilab E653 Collaboration, K. Kodama et al., Phys. Lett. B 274 (1992) 246.

[8] Fermilab E691 Collaboration, J.C. Anjos et al., Phys. Rev. Lett. 65 (1990) 2630.

[9] N. Isgur, D. Scora, B. Grinstein, and M.B. Wise, Phys. Rev. D 39 (1989) 799.

[10] M. Wirbel, B. Stech, and M. Bauer, Z. Phys. C 29 (1985) 637.

[11] T. Altomari and L. Wolfenstein, Phys. Rev. D 37 (1988) 681.

[12] B. Stech, Z. Phys. C 75 (1997) 245.

[13] C.W. Bernard, Z.X. El-Khadra, and A. Soni, Phys. Rev. D 45 (1991) 869; Phys. Rev. D 47 (1993) 998.

[14] V. Lubicz, G. Martinelli, M. S. McCarthy, and C. T. Sachrajda, Phys. Lett. B 307 (1992) 415.

Reproduced with permission of the copyright owner. Further reproduction prohibited without permission.

[15] A. Abada et al., Nucl. Phys. B 416 (1994) 675.

[16] C.R. Alton et al., Phys. Lett. B 345 (1995) 513.

[17] M. Nieves et al., Nucl. Phys. Proc. Suppl. 42 (1995) 431.

[18] P. Ball, V.M. Braun, and H.G. Dosch, Phys. Rev. D 44 (1991) 3567.

[19] J.A. Appel, Ann. Rev. Nucl. Part. Sci. 42 (1992) 367; D.J. Summers *et al*, XXVII Rencontre de Moriond, Les Arcs, France (15-22 March 1992) 417.

[20] *Search for $D^0 - \overline{D}^0$ Mixing Using Semileptonic Decays*, Ph. D. Thesis, A. K. Tripathi, The Ohio State University, 1997.

[21] *Search for Flavor Changing Neutral Current Decays of Charm Mesons*, Ph. D. Thesis, N. J. Witchey, The Ohio State University, 1996.

[22] *Measurement of the Form Factors in the Semileptonic Decay $D^+ \to \overline{K}^{*0} e^+ \nu_e$*, Ph. D. Thesis, P. Gagnon, University of California at Santa Cruz, 1993.

[23] *Performance of the Čerenkov Counters in the Fermilab Tagged Photon Spectrometer Facility*, D. Bartlett *et al.*, Nucl. Instr. Meth. A260 (1987) 55.

[24] *Description of Analysis of Muon Wall Efficiency*, N. Witchey, A. Nguyen and N. W. Reay, E791 offline document number 113.

[25] D.M. Schmidt, R.J. Morrison, and M.S. Witherell, Nucl. Instrum. Methods A 328 (1993) 547.

[26] *Measurement of the Form Factor Ratios for $D^+ \to \overline{K}^{*0} e^+ \nu_e$*, R. Zalizniak, offline doc 296, E791 internal documents.

[27] L. Lyons, Statistics for Nuclear and Particle Physicists (Cambridge University Press, Cambridge, 1986).

Reproduced with permission of the copyright owner. Further reproduction prohibited without permission.

Appendix A

Neutrino Momentum Ambiguity

With real data, no tracking information is available for the neutrino, but it is possible, given the momenta of the three visible particles, to calculate the neutrino momentum up to a quadratic ambiguity. From momentum and energy conservation laws, one can write:

$$m_D^2 = (p^{vis} + p^{\nu})^2 = m_{vis}^2 + 2(p^{vis} \cdot p^{\nu}) \tag{A.1}$$

As well as having information about the 4-momenta of the charged D decay products, the direction of flight of the D meson is also known from the vertex positions measurements. The transverse momentum of the neutrino with respect to the direction of the D meson is constrained: $\mathbf{p}_{\perp}^{\nu} = -\mathbf{p}_{\perp}^{vis}$. If the system is boosted along the direction of the D meson to the frame where the component along the D direction $\mathbf{p}_{\parallel}^{vis}$ is zero, then the previous relation can be transformed into a relation for $\mathbf{p}_{\parallel}^{\nu}$ in terms of measurable quantities:

$$m_D^2 = m_{vis}^2 + 2\left[E^{vis}\sqrt{(\mathbf{p}_{\perp}^{vis})^2 + (\mathbf{p}_{\parallel}^{\nu})^2} + (\mathbf{p}_{\perp}^{vis})^2\right] \tag{A.2}$$

This equation can be solved for $\mathbf{p}_{\parallel}^{\nu}$ only up to a two-fold ambiguity:

$$\mathbf{p}_{\parallel}^{\nu} = \pm\left[\left(\frac{m_D^2 - m_{vis}^2 - 2(\mathbf{p}_{\perp}^{vis})^2}{2E^{vis}}\right)^2 - (\mathbf{p}_{\perp}^{vis})^2\right]^{1/2} \tag{A.3}$$

All quantities in equation A3 are evaluated in the reference frame where the parallel visible momentum ($\mathbf{p}_{\parallel}^{vis}$) is zero. The neutrino momentum is usually needed in the rest frame of

Reproduced with permission of the copyright owner. Further reproduction prohibited without permission.

the D meson. Therefore the previous reference frame has to be boosted in either positive or negative direction with:

$$\beta_{\pm} = \frac{(\mathbf{p}_{\parallel}^{\nu})_{\pm}}{E^{vis} + E^{\nu}} \tag{A.4}$$

Because the magnitude of β is the same in both directions, and the transverse momentum is also the same, the magnitude of neutrino momentum in the D rest frame does not depend on which solution A3 is chosen. So, in the rest frame of D:

$$\mid \mathbf{p}_{+}^{\nu} \mid = \mid \mathbf{p}_{-}^{\nu} \mid \tag{A.5}$$

All visible momenta and relative angles evaluated in the rest frame of D depend on which sign is chosen in A3, but the magnitude of neutrino momentum is invariant to this choice.

Due to resolution, some events were reconstructed outside the physical region ($(\mathbf{p})_{\parallel}^{2} < 0$). These "unphysical" events were recovered by setting $(\mathbf{p})_{\parallel} = 0$. The reconstructed D invariant mass is larger than the PDG value for the "unphysical" events. It is straightforward to show that in these cases the D mass equals M_{min}. So, the "unphysical" events have the value of M_{min} (and reconstructed D mass) between 1.87 GeV and 2.00 GeV. The data sample contained 25.60 % "unphysical" events and Monte Carlo sample 23.43%. The number of "unphysical" events can be varied by changing the upper bound of the M_{min} cut. This study was done in Section 1.5.6. The upper limit of the M_{min} cut was varied in the range from 1.9 GeV to 2.1 GeV. The values of form factor ratios fluctuated within less than 0.5σ statistical errors.

Reproduced with permission of the copyright owner. Further reproduction prohibited without permission.

Appendix B

Muon Identification

Muons were identified in two walls of scintillating counters behind shielding equivalent to 2.5 meters of steel. The two muon walls provided information about the x and y positions of the muon candidate track. Ideally, a true muon should be registered by the projected paddles in both muon walls. This doesn't always happen because the efficiency of the walls is less than 1, and also because of the deflection caused by multiple Coulomb scattering. The standard deviation of the multiple scattering is momentum dependent [23], and is empirically given by:

$$\sigma_x = \frac{55.62}{p - 1.29} cm \tag{B.1}$$

$$\sigma_y = \frac{98.55}{p - 1.87} cm \tag{B.2}$$

where p is the track momentum, and σ_x and σ_y are the widths of multiple scattering distributions at the X and Y walls.

At the substrip level, a particle was included on the muon candidate list if it had momentum larger than 7 GeV and if there was a hit in either the X or Y wall within 3σ of the projected position:

$$p_\mu > 7.and.(n_{\sigma_y} < 3.or.n_{\sigma_x} < 3). \tag{B.3}$$

These loose cuts kept about 99 % of muons having momentum larger than 7 GeV and

Reproduced with permission of the copyright owner. Further reproduction prohibited without permission.

having the track within the Y wall acceptance.

In this analysis a necessary condition for a particle to be identified as a muon is to hit the Y muon wall, with the projected y position away from the hit position by at most 1σ ($n_{\sigma_y} < 1$). This condition was not enough to clean the data sample, and some extra requirements for x position of the projected track were needed.

In addition to X wall, Y-wall TDC information is valuable for x position estimation. The delay of the pulse registered by the phototubes attached to the paddles is correlated with the x position of the track (see fig. B.1 (a)). The parameters of the centerline in the TDC vs. x position plot were determined with "good" muons (the projected position of the track falls within the hit paddles). A variable "dist" was defined as the distance from a point to the centerline. By convention "dist" is positive if the point is above the centerline and negative otherwise. The distribution of this variable is shown in fig. B.1 (b), for right-sign and wrong-sign events. In order to reduce the number of hadron decays in flight, the cut on muon momentum was also tighter, $p_\mu > 8$ GeV, compared with substrip cuts. To summarize, the muon identification was based on the following cuts:

1. $p_\mu > 8$ GeV;
2. $n_{\sigma_y} < 1$;
3. $abs(dist) < 8$ cm.

If two tracks associated with the secondary vertex passed the muon identification cuts, then the first choice for muon candidate was the track which had a higher muon category [20]. If the event didn't pass the rest of the cuts (with the first choice for the muon candidate) then the second possibility for assigning the muon candidate was taken into account. Overall the data sample contained 8.4% of events having two tracks that pass muon ID requirements, compared with 4.7 % similar events in the Monte Carlo sample. The systematic errors related to this kind of inaccuracy in the Monte Carlo simulation were studied in chapter 4.

Reproduced with permission of the copyright owner. Further reproduction prohibited without permission.

This set of cuts kept about 85 % of muons that passed substrip cuts, had momentum larger than 8 GeV and were within the acceptance of Y wall. The data sample obtained with this muon identification scheme has a size similar to that for the decay channel $D^+ \to K^-\pi^+e^+\nu_e$.

Reproduced with permission of the copyright owner. Further reproduction prohibited without permission.

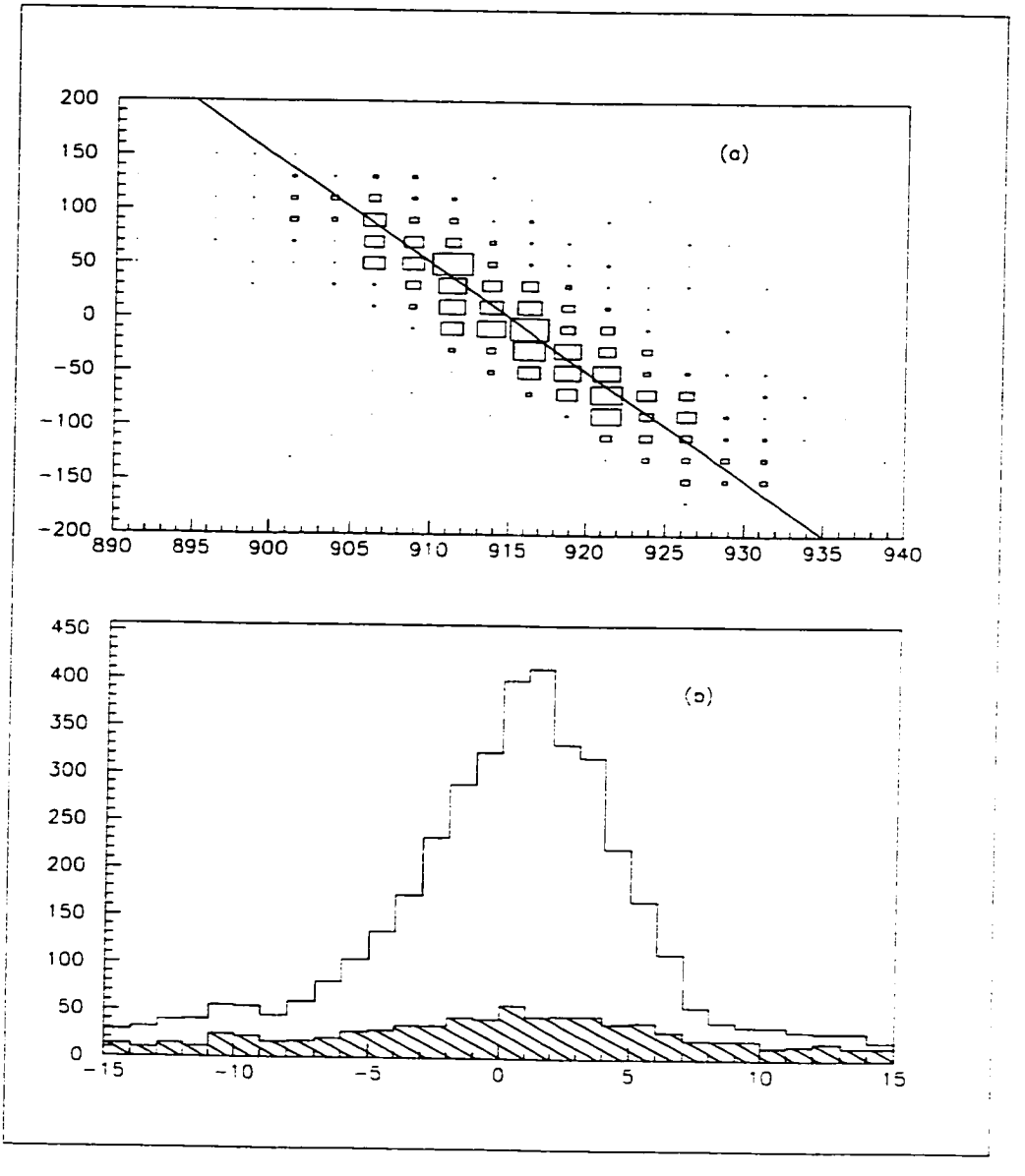

Figure B.1: (a) Centerline in the position and TDC correlation plot. The equation for the line is 10x + y -9150 = 0, where y is the projected X-position on the Y wall and x is the muon TDC from Y wall. (b) Distribution of the DIST variable for RS and WS events.

Reproduced with permission of the copyright owner. Further reproduction prohibited without permission.

Appendix C

The Origin of Systematic Shifts in Fitting

When fits were performed with the unbinned maximum likelihood method, the fit values of the form factor ratios were systematically shifted from the real values. The magnitudes of the systematic shifts were precisely determined from Monte Carlo studies as described in 5.2.1:

$$\delta R_2 = -0.09 \pm 0.01, \qquad \delta R_V = +0.09 \pm 0.02, \qquad \delta R_3 = -0.11 \pm 0.06.$$

The systematic shifts δR_2 and δR_V are comparable to the statistical uncertainties associated with the measurement of R_2 and R_V. δR_3 is one third of the statistical uncertainty of the measured R_3.

The values of the form factor ratios measured for the data sample were corrected by subtracting the systematic shifts previously determined from Monte Carlo studies. This procedure might be wrong if, for example, the systematic shifts depend on the form factors. Therefore, it is important to understand the origin of the systematic shifts. It is interesting to note that a binned maximum likelihood fitting technique does not lead to any systematic bias of the fit results.

Reproduced with permission of the copyright owner. Further reproduction prohibited without permission.

Many potential sources of systematic shifts were investigated. Some of these potential sources which were proven not to be related to the systematic bias are:

- Neutrino momentum ambiguity.
- Smearing effects caused by limited spectrometer resolution.
- Size of the Monte Carlo sample.
- Data selection criteria.
- The minimum number of Monte Carlo events associated to a data point.

These studies suggested that the systematic shifts originate from the unbinned maximum likelihood fitting technique itself, rather than from event reconstruction procedure or data selection criteria. In the unbinned maximum likelihood method, the probability distribution function is well approximated by the whole Monte Carlo sample (Eqn. 4.4):

$$F_{MC}(x;\mu_0) = \frac{1}{N_{MC}} \sum_{i=1}^{N_{MC}} \delta^4(x - \tilde{x}_i) \tag{C.1}$$

where μ_0 is the set of form factor ratios used to generate the Monte Carlo sample, N_{MC} is the total number of Monte Carlo events that were retained after applying all selection criteria, $\tilde{x}_i$'s are the positions in the four-dimensional kinematic variable space associated with each Monte Carlo event and x is an arbitrary point in the phase-space. It is important to note that $F_{MC}(x;\mu_0)$ is not continuous but it is normalized to one. Using the weighting procedure described in 4.3 the probability distribution function $F_{MC}(x;\mu)$, evaluated for an arbitrary set of form factor ratios, can be expressed in terms of $F_{MC}(x;\mu_0)$ (Eqn. 4.6).

When this fitting technique is employed, the probability distribution function (Eqn. C1) cannot be directly used because of the presence of the δ functions. Therefore the general expression C1 is replaced by the average of F_{MC} over a small volume V centered on the position x_i associated with a data event:

$$\bar{F}_{MC}(x_i;\mu) = \frac{1}{V}\int_V d^4x F_{MC}(x;\mu) \tag{C.2}$$

Reproduced with permission of the copyright owner. Further reproduction prohibited without permission.

The volume V in Eqn. C2 is a certain fraction of the total phase-space volume. If the position x_i of a data point is close to the phase-space edges, then the nominal volume V is shrunk such that it is still centered on the data point. In this analysis the nominal volume was 1/625 of the total phase-space volume. The projections of the nominal volume on each one-dimensional kinematic variable subspaces were one fifth of the full range of that variable.

The replacement of the true distribution function F_{MC} with $\bar{F}_{MC}$ is responsible for two major problems:

1. The "average" distribution function $\bar{F}_{MC}$, defined by Eqn. C2, approaches F_{MC} only in the limit $V \to 0$.

2. $\bar{F}_{MC}$ is not normalized to one. When fits are performed with a log-likelihood method the normalization of the probability distribution function is crucial for the correct convergence of the fit.

An example will illustrate how distortion of the distribution function (determined by the transition from $f(x)$ to $\bar{f}(x)$) and its normalization depend on the nominal volume. A simple one-dimensional distribution function $f(x)$ is shown in Fig. C1 (top). The full range of x is from 0 to 1. The "average" distribution function $\bar{f}(x)$ calculated according the prescription given by Eqn. C2 and with the nominal volume the same as the full range of x is shown in Fig. C1 (bottom). The graphs of $\bar{f}(x)$ when the nominal volume was one fifth and one tenth of the full range of x are shown in Fig. C2 top and bottom respectively. As expected, both the distortion of $\bar{f}(x)$ (in comparison with $f(x)$) and the departure from the correct normalization decrease when the nominal volume decreases.

The distortion of the distribution function is not expected to lead to systematic shifts of the fit results because it was shown before that smearing effects (which have the same effect on the distribution function) do not generate systematic bias. Consequently, the approximate normalization of the distribution funtion is mostly responsible for the systematic shifts. The log-likelihood fitting technique is extremely sensitive to the normalization

Reproduced with permission of the copyright owner. Further reproduction prohibited without permission.

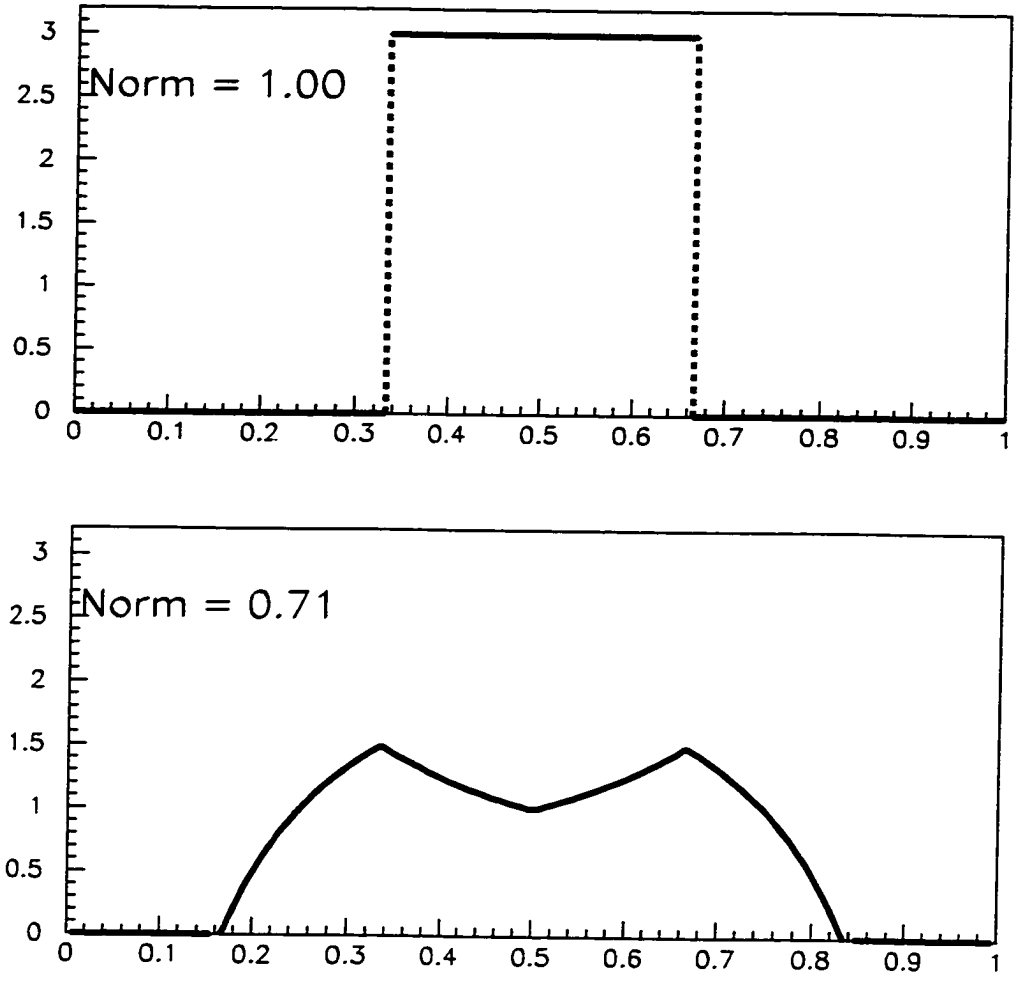

Figure C.1: A correctly-normalized distribution function $f(x)$ is shown in the top plot. The "average" distribution function $\bar{f}(x)$ (defined in the text) is shown in the bottom plot. The nominal volume equals to the full range of x.

Reproduced with permission of the copyright owner. Further reproduction prohibited without permission.

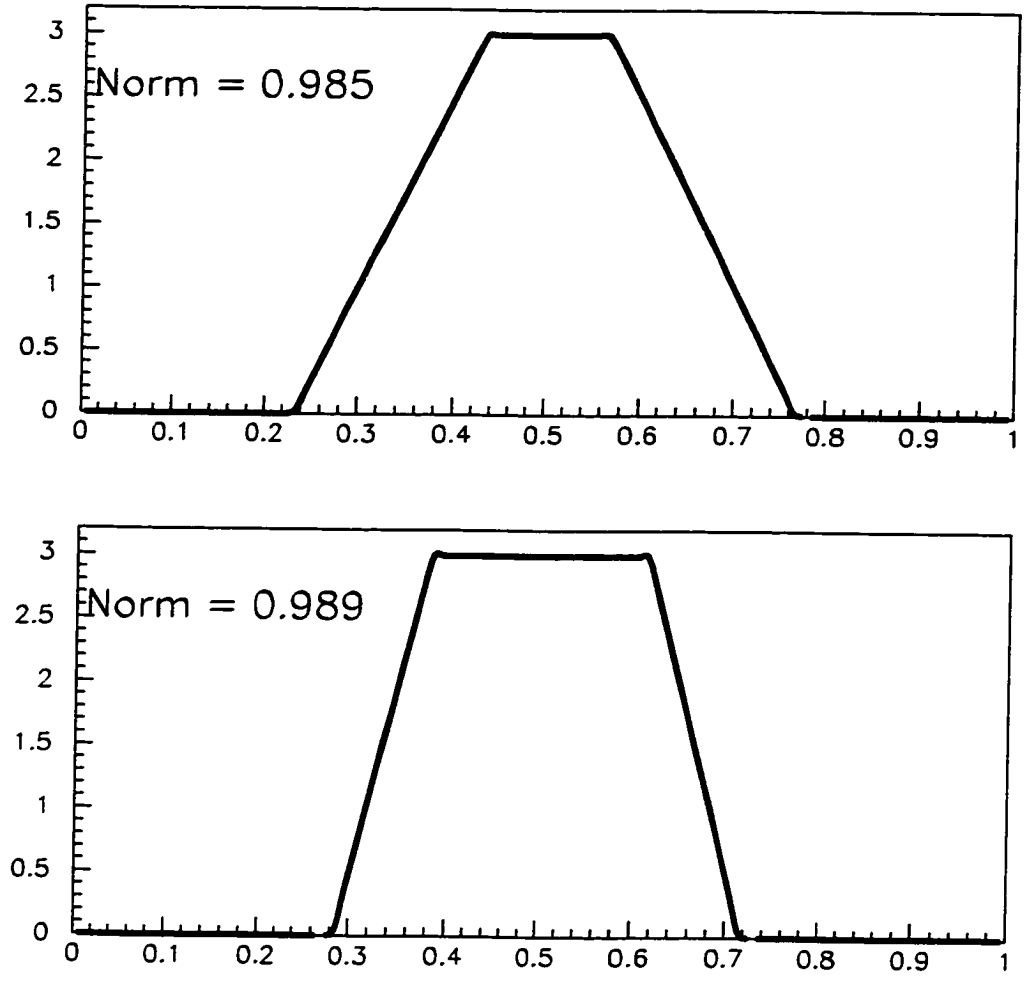

Figure C.2: The "average" distribution functions $\bar{f}(x)$'s when the nominal volume is one fifth (top) and one tenth (bottom) from the full range of x.

Reproduced with permission of the copyright owner. Further reproduction prohibited without permission.

Table C.1: The values of the systematic shifts measured for different values of the nominal volume. The first column shows the number of bins for each kinematic variable.

$n_{q^2}/n_{\cos\theta_l}/n_{\cos\theta_V}/n_\chi$	δR_2	δR_V	δR_3
3/3/3/3	-0.23 ± 0.01	$+0.30 \pm 0.02$	-0.47 ± 0.06
4/4/4/4	-0.15 ± 0.01	$+0.15 \pm 0.02$	-0.17 ± 0.06
5/5/5/5	-0.09 ± 0.01	$+0.09 \pm 0.02$	-0.11 ± 0.06
6/6/6/6	-0.06 ± 0.01	$+0.07 \pm 0.02$	-0.01 ± 0.06
7/7/7/7	-0.04 ± 0.01	$+0.06 \pm 0.02$	$+0.01 \pm 0.06$
8/8/8/8	-0.03 ± 0.01	$+0.06 \pm 0.02$	$+0.01 \pm 0.06$

condition. Even a 1% departure from the correct normalization may affect the fit results subtantially.

To check the binning dependence of the fitted form factor ratios, the systematic shifts were determined for different values of the nominal volume. The results are shown in Table C1. The values of the systematic shifts are indeed strongly dependent on the size of the nominal volume. In practice, the size of the nominal volume cannot be decreased indefinitely because a significant number of data events would be excluded from the fit (the reasons are explained in 4.4.1). For example, with the standard binning ("5/5/5/5") there were 90 data events excluded from the fit. This number increased to 305 when the binning is "8/8/8/8".

Since the systematic shifts depend strongly on binning, it is crucial to check the consistency of the fit values of the form factor ratios (corrected for the systematic shifts) when fits are performed with different binning conditions. The results are shown in Table C2 and plotted in Fig. C3. After applying the corrections for the systematic shifts, the values of the form factors are consistent each other no matter what the binning is.

As shown before, the probability distribution function is not normalized to one when

Reproduced with permission of the copyright owner. Further reproduction prohibited without permission.

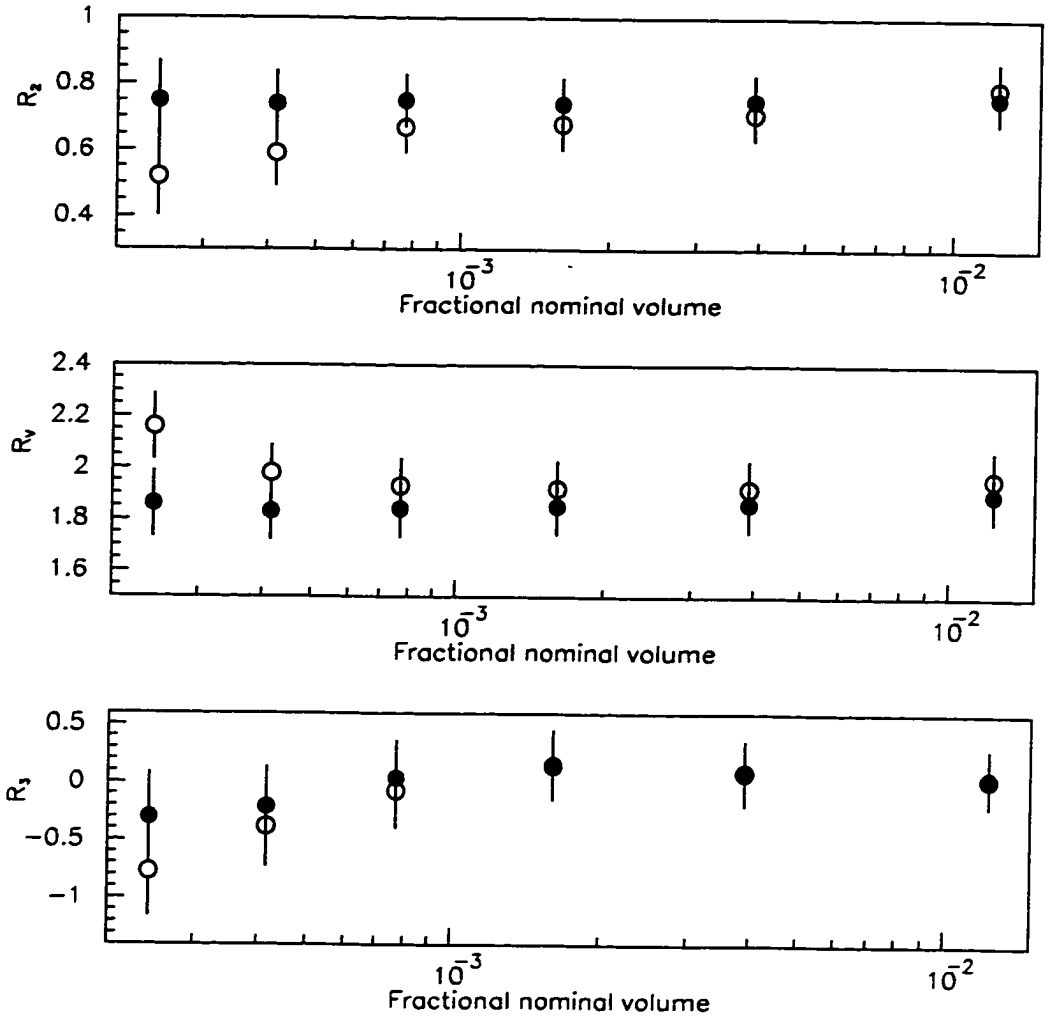

Figure C.3: Values of the form factor ratios, uncorrected (open circles) and corrected (black bullets) for the systematic shifts. The horizontal axis represents the fraction nominal volume to the total phase-space volume in log scale. The values of the nominal volume are the same as those in Table C1 and Table C2.

Reproduced with permission of the copyright owner. Further reproduction prohibited without permission.

Table C.2: The values of the form factor ratios uncorrected and corrected for the systematic shifts. The corrections were done by subtracting the values of the systematic shifts listed in Table C1.

Binning	R_2	R_V	R_3	$(R_2)_{corr}$	$(R_V)_{corr}$	$(R_3)_{corr}$
3/3/3/3	0.52 ± 0.12	2.16 ± 0.13	-0.77 ± 0.39	0.75 ± 0.12	1.86 ± 0.13	-0.30 ± 0.39
4/4/4/4	0.59 ± 0.10	1.98 ± 0.11	-0.38 ± 0.35	0.74 ± 0.10	1.83 ± 0.11	-0.30 ± 0.39
5/5/5/5	0.67 ± 0.08	1.93 ± 0.11	-0.07 ± 0.33	0.75 ± 0.08	1.84 ± 0.11	0.04 ± 0.33
6/6/6/6	0.68 ± 0.08	1.92 ± 0.11	0.15 ± 0.30	0.74 ± 0.08	1.85 ± 0.11	0.16 ± 0.30
7/7/7/7	0.71 ± 0.08	1.92 ± 0.11	0.09 ± 0.28	0.75 ± 0.08	1.86 ± 0.11	0.08 ± 0.28
8/8/8/8	0.73 ± 0.08	1.96 ± 0.11	0.04 ± 0.25	0.76 ± 0.08	1.90 ± 0.11	0.03 ± 0.25

the fits are performed with the unbinned log-likelihood method. The distribution function (Eqn. 4.6) can be normalized to one if divided by its integral over the whole phase-space. The distribution function (Eqn. 4.6) was integrated numerically using 50,000 points randomly distributed over the four-dimensional kinematic variable space. The values of the systematic shifts were again measured for the standard binning. As expected they significantly decresed; from -0.09 to -0.01 for R_2, from 0.09 to 0.05 for R_V and from -0.11 to -0.04 for R_3. The numerical integration of the probability distribution function (Eqn. 4.6) is extremely time-consuming and it can be performed for only a relatively low number of points. This means that the normalization condition is still not perfectly fulfiled. Although the correct normalization of the probability distribution function greatly reduces the systematic shifts, it is reasonable to assume that there is at least one more reason for the systematic bias. The most likely additional source of syatematic shifts is the non-linearity of the distribution function over the small volume centered on each data point. No measurements of the contribution to the systematic shifts associated with the non-linearity effects were performed.

Reproduced with permission of the copyright owner. Further reproduction prohibited without permission.

In summary:

- The systematic shifts originate from:

  1. Approximate normalization of the probability distribution function.
  2. Non-linearity of the decay rate within the volume centered on the data point.

- The values of the systematic shifs can be precisely determined from Monte Carlo studies.

- The fit values of the form factor ratios can be corrected (by subtracting the systematic shifts) in a consistent manner.

Reproduced with permission of the copyright owner. Further reproduction prohibited without permission.

IMAGE EVALUATION TEST TARGET (QA-3)

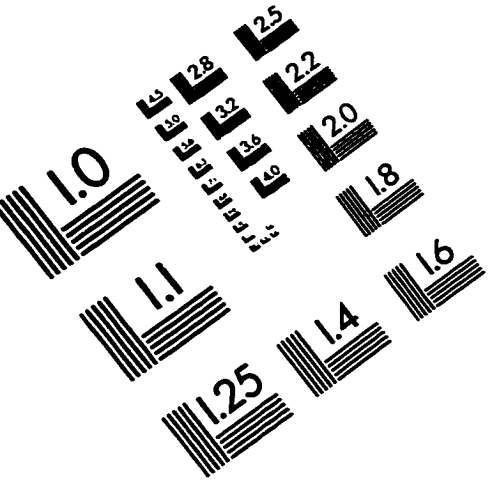

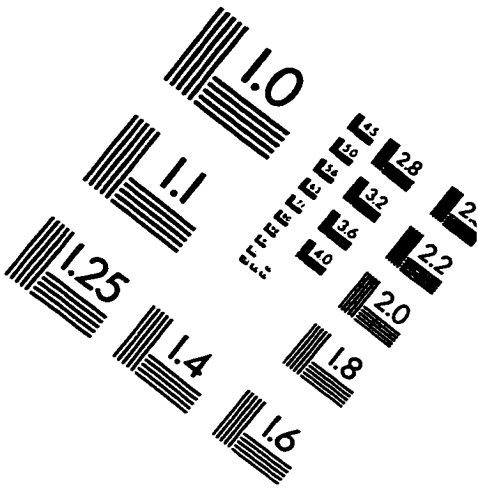

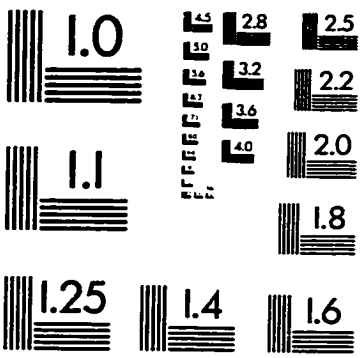

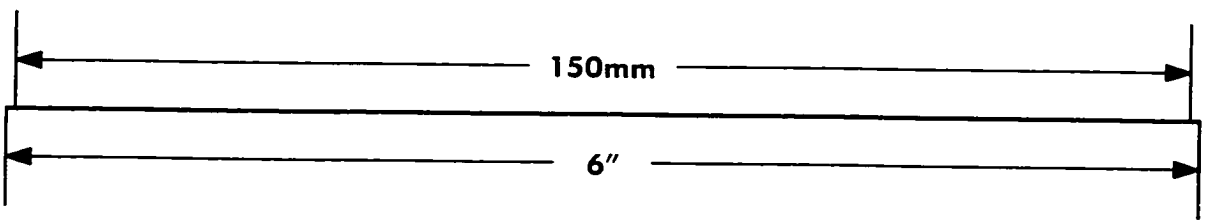

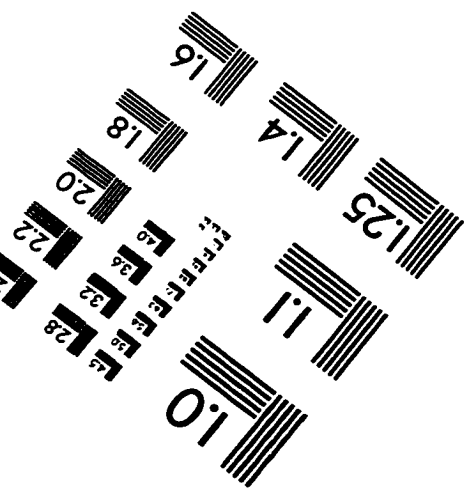

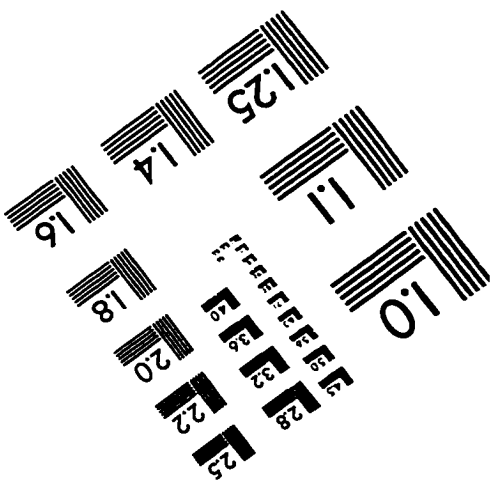

APPLIED IMAGE, Inc
1653 East Main Street
Rochester, NY 14609 USA
Phone: 716/482-0300
Fax: 716/288-5989

© 1993, Applied Image, Inc., All Rights Reserved

Reproduced with permission of the copyright owner. Further reproduction prohibited without permission.